

UNIVERSITY OF CALIFORNIA,
IRVINE

Limonene-Derived Secondary Organic Aerosol:
Composition and Photochemistry

DISSERTATION

submitted in partial satisfaction of the requirements
for the degree of

DOCTOR OF PHILOSOPHY

in Chemistry

by

Maggie Lynn Walser

Dissertation Committee:
Professor Sergey A. Nizkorodov, Chair
Professor Barbara J. Finlayson-Pitts
Professor Donald R. Blake

2007

Chapter 3 & portions of Chapter 5 © 2007 Royal Society of Chemistry
Chapter 4 & portions of Chapter 5 © 2007 American Chemical Society
Appendix II © 2006 & 2007 American Geophysical Union
All other materials © 2007 Maggie Lynn Walser

The dissertation of Maggie Lynn Walser
is approved and is acceptable in quality and form for
publication on microfilm and in digital formats:

Committee Chair

University of California, Irvine
2007

DEDICATION

To my parents, William and Barbara Walser,
who always remind me to be true to myself.

TABLE OF CONTENTS

	Page
LIST OF FIGURES	v
LIST OF TABLES	vi
ACKNOWLEDGEMENTS	vii
CURRICULUM VITAE	viii
ABSTRACT OF THE DISSERTATION	ix
CHAPTER 1: Introduction	1
Atmospheric chemistry background	
Atmospheric aerosol	
Objective of the current study	
CHAPTER 2: Literature survey	13
CHAPTER 3: Composition	25
Introduction	
Experimental	
Results and discussion	
Conclusion	
CHAPTER 4: Photochemistry	46
Introduction	
Experimental	
Results and discussion	
Conclusion	
CHAPTER 5: Mechanisms	62
Introduction	
Reaction mechanisms and discussion	
Conclusion	
APPENDIX I: Solvent effects	73
APPENDIX II: Trace gas measurements	83
Methyl halides in the atmosphere	
Terrestrial methyl halide sources	
Experimental	
Results and discussion	
Conclusion	
REFERENCES	117

LIST OF FIGURES

<u>Figure</u>	<u>Title</u>	<u>Page</u>
1.1	Radiative forcing components	5
2.1	Structures of the most common monoterpenes	14
2.2	Criegee mechanism	16
3.1	Aerosol generation setup	27
3.2	Representative ESI mass spectra of SOA particles	30
3.3	Kendrick and van Krevelen diagrams	37
3.4	Comparison of measured and predicted SOA components	43
4.1	Aerosol generation setup	48
4.2	IR – CRDS setup	50
4.3	UV/Vis spectra of limonene and aerosol particles	52
4.4	IR-CRDS spectra resulting from broad photolysis ($\lambda > 295$ nm)	54
4.5	Time dependent IR-CRDS signals	56
4.6	Limonene SOA formic acid action spectra	57
5.1	Initial products of limonene ozonolysis	64
5.2	Radical isomerization and oxygen addition mechanism	66
5.3	Radical decomposition mechanism	67
5.4	Formation of secondary products	69
5.5	Organic peroxide formation during ozonolysis of limonene	70
5.6	Photolysis reactions of organic peroxide species	72
I.1	Mass spectra of SOA extracted in 4 solvents	74
I.2	Monomer region of mass spectra of SOA extracted in 4 solvents	75
I.3	Mass spectra of SOA extracted in isotopically labeled CH ₃ CN	77
I.4	Mass spectra of SOA extracted in isotopically labeled CH ₃ OH	79
II.1	Map of sampling location	86
II.2	Monthly mean methyl halide emissions	93
II.3	Biomass specific monthly mean methyl halide emissions	94

LIST OF TABLES

<u>Table</u>	<u>Title</u>	<u>Page</u>
2.1	Rate constants for reactions of terpenes and atmospheric oxidants	15
3.1	Elemental composition for the five most abundant peaks observed in the positive and negative ESI modes	32
3.2	Kendrick data for representative oxygenated species	39
I.1	Five most abundant peaks observed in the positive and negative ESI modes from SOA extracted in CH ₃ CN and CH ₃ OH	76
I.2	Five most abundant peaks with even <i>m/z</i> observed in the positive and negative ESI modes from SOA extracted in isotopically labeled CH ₃ OH	81
II.1	Atmospheric methyl halide budgets	84
II.2	Annual methyl halide production from coastal salt marsh plants and controls	96
II.3	Tissue halide content and biomass specific methyl halide production from coastal salt marsh plants	97
II.4	Linear correlation coefficients (<i>r</i>) and molar ratios for monthly methyl halide production from coastal salt marsh plants and controls	104
II.5	Methyl halide emissions from greenhouse-grown mangroves	109
II.6	Tissue halide content of greenhouse-grown mangroves	113

ACKNOWLEDGEMENTS

I would like to thank my thesis advisor, Professor Sergey Nizkorodov, for his support and guidance during my graduate career. To him I say, “So long, and thanks for all the booze.” I also want to thank the members of the Nizkorodov group, past and present. I am particularly grateful to Steve Mang, Dr. Tony Gomez, and Dr. Joelle Underwood for their help in the lab, and more importantly, their friendship.

Special thanks go to my collaborators at the Pacific Northwest National Laboratory, Dr. Alex Laskin, Dr. Julia Laskin, and Dr. Yury Dessiaterik. I also thank my collaborators in AirUCI, especially Matthew Brown, Dr. Ron Grimm, Dr. Theresa McIntire, and Dr. Amy Moskun, who have been friends as well as colleagues. I also owe a great deal to the members of my former research group, Dr. Ralph Cicerone, Dr. Steve Manley, and Dr. Nun-Yii Wang. The support of these three talented scientists was invaluable, and without them, this work would have been impossible. I am also grateful to my colleagues in the Calcium Chapter of Iota Sigma Pi for their support and camaraderie, especially my dear friends Meghan Krage and Megan Bourg. I would also like to thank my good friends Steve Mang and Rob Walder, without whom I would never have survived graduate school.

I would like to thank Dr. Nader Nassif for his friendship and encouragement. Finally, and perhaps most importantly, I would like to thank my family for standing behind me in whatever I do. The love and support of my parents, Bill and Barbara, my brother, Matt, and my best friend, Elizabeth, have made all my achievements possible.

This work was supported by the National Science Foundation, through the Environmental Molecular Science Institute program; grant CHE-0431312 (formerly CHE-0209719), and the Graduate Research Fellowship Program. Additional financial support was provided by the University of California, Irvine through a Chancellor’s Fellowship. The work presented in Chapter 3 & Appendix I was performed in the Environmental Molecular Sciences Laboratory, a national scientific user facility sponsored by the Department of Energy’s Office of Biological and Environmental Research and located at Pacific Northwest National Laboratory. The work presented in Appendix II was supported by the National Science Foundation, through grants ATM-0121153 and OCE-0350746. Brian Shelton, Orange County Ecological Reserve Manager, California Department of Fish and Game provided access to Upper Newport Bay and Michael Goulden (Department of Earth System Science, University of California, Irvine) provided insolation data.

CURRICULUM VITAE

Maggie Lynn Walser

EDUCATION

- Ph.D. in Atmospheric Chemistry 2007
University of California, Irvine
- B.S. in Chemistry, *cum laude*, and Chemical Engineering, *cum laude* 2002
Minor in Earth and Atmospheric Science
University of California, Irvine

PUBLICATIONS

- High-resolution mass spectrometric analysis of secondary organic aerosol produced by ozonation of limonene, M.L. Walser, Y. Dessiaterik, J. Laskin, A. Laskin, and S.A. Nizkorodov, *submitted to Phys Chem Chem Phys*, **2007**.
- Photochemical aging of secondary organic aerosol particles generated from the oxidation of d-limonene, M.L. Walser, J. Park, A.L Gomez, A.R. Russell, and S.A. Nizkorodov, *J Phys Chem A*, **2007**, *111*, 1907-1913.
- Methyl halide emissions from greenhouse-grown mangroves, S.L. Manley, N.-Y. Wang, M.L. Walser, and R.J. Cicerone, *Geophys Res Lett*, **2007**, *34*, L01806.
- Ozonolysis and photolysis of alkene-terminated self-assembled monolayers on quartz nanoparticles: implications for photochemical aging of organic aerosol particles, J. Park, A.L. Gomez, M.L. Walser, A. Lin, and S.A. Nizkorodov, *Phys Chem Chem Phys*, **2006**, *8*, 2506-2512.
- Annual intrinsic methyl halide production by coastal salt marsh plants: global contributions revisited, S.L. Manley, N.-Y. Wang, M.L. Walser, and R.J. Cicerone, *Global Biogeochem Cycles*, **2006**, *20*, GB3015.
- UV photodissociation spectroscopy of oxidized undecylenic acid films, A.L. Gomez, J. Park, M.L. Walser, A. Lin and S.A. Nizkorodov, *J Phys Chem A*, **2006**, *110*, 3584-3592.
- Seasonal mass balance of halogens in simulated rice paddies, K.R. Redeker, S.L. Manley, L. Brothers, K. McDuffee, M. Walser, and R.J. Cicerone, *Geophys Res Lett*, **2004**, *31*, L11504.
- Physiological and biochemical controls over methyl halide emissions from rice plants, K.R. Redeker, S.L. Manley, M. Walser, and R.J. Cicerone, *Global Biogeochem Cycles*, **2004**, *18*, GB1007.

ABSTRACT OF THE DISSERTATION

Limonene-Derived Secondary Organic Aerosol:
Composition and Photochemistry

by

Maggie Lynn Walser

Doctor of Philosophy in Chemistry

University of California, Irvine, 2007

Professor Sergey A. Nizkorodov, Chair

Atmospheric aerosol particles affect global climate, local air quality, and human health. A large fraction of organic aerosol are formed as secondary organic aerosol (SOA) resulting from the condensation of partially oxidized volatile organic compounds (VOC). Monoterpenes compose a significant fraction of biogenic VOC emissions and their oxidation products have been shown to form SOA in relatively large yields. Once SOA particles are formed, they undergo aging processes in the atmosphere, and because atmospheric particles are exposed to sunlight 8-14 hours a day, photochemical processes are likely to be among the primary aging mechanisms. This work focuses on the composition and photochemical aging of SOA particles resulting from the oxidation of d-limonene vapor by ozone.

SOA particles formed from the ozone-initiated oxidation of d-limonene vapor were collected and analyzed using a variety of techniques. Accurate mass measurement using high-resolution mass spectrometry was used for the determination of elemental composition, while tandem mass spectrometry aided in structural characterization. Kendrick analysis was used to reduce the complexity of the spectra

by identifying groups of homologous species that differ by the number of repeating groups (i.e. $-\text{CH}_2$ or $-\text{O}$).

The photochemical properties of SOA particles were studied using infrared cavity ringdown spectroscopy (IR-CRDS) and standard absorption techniques. UV/Vis spectroscopy showed that SOA particles absorb significantly more radiation at atmospherically relevant wavelengths than the parent limonene molecule. IR spectra of gas-phase photolysis products of limonene SOA showed formation of both formic acid and formaldehyde. Formic acid production as a function of UV photolysis wavelength was also investigated, and measurable amounts of formic acid were produced at atmospherically relevant wavelengths. The results of this investigation indicate that solar radiation may play a significant role in the processing of SOA in the atmosphere. Finally, a detailed mechanism of the ozone-induced oxidation of limonene, resulting particle formation, and subsequent photochemistry is presented.

CHAPTER 1

INTRODUCTION

While the American public has been slow to accept the reality of global climate change, there is now a general consensus among scientists and much of the world's population that the Earth is warming due, at least in part, to human activities. In 2001, the Intergovernmental Panel on Climate Change stated in its Synthesis Report that "Earth's climate system has demonstrably changed on both global and regional scales since the pre-industrial era, with some of these changes attributable to human activities."¹ Due to increased scientific understanding of global climate change, the most recent IPCC report gives a 90% probability that human activity has contributed to net warming of the Earth since 1750.²

Much of the global economy currently depends on fossil fuels for energy, and their massive consumption has contributed to atmospheric levels of carbon dioxide reaching 368 ppm (parts per million) in 2000, up from 280 ppm in the period 1000-1750.¹ Methane, another greenhouse gas, also increased: from 700 ppb (parts per billion) in the pre-industrial atmosphere to a level of 1,750 ppb in 2000.¹ These numbers alone show that humans are impacting the global environment, and it is unreasonable to believe that if we continue on our current path, these effects will not change our world in ways we cannot currently understand.

Fossil fuel consumption often receives the majority of the blame for global climate change, and while it is in fact a major culprit, it is not the only factor. Many other factors affect both the global climate and regional atmospheric chemistry, ranging from trace gases to atmospheric particulate matter, with both natural and

human sources. While it is important to quantify and understand the climate effects of anthropogenic species, it is also necessary to increase our knowledge of biogenic sources of atmospheric trace gases and particulate matter. A more thorough knowledge of the climate impacts of naturally occurring species is necessary for the regulation of manmade emissions and the creation of responsible environmental policy.

This dissertation presents a study of secondary organic aerosol (SOA) produced by the reaction of ozone with limonene, a naturally occurring gas emitted by trees and other plants. Limonene is one of the major monoterpenes emitted from forests, fruit trees, and even soil,³⁻⁶ and often forms aerosol in higher yields than other monoterpenes. Novel instrumentation, including high-resolution Orbitrap mass spectrometry and infrared cavity ringdown spectroscopy are used to probe the composition and aging mechanisms of limonene-derived SOA. Additionally, mechanisms for aerosol formation and photochemical aging are presented, and implications for atmospheric chemistry are discussed. Finally, quantification of biogenic emissions of methyl halides from two natural ecosystems, coastal salt marshes and mangrove forests, will be presented as an appendix.

Atmospheric chemistry background

It is well known that the atmosphere is composed mainly of nitrogen (78%), oxygen (21%) and argon (0.9%).^{7,8} These major components of the atmosphere undergo virtually no chemistry; it is the remaining 0.1% of gases that participate in most atmospheric processes. The most well known examples of trace gas chemistry

include smog formation in the lower troposphere and the destruction of stratospheric ozone.

The formation of photochemical smog involves a complex set of reactions that produce a variety of products, including ozone, from volatile organic compounds, nitrogen dioxide, and sunlight. The result is the brown haze that is characteristic of Los Angeles and other large metropolitan areas. In the stratosphere, ozone that shields the Earth's surface from ultraviolet radiation can be depleted by a series of reactions involving halogen radicals. Such species are transported to the upper atmosphere in the form of long-lived species such as chlorofluorocarbons and methyl halides.⁸⁻¹¹

The reactions involved in the above processes occur, for the most part, in the gas phase. Another important component of the atmosphere is aerosol particles, which span a wide range of sizes, lifetimes, and composition. Number densities of aerosol particles range from 10^{11} - 10^{12} m^{-3} to 1.5×10^{10} m^{-3} in urban and rural atmospheres, respectively.⁹ Atmospheric aerosol are receiving an increasing amount of interest among atmospheric scientists because there is a great deal of uncertainty concerning their impact on, among other things, global climate and human health.

Atmospheric aerosol

Atmospheric aerosol particles affect both tropospheric chemistry and human health, and play an important role in controlling global climate and local air quality. Tropospheric aerosol particles provide surfaces for heterogeneous chemistry such as the transformation of gaseous HNO_3 to HCl and aqueous reactions of other species,

including SO₂ and NO₂.^{8,9} Particulate matter has been linked to negative health effects such as an increased incidence of asthma, and fine particles have been correlated to both cancer and mortality.

Climate and air quality

There is currently a large degree of uncertainty as to the degree of radiative forcing caused by atmospheric aerosol particles. Radiative forcing is the net change in radiation power reaching the Earth's surface due to a particular perturbation, and can be either negative or positive (measured in W m⁻²).^{8,10} For example, greenhouse gases such as carbon dioxide and methane have a positive radiative forcing, which results in a net warming effect on the climate.⁷ The 2007 IPCC report stated that atmospheric aerosol likely have a net negative radiative forcing, however the magnitude of the forcing is still undetermined (Figure 1.1).

Aerosol particles affect the radiative balance of the Earth's atmosphere both directly and indirectly.^{7,8,11,12} Direct effects include scattering and absorption of solar radiation and absorption of infrared radiation emitted by the Earth's surface. Because the diameters of many atmospheric particles are comparable to the wavelengths of visible light, such particles efficiently scatter incoming solar radiation (Mie scattering) resulting in a net cooling effect, sometimes referred to as the "whitehouse effect."^{7,8,10,11}

The absorption of both solar and infrared radiation by atmospheric particles results in positive radiative forcing. Such absorption depends on the aerosol composition, making it hard to quantify. Particles containing elemental carbon or

iron compounds absorb in the visible region, while species such as nitrate, sulfate, and organics absorb longer, infrared wavelengths.⁸

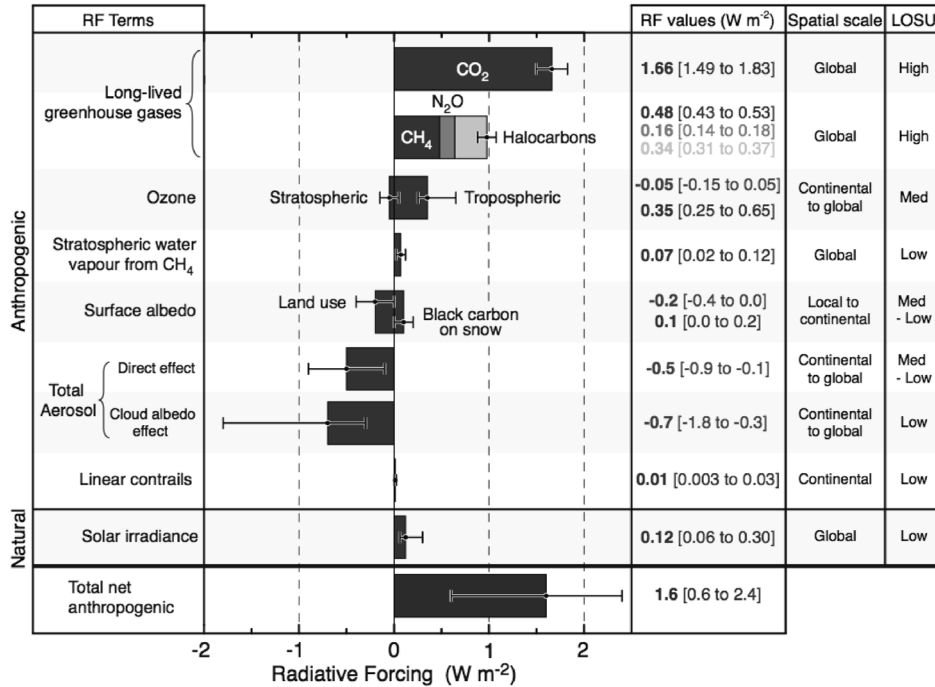


Figure 1.1: Radiative forcing components. Positive radiative forcing results in net warming, while negative radiative forcing results in net cooling of the atmosphere. Aerosol contribute to cooling of the atmosphere, however the magnitude of radiative forcing due to aerosol remains uncertain, and the level of scientific understanding of the effects of atmospheric aerosol is low. (RF = radiative forcing; LOSU = level of scientific understanding; figure taken from Ref. 2)

Atmospheric aerosol also affect climate indirectly, and it is this effect that leads to much of the uncertainty in the magnitude of radiative forcing due to particles. The indirect effects of aerosol particles involve the formation and properties of clouds. Certain particles have the ability to act as cloud condensation nuclei (CCN) and large concentrations of CCN in the atmosphere affect the number of droplets within a cloud and thus the cloud albedo and condensation rate. Increased particle

numbers lead to increased droplet concentrations within a cloud, which increases the cloud's albedo, a mechanism known as the Twomey effect. Because the presence of particles increases the number of cloud droplets, for a given liquid water content, the droplets will generally be smaller. This leads to slower precipitation rates, and thus longer-lived clouds, which results in net cooling.^{8,10,11}

In addition to global effects, aerosol particles have local and regional impacts, as they negatively impact both air quality and visibility.¹⁰ In remote atmospheres, visual ranges can extend hundreds of kilometers, whereas visibility is reduced to only a few kilometers in heavily polluted regions.⁸

Health effects

The reduced air quality associated with increased particle concentrations has been linked to a number of negative health effects, ranging from increased incidences of asthma to heart attack, stroke, and even death. It is generally recognized that the respiratory health of both children and adults is affected negatively by exposure to air pollution, including particulate matter. Children are particularly at risk, and recently, exposure to ultrafine particles has been identified as a potential public health concern.¹³ A study of over 1700 children in Munich, Germany found associations between traffic-related pollutants and increased incidence of respiratory symptoms. In particular, a significant correlation between PM_{2.5} (particulate matter with diameters < 2.5 μm) exposure and respiratory symptoms during the first 2 years of life was found.¹⁴

Traffic-related pollution has also been positively linked to an increased risk of acute myocardial infarction, that is, heart attack. In a study of hospitalizations in five European cities, Lanki et al.¹⁵ found an association between particle number concentration and the occurrence of a first heart attack. In a recent study of over 1800 women, each $10 \mu\text{g m}^{-3}$ increase in $\text{PM}_{2.5}$ increased the risk of a first heart attack by a factor of 1.5. The same increment in particle concentration was also associated with a 76% increase in death due to cardiovascular disease.¹⁶ In addition to increased risk for negative cardiovascular effects, particle exposure after a heart attack is associated with decreased survival rates.¹⁷ Exposure to ambient particles has been linked to an increase in ischemic stroke as well as stroke mortality.^{18,19} Indeed, particulate exposure has long been associated with increased mortality due to numerous causes, including stroke, diabetes, cardiovascular disease, and lung cancer.²⁰⁻²²

Aerosol sources

Sources of atmospheric aerosol are as varied as their composition and properties. The major classes of inorganic aerosol include mineral dust, elemental carbon, sulfate aerosol, and sea salt aerosol. Mineral dust particles enter the atmosphere as a result of large dust storms in deserts such as the Sahara and Gobi, while aerosol particles containing black carbon and sulfate are mainly the result of anthropogenic activities. Sea salt aerosol result from ocean wave action and are most prevalent in coastal areas. These particles consist of an aqueous salt solution, and often have an organic coating. This is especially true of aged sea salt aerosol.^{7-9,11}

Organic aerosol particles are less understood by scientists, and are receiving an increasing amount of attention, especially as it is recognized that even inorganic aerosol often have an organic layer on their surface. Studies have shown that as much as 31% and 24% of urban and non-urban aerosol, respectively, can be organic in nature, making organic aerosol particles and their chemistry of particular interest to atmospheric chemists.²³ Primary organic aerosol (POA) particles are those emitted directly into the atmosphere. POA come from a variety of sources, including biomass burning, traffic, construction, and meat cooking. Secondary organic aerosol (SOA), on the other hand, are formed in the atmosphere by chemical reactions and up to 90% of urban organic aerosol has been shown to be secondary in nature.²⁴

Formation of SOA results from the condensation and nucleation of partially oxidized volatile organic compounds (VOC). Oxidation occurs through reactions with the primary atmospheric oxidants: ozone (O₃), hydroxyl radical (OH), or nitrate radical (NO₃). The oxidation products must reach high enough concentrations to condense onto existing particles or nucleate into condensed form. While many different VOCs can be oxidized to form SOA, the work presented here will focus on the oxidation of monoterpenes, specifically limonene.

Terpene-derived aerosol

Monoterpenes, such as α - and β -pinene and limonene, are a group of molecules (C₁₀H₁₆) that have been shown to form SOA with a high degree of efficiency. Terpenes are a class of hydrocarbons with unsaturated bonds that are emitted by plants and formed from isoprene (C₅H₈) subunits. Monoterpenes

generally having mixing ratios ranging from 0.03-2 ppb, and atmospheric lifetimes of ~0.4 days.⁹ Oxidation of their carbon-carbon double bonds produces species with a variety of functional groups, including alcohols, aldehydes, ketones, and carboxylic acids, all of which tend to have lower vapor pressures than the parent terpenes and can condense to form particles. Aerosol yields from the oxidation of monoterpenes range from as low as 5% to nearly 100%, depending on the structure of the terpene, at atmospherically relevant concentrations.²⁵ Limonene, which contains two carbon-carbon double bonds tends to form SOA more efficiently than mono-unsaturated species such as α - or β -pinene.²⁶

In the United States, on a regional scale, biogenic emissions of VOCs tend to be about three times higher than anthropogenic emissions, and monoterpenes are responsible for a significant fraction of biogenic VOC emissions.²⁷ A study using tethered balloon observations in Alabama found that fluxes of α - and β -pinene were ~1800 and 800 $\mu\text{g m}^{-2} \text{h}^{-1}$, respectively.²⁸ Monoterpenes have been shown to comprise as much as 97% of VOC emissions from pine forests, with concentrations just above the forest canopy on the order of 10 ppb.^{5,29} Fluxes of limonene from orange orchards in Denmark were measured as ~200 $\mu\text{g m}^{-2} \text{h}^{-1}$.⁴ Monoterpene emissions from soil have also been quantified, with limonene and α -pinene dominating the total soil emissions at all three depths measured.³⁰ It is estimated that 11% of the ~1200 Tg C annual VOC flux is due to monoterpenes.²⁷

Diurnal variations of monoterpenes have been found to depend both on their emissions and the presence of OH and NO₃.³¹ The atmospheric residence times of monoterpenes are primarily limited by reaction with OH during the day and NO₃ at

night, and are typically on the order of a few hours.³² Reaction with ozone is also an important removal mechanism. The atmospheric lifetime of limonene with respect to reaction with ozone ranges from 1.6 h in remote atmospheres to 0.19 h in urban atmospheres, where ozone mixing ratios vary from ~30 ppb to 250 ppb, respectively.³²

Oxidation of terpenes is also an important source of indoor particles.³³⁻³⁵ Terpenes, especially limonene and α -pinene, are major constituents of citrus- and pine-scented cleaning products, respectively. Ozone from outdoor-to-indoor transport, use of office equipment, and air purifiers can react with terpenes, leading to particle formation in the sub-micron range.³⁵

While reactions of monoterpenes with atmospheric oxidants have been studied, they are not completely understood. The state of knowledge regarding atmospheric reactions of monoterpenes, and the resulting SOA formation will be reviewed in greater detail in Chapter 2.

Objective of the current study

To date, most studies of terpene oxidation have involved the identification of gas- and condensed-phase products using various mass spectrometric and chromatographic techniques. Studies of terpene aerosol formation have focused on determining how various factors, such as relative humidity, UV radiation, and NO_x (NO and NO₂) concentration affect aerosol yield. This research builds upon previous studies by using high-resolution mass spectrometry to characterize the composition of limonene-derived SOA. The mass-spectra reveal a large number of both monomeric

and oligomeric products of oxidation. The work presented in Chapter 3, along with the work of Reinhardt et al.,³⁶ represents the first application of techniques developed by high-resolution mass-spectrometrists for analysis of complex mixtures to SOA characterization.

While progress has been made in identifying what species are present upon particle formation, it has yet to be determined how a particle's composition will change in the atmosphere. Very little research has focused on the aging mechanisms of SOA. Chapter 4 presents an investigation of the photochemical aging mechanisms of limonene-derived SOA. Photolysis of limonene SOA in the tropospheric actinic region ($\lambda > 295$ nm) readily produces formic acid and formaldehyde as gas-phase products. The data suggest that the rate of photochemical aging of SOA particles in the atmosphere is likely comparable to the rate of chemical aging.

Finally, in Chapter 5 a qualitative mechanism for the formation SOA components is proposed. The mechanism includes known isomerization and addition reactions of the carbonyl oxide intermediates generated during the ozonation of limonene, and numerous isomerization pathways for alkoxy radicals resulting from the decomposition of carbonyl oxides. A qualitative agreement is found between the predicted reaction products and those measured with high-resolution mass spectrometry. The mechanism also predicts the presence of organic peroxides, which is confirmed by the photochemical aging studies of limonene SOA.

The work presented in this dissertation increases the level of scientific understanding of both the composition and atmospheric aging of limonene-derived SOA. As we learn more about this particular system, we can in turn understand more

about the role of organic aerosol in controlling global climate, local and regional air quality, and human health.

CHAPTER 2

LITERATURE SURVEY

As early as 1960, the involvement of terpenes in the formation of tropospheric particles was recognized by Went,³⁷ who observed a blue haze formed by pine needles in the presence of ozone in a bell jar. Since then, a great deal has been learned about the reactions between naturally emitted terpenes and atmospheric oxidants that lead to particle formation. This chapter reviews what is currently known about terpene-derived aerosol yields, gas- and particle-phase products, and how such particles age in the atmosphere.

A large portion of atmospheric aerosol has been found to be organic,^{23,38} and of those many are secondary organic aerosol (SOA),³⁹ often with biogenic precursors.⁴⁰ The loss of approximately half of atmospheric nonmethane organic carbon is unaccounted for, and it has been proposed that SOA formation may be a large part of this missing sink.⁴¹

Monoterpenes ($C_{10}H_{16}$) often comprise a significant portion of biogenic volatile organic compound (VOC) emissions,^{5,27} and because biogenic VOC emissions are often much greater than anthropogenic VOC emissions,^{27,42} it is important to understand the behavior of monoterpenes in the atmosphere. The most commonly observed monoterpenes include α -pinene, β -pinene, Δ^3 -carene, *d*-limonene, camphene, myrcene, α -terpinene, β -phellandrene, sabinene, ρ -cymene, ocimene, α -thujene, terpinolene, and γ -terpinene (Figure 2.1).³ In many cases, α - and β -pinene, as well as limonene, dominate monoterpene emissions,^{4,5,28-30} and they

have been found to form secondary organic aerosol (SOA) in impressively large yields. As such, much of the work discussed herein focuses on these three species.

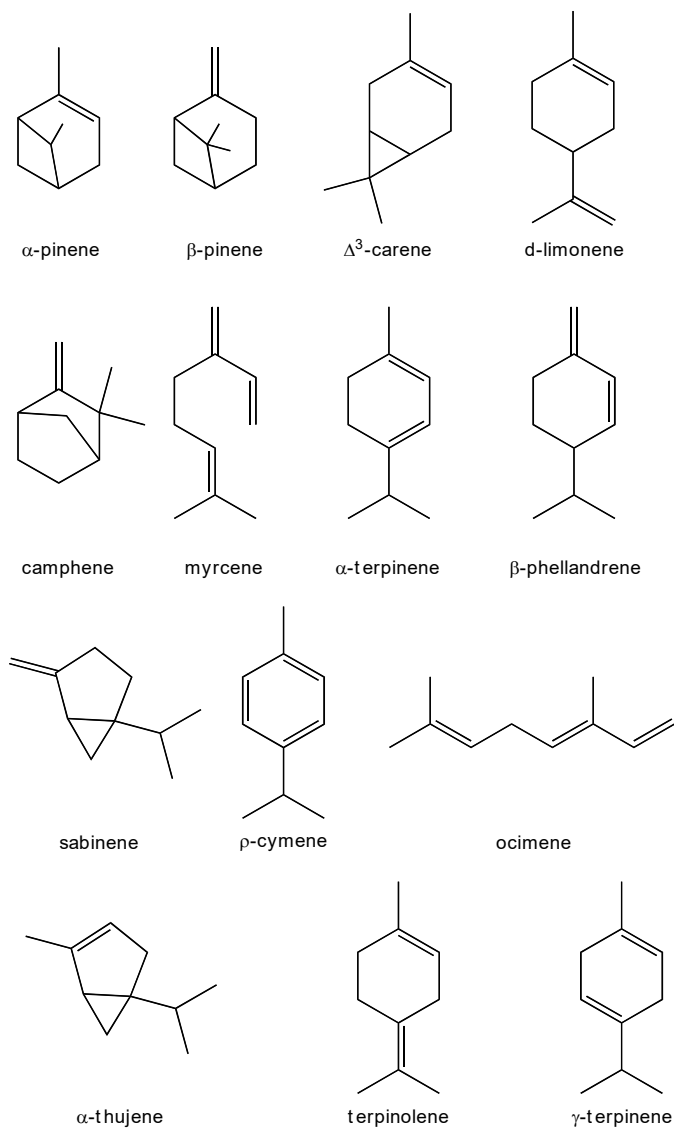


Figure 2.1: Structures of the most common monoterpenes.

Atmospheric terpene oxidation and particle formation

When terpenes are oxidized in the atmosphere, they form species with a variety of functional groups, including carboxylic acids, ketones, aldehydes, and/or

alcohols.⁴³⁻⁴⁸ Many of these species have a lower vapor pressure than their respective parent terpene, and can condense to form particles. It is well known that terpenes react with the major atmospheric oxidants ozone (O₃), hydroxyl radical (OH), and nitrate radical (NO₃). During the day, terpene concentrations are controlled by OH, and at night they are controlled by NO₃, with lifetimes on the order of a few hours.³² Ozone also plays a key role in removing terpenes from the atmosphere, with lifetimes ranging from a fraction of, to a few hours, depending on the ozone mixing ratio.³² Reaction rate constants for 5 of the most abundant terpenes are shown in Table 2.1. Additionally, heterogeneous processes have been identified as a possibly important mechanism for terpene removal and aerosol production in the atmosphere.⁴⁹

Table 2.1: Rate constants for reactions of terpenes and atmospheric oxidants^a

	$k_{\text{O}_3} (\times 10^{18})$	$k_{\text{OH}} (\times 10^{12})$	$k_{\text{NO}_3} (\times 10^{12})$
Δ^3 -Carene	37	88	9.1
Limonene	200	171	12.2
Myrcene	470	215	11
α -pinene	86.6	53.7	6.2
β -pinene	15	78.9	2.5

^aGriffin et al.⁵⁰

Ozone

The atmospheric oxidation of terpenes by ozone proceeds via the well known Criegee mechanism.⁵¹ A primary ozonide (POZ) is formed when ozone adds across a carbon-carbon double bond, forming a 5-membered ring (Figure 2.2). The POZ decomposes quickly, forming one of two possible stable carbonyl species and reactive Criegee intermediate (CI) pairs. The highly reactive CI is stabilized via isomerization, decomposition or recombination, yielding a variety of products. One possible product of recombination is the secondary ozonide, which has been detected

in ozonolysis experiments of limonene, β -pinene, and sabinene.⁵²⁻⁵⁴ Reaction of unsaturated hydrocarbons with ozone leads to formation of lower volatility species, and is an important pathway for aerosol formation.²⁵

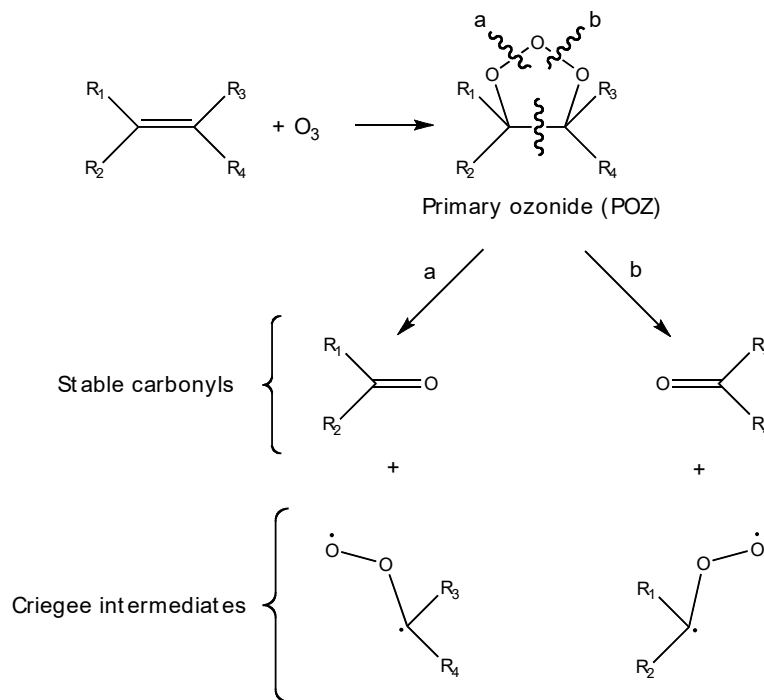


Figure 2.2: Criegee mechanism. Ozone adds across a carbon-carbon double bond via the Criegee mechanism to form a primary ozonide (POZ), which decomposes to form a stable species and a reactive Criegee intermediate (CI).

Hydroxyl and nitrate radicals

Oxidation by the hydroxyl or nitrate radical proceeds via abstraction of a hydrogen atom or addition to a double bond, and results in the formation of a radical species. Reaction between NO_3 and β -pinene, among others, has a high aerosol yield, indicating that nitrate oxidation can lead to a significant amount of aerosol formation at night, when monoterpenes are still emitted by vegetation, albeit, at a reduced rate, and NO_3 accumulates.⁵⁰ For example, the aerosol yield for the reaction between

β -pinene and ozone is quite small (~ 0.05), whereas nitrate oxidation of β -pinene produces aerosol yields as high as 0.9.⁵⁰

Other oxidation and heterogeneous processes

Although not one of the three major atmospheric oxidants, chlorine atoms (Cl) can be an important oxidant in coastal and industrialized areas. Laboratory chlorine oxidation of α - and β -pinene, and limonene gave aerosol yields of 0.2, 0.2, and 0.3, respectively.⁵⁵ The authors therefore concluded that chlorine oxidation of monoterpenes could be a potentially significant source of SOA in the marine boundary layer, coastal areas, and inland industrialized areas.⁵⁵

In addition to the gas-phase oxidation processes outlined above, SOA can also be formed through heterogeneous processes. In particular, interaction between gas-phase organics and particle-phase inorganic acids such as sulfuric acid (H₂SO₄) and nitric acid (HNO₃) can lead to possibly significant SOA formation. For example, Jang et al. found that in the reaction between ozone and isoprene (C₅H₈; the monoterpene building block), the presence of inorganic acid particles nearly doubled the normalized SOA yield.⁴⁹

Products of terpene oxidation

Gas phase

The major gas-phase products in the ozonolysis of β -pinene have been identified as formaldehyde and nopinone (6,6-dimethyl-bicyclo[3,1,1]heptan-2-one), with yields of 0.42 and 0.22, respectively.⁵⁶ Keto-limonene (4-acetyl-1-methyl

cyclohexene) and formaldehyde (yield = 0.10) were observed in the gas phase following ozonolysis of limonene.⁵⁶ Formaldehyde, along with formic acid, acetone, acetaldehyde, acetic acid, and glycolaldehyde, were all observed the gas phase after ozonolysis of terpenes found in household cleaning products.³³ Similar carbonyl products have also been observed in the photooxidation of α - and β -pinene and limonene.⁵⁷

For the OH-initiated oxidation of α - and β -pinene and limonene, formaldehyde, formic acid, acetone, and acetic acid were all detected in the gas phase, depending on the terpene concentration.⁵⁸ Additionally, pinonaldehyde (2',2'-dimethyl-3'-acetyl-cyclobutyl ethanal), nopinone, and keto-limonene were detected for the α - and β -pinene and limonene experiments, respectively.⁵⁸

Particle phase

In laboratory ozonolysis of α -pinene, both pinonaldehyde and pinonic acid (2',2'-dimethyl-3'-acetyl-cyclobutyl acetic acid) have been identified as major condensed phase products.⁵⁹ While these two species have moderate volatilities and are not likely to form new particles, they will partition onto existing particles.⁶⁰ For this reason, these species have been observed in both the gas- and particle-phase. Nopinone, which is also observed in the gas phase,⁵⁶ was identified as the major particle-phase product of β -pinene ozonolysis,^{44,59} along with norpinic and pinic acids.⁴⁴ Leungsakul et al. identified limononaldehyde as the major product of limonene ozonolysis, and this species, along with keto-limonene, keto-limononaldehyde, limononic acid, and keto-limononic acid, accounted for ~60% of

the observed aerosol mass.⁶¹ The products detected in their smog chamber experiments agreed well with their kinetic model.⁶¹ The latter three products have since been identified as major constituents of SOA resulting from the photooxidation of limonene in the presence of NO_x.⁶² Keto-limonene, which results from oxidation of the external double bond in limonene, has been investigated for its aerosol formation potential. Donahue et al. found that aerosol formation from the further oxidation of keto-limonene is similar to α -pinene, and significantly less than that of limonene itself.⁶³

In the OH-initiated oxidation of limonene, both keto-limonene (also observed as a gas phase product⁵⁶) and limononaldehyde were identified as major low volatility products.⁶⁴ Pinonaldehyde and nopinone were identified as the major products of OH oxidation of α - and β -pinene, respectively.⁶⁴ Oxidation of α -pinene and limonene by NO₃ yields pinonaldehyde and limononic acid, respectively, in addition to other unidentified organic nitrates.⁶⁵ Additionally, only products which indicated attack on limonene's internal double bond were observed.⁶⁵

The major products identified in the oxidation reactions of α - and β -pinene and limonene can be predicted by known gas-phase chemistry. In addition to these species, many groups have identified organic peroxides^{66,67} and polyfunctional species.⁴⁵⁻⁴⁸ For example, Docherty et al. estimate that as much as ~47% and 85% of the SOA mass resulting from the ozonolysis of α - and β -pinene, respectively, correspond to molecules containing at least one –O–O– group.⁶⁷

There is also increasing evidence that oligomeric species play a key role in terpene-derived SOA systems,⁶⁸⁻⁷⁰ with oligomeric species contributing to as much as

50% of the mass of α -pinene-derived SOA.⁴⁷ For example, Reinhardt et al. recently detected as many as 450 compounds in the m/z range of 200-700 amu.³⁶ They also found that the O:C ratio decreases with molecular weight, which agrees with previous α -pinene + ozone results, and is most likely due to condensation reactions during oligomer formation.^{36,66} It has been proposed that oligomer species are mostly peroxyhemiacetals, formed from reactions between hydroperoxides and aldehydes.⁶⁷ Inorganic, acidic seed particles can catalyze the formation of oligomeric species,⁷¹ but such oligomers are also detected in the absence of seed particles, indicating the presence of organic acids that also have the capability to catalyze oligomerization.⁴⁷

Aerosol yield

Terpene, oxidant, and seed aerosol identity

Griffin et al. have found that for ozone-initiated oxidation in particular, aerosol yield is less dependent on organic mass concentration than in photooxidation experiments.⁵⁰ In the reaction between NO_3 and α -pinene and limonene, Spittler et al. determined that the chemical character of the seed aerosol plays a role in determining aerosol yield.⁶⁵ Acid-catalyzed heterogeneous processes have been implicated in the formation of low-volatility products, possibly through increased oligomer formation.⁴⁷ For seeded α -pinene + ozone experiments, the yield in the presence of acidic seed aerosol more than doubled the SOA yield compared to non-acid seed particles.⁷¹ When α -pinene is irradiated in the presence of NO_x , adding SO_2 , which produces acidic aerosol, to the system, increased the aerosol yield from 0.096 to 0.132.⁷²

Humidity

While increased relative humidity (RH) may not have a significant effect on the amount of terpene reacted,⁷³ it can increase the amount of aerosol formed. In terpene/ozone reactions, RH influences aerosol yield because the presence of water can affect the product distribution following the decomposition of the POZ.²⁶ Reactions can occur with the stabilized CI or by other, unknown, pathways.^{26,74} By altering the concentration of low volatility ozonolysis products, water impacts the aerosol yield.

In an investigation of limonene, Δ^3 -carene, and α -pinene, Jonsson and coworkers²⁶ found that an increase in the RH resulted in an increase in both the total mass and total number of aerosol. For both high and low monoterpene concentrations, ~30 ppb and ~15 ppb, respectively, increasing the RH from < 2% to ~80%, resulted in a factor of 4 to 7 increase in the integrated mass of the resulting SOA. The number concentration was similarly affected, increasing by a factor of 2 to 3. Jonsson et al. concluded that the increased water vapor must participate in a gas-phase reaction that yields more low volatility product(s).²⁶

In the NO₃ oxidation of α -pinene, increased RH led to a decrease in aerosol mass, and the authors proposed that this was most likely due to a change in the mechanism leading to production of more volatile compounds, or an increased amount of low-volatility products in the gas phase due to water uptake on the particles.⁶⁵

Oxides of nitrogen (NO_x)

The ability of the limonene + ozone reaction to form aerosol is affected by the presence of NO_x (NO + NO₂) and the magnitude of this effect has been found to depend upon the amount of NO_x present.⁷⁵ Zhang et al. found that at low NO_x concentrations, the external carbon-carbon double bond is oxidized heterogeneously after the initial gas-phase oxidation of the internal double bond. At higher NO_x concentrations, such heterogeneous processes are inhibited, and oxidation of the external double bond occurs in the gas phase. This process is much slower, and so the resulting aerosol yield is reduced.⁷⁵

These results are consistent with the work of Presto et al., who also found that increased NO_x concentrations decreased the aerosol yield.⁷⁶ Specifically, when the α -pinene/NO_x ratio is $> \sim 15$, the yield remains roughly constant, but the yield begins to decrease significantly as the ratio decreases.⁷⁶ Likewise, aerosol formation from the photooxidation of β -pinene has been shown to depend non-linearly on the β -pinene/NO_x ratio.⁷⁷ Yield reductions have been observed in the presence of both NO and NO₂, indicating that reactions of RO₂ with both NO and NO₂ form stable products.⁷⁸ When limonene is oxidized in the presence of NO_x, FTIR analysis shows the presence of nitrates in the particle phase.⁷⁹

UV radiation

During the ozonolysis of α -pinene, exposure to UV radiation can decrease the aerosol yield by as much as 20-40%.⁴⁶ Further analysis indicated that the reduction in yield was most likely due to a shift in the product distribution to higher volatility

products.⁴⁶ Aerosol yield is reduced by exposure to UV radiation for conditions of low total aerosol mass as well.⁷⁸

Aerosol aging

There is evidence that particle composition continues to change after aerosol formation has slowed.⁸⁰ Exposure to both ozone and OH can oxidize organic particles, making them more active as cloud condensation nuclei, affecting regional precipitation patterns.^{81,82} Research indicates that the lifetime of organic particles with respect to attack by ozone and OH is on the order of a few days, which is the same order of magnitude as the particle's atmospheric lifetime.^{81,83-85} Therefore, chemical aging is likely to be important for atmospheric organic particles, and must be taken into account.

Exposure to UV light has been shown to suppress aerosol formation in the ozonolysis of both α -pinene⁴⁶ and limonene⁷⁵, so it is not surprising that UV radiation would also affect particle chemistry once they are formed. Limonene has been found to have one of the greatest particle-formation potentials of the terpenes.^{25,34,35} In fact, limonene has been found to contribute to as much as 20% of terpene SOA in areas where it is only ~5% of the total terpene emissions.⁶¹ Oxidation via ozone also seems to form particles more efficiently than other oxidation mechanisms.²⁵ For this reason, and because it less understood than other terpene systems, the limonene + ozone system was chosen for the current investigation. With atmospheric lifetimes on the order of days,⁸³ it is likely that the composition of SOA will change due to both

chemical attack and photochemical degradation. Photochemical aging in particular is one of the focuses of the current work.

CHAPTER 3

COMPOSITION

*Reproduced in part with permission from Phys Chem Chem Phys
submitted for publication.*

Unpublished work copyright © 2007 Royal Society of Chemistry

Introduction

A large portion of aerosol particles in both the free and polluted troposphere contain organic material, therefore it is important to understand the chemical composition and physical properties of the most representative types of organic aerosol particles.^{23,24,86-93} Increasingly, sophisticated methods such as high-resolution mass spectrometry are used to determine the molecular composition of atmospherically relevant organic aerosol species.^{36,68,94-96}

A variety of polyfunctional species, ranging from alcohols to ketones, aldehydes, and carboxylic acids have been detected among the gas- and particle-phase products of monoterpene oxidation (see Chapter 2 for details).^{54,56,61} In the case of the ozone-initiated oxidation of limonene, Leungsakul et al.⁶¹ recently described a semi-empirical mechanism that correctly reproduced the major first-generation products that could be identified by chromatographic techniques, and SOA yields. Limononaldehyde was the major identified product, followed by keto-limonene, keto-limononaldehyde, limononic acid, and keto-limononic acid (structures are shown in Table 3.1). These SOA products accounted for about 60% of the observed particle mass. Major gas-phase products include formaldehyde and keto-limonene,^{54,56} and a relatively stable endo-ozonide was also identified amongst the products.^{52,54,97} Yields

of SOA resulting from the ozonation of limonene have been reported by various groups,^{25,26,34,75,98} with limonene generally yielding more particles than monoterpenes containing a single double bond, such as α - or β -pinene.

The presence of oligomeric species in terpene-derived SOA particles has been reported by multiple groups^{36,47,67,99-101} but the mechanism of their formation is still unclear. This work focuses on the identification of the monomeric and oligomeric chemical species present in SOA particles produced from the ozone-induced oxidation of limonene. We take advantage of the rapidly developing tools of high-resolution mass spectrometry that have the potential to analyze the aerosol particle composition without chromatographic separation techniques.

Experimental

Model SOA particles were formed from the ozone-initiated oxidation of d-limonene vapor in an inflatable Teflon reaction chamber (Figure 3.1). A fan was used to ensure rapid mixing of ozone and limonene in the chamber. The chamber was first filled to approximately 200 L with oxygen (99.994% purity). Ozone was produced at concentrations ranging from 1-10 ppm using a small commercial ozone-generator (EZ-Com air purifier; $68 \text{ mg O}_3 \text{ h}^{-1}$)¹⁰² placed directly inside the chamber. Once the desired ozone concentration was achieved, a 100 sccm (standard cubic centimeters per minute) oxygen flow saturated with d-limonene (97% purity, Fisher Scientific) was injected into the chamber over the course of 10 min. The saturated vapor was obtained by flowing air through a temperature-controlled bubbler containing limonene at $T = 298 \text{ K}$ (partial pressure of d-limonene = 260 Pa). In the

absence of ozone, the final concentration of limonene in the 200 L chamber would be ~10 ppm, but this level was not achieved because oxidation and particle growth occurred in parallel with the slow limonene addition. The resulting mixture was allowed to age in the dark, at room temperature (~298 K) and ambient pressure (~750 torr), for 15-60 min before particle collection.

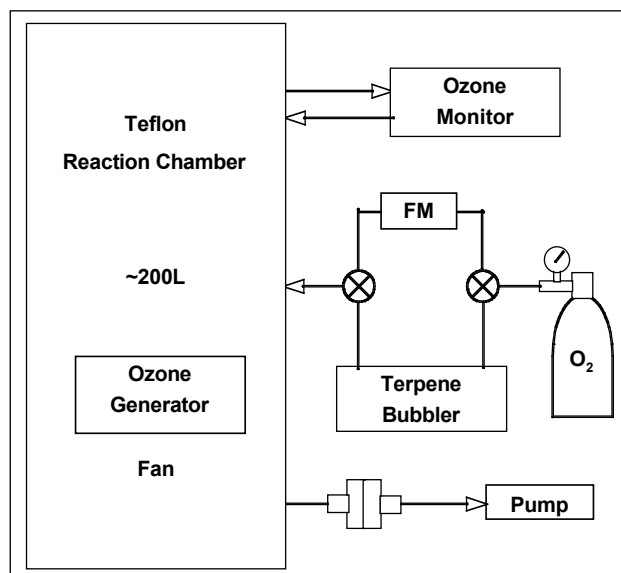


Figure 3.1: Aerosol generation setup. Limonene reacts with ozone in the dark for 15-60 min. The particles are collected and extracted in a suitable solvent for mass-spectrometric analysis.

The particles were collected on a glass fiber filter by pumping air through the filter at 30 slpm (standard liters per minute) over the course of ~6 min, and then ultrasonically extracted with 10 mL of solvent (methanol, acetonitrile, dichloromethane, or water). To assess the degree of functionalization of the analyte molecules by the solvents, isotopically labeled solvents (e.g., CD₃CN rather than CH₃CN) were used. The particle filter collection efficiency was >95% for particles larger than 0.1 μm. Exposure to ambient light was minimized during the collection

and extraction processes. The resulting extracts were then filtered through a 0.45 μm -pore syringe filter before mass-spectrometric analysis.

The composition of the SOA extracts was probed using a Finnigan LTQ Orbitrap Hybrid Mass Spectrometer (Thermo Electron Corporation). An electrospray ionization (ESI) source (Omni Spray™, Prosolia, Inc.) with a fused-silica capillary (30 μm ID) was used. Samples were injected with a flow rate of 0.5-1.5 $\mu\text{L min}^{-1}$ using a spray voltage of 3.5 kV. The system was operated in both positive and negative ion modes with a resolving power of 60,000 to 100,000 ($m/\Delta m$ at 400 amu). The instrument was calibrated using a mixture of stock solutions of caffeine, MRFA, and Ultramark 1621.

MS/MS fragmentation patterns of selected peaks were obtained by isolating a single mass from the full mass spectrum in the linear trap, and setting the nominal collision energy to the value necessary to observe efficient collision induced dissociation (CID) of the selected ion, and detecting the resulting products in the Orbitrap with high mass resolution. The isolation window was typically 1 amu, and the collision energy was adjusted to obtain comparable intensities of the precursor and fragment ions.

Results and discussion

High-resolution mass spectrometric data were used to generate the stick spectra shown in Figure 3.2. Figure 3.2a shows a representative mass spectrum of a limonene SOA sample extracted in acetonitrile obtained in the positive ESI ion mode at a resolving power of 60,000. The spectrum has over 600 peaks in the m/z 1001000

range with intensities exceeding 0.5% of the most abundant peak at 209.0777 amu. The peaks are clustered in clearly identifiable groups separated by ~14 amu. In addition, there is a broader pattern resulting from the presence of oligomerization products: the cluster of peaks centered at m/z 200 corresponds to monomeric products; peaks centered at m/z 400 are dimeric products; and so on.

Composition of the observed peaks was determined by the mass spectrometer software (Xcalibur) assuming that ions contain only ^{12}C , ^{13}C , ^1H , ^{16}O , and ^{23}Na atoms. The proposed assignments were verified manually on a peak-by-peak basis. Analysis of the measured m/z values showed that all major peaks in the monomeric range ($m/z < 300$) contain one Na atom. Alternative composition assignments containing zero or two Na atoms resulted in deviations between the measured and predicted m/z values that were well in excess of the experimental uncertainty. Therefore, complexation to $[\text{Na}]^+$ (m/z 22.9898) is assumed to be the primary ionization pathway for all peaks. This assumption is consistent with the mass spectra of several standards recorded under similar experimental conditions.

The mass spectrum of the same acetonitrile SOA extract obtained in the negative ion ESI mode is shown in Figure 3.2b. It contains about 220 peaks above the 0.5% intensity threshold. Once again, the spectrum displays broad features corresponding to monomeric, dimeric, and trimeric products as well as repeated clusters of peaks separated by ~14 amu. Based on the mass spectra of standards, the major ionization pathway is deprotonation, i.e., removal of a proton (m/z 1.0078) from the parent species. Therefore, the composition is assigned assuming that the ions contain only ^{12}C , ^{13}C , ^1H , and ^{16}O atoms. There is no evidence for the presence of

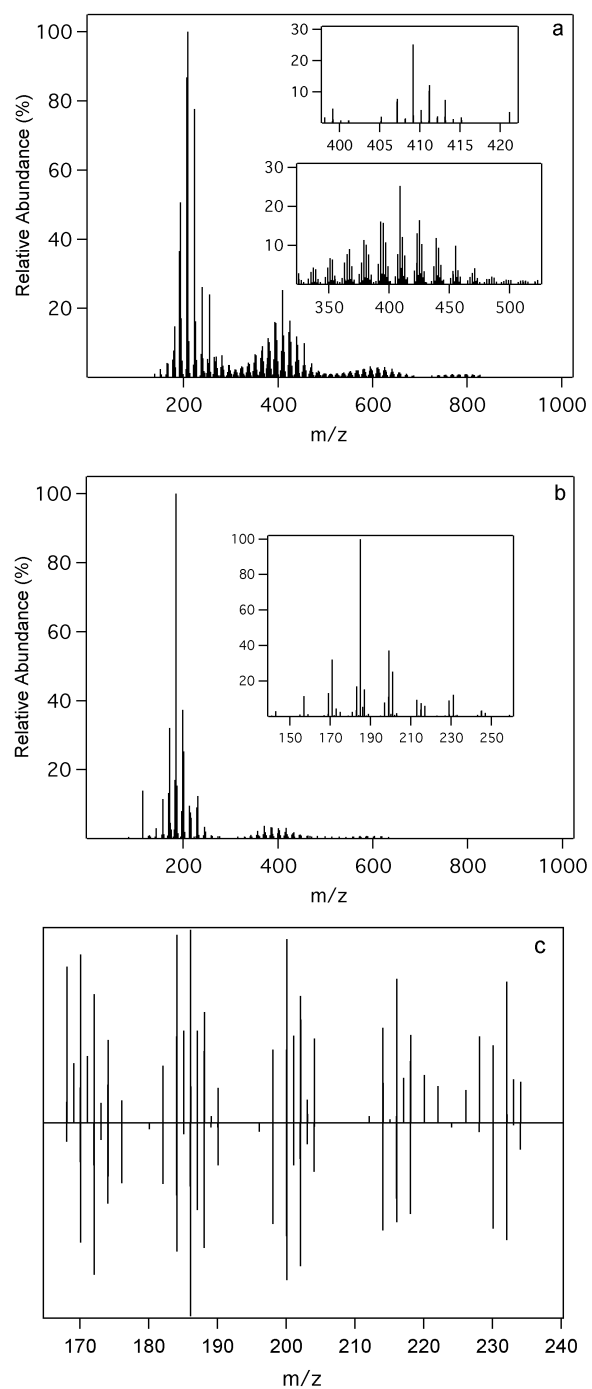


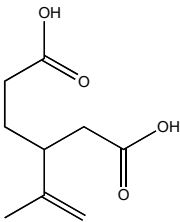
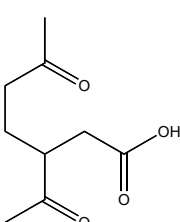
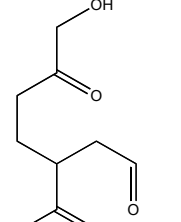
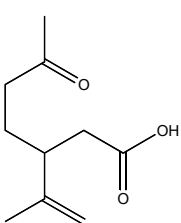
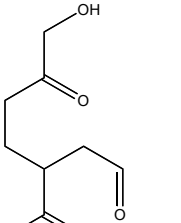
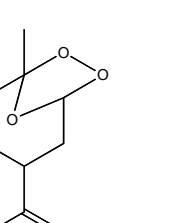
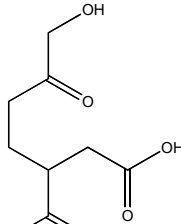
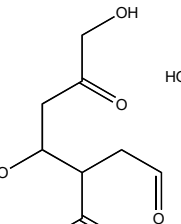
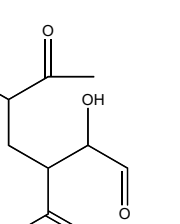
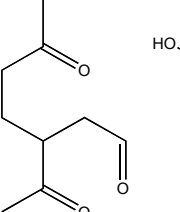
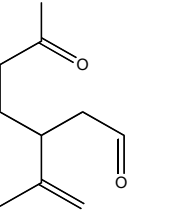
Figure 3.2: Representative ESI mass spectra of SOA particles. The data include peaks with $\geq 0.5\%$ abundance relative to the largest peak in the spectrum. a) Stick spectra in the positive and b) negative ion modes. c) Comparison of positive (up) and negative (down) mass-spectra on a logarithmic intensity scale after subtracting m/z of ^{23}Na from the positive m/z scale and adding m/z of ^1H to the negative m/z scale.

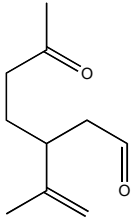
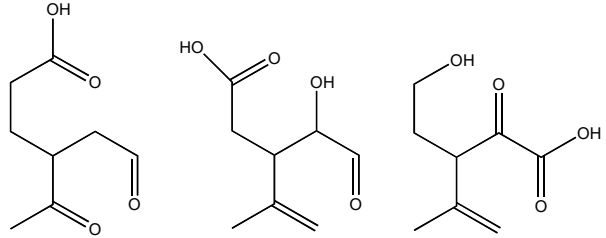
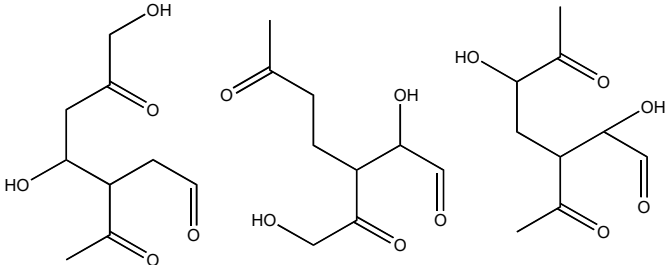
multiply charged ions ($z > 1$) in either positive or negative ion mode spectra.

The most abundant peaks in the positive and negative ion mode spectra, at m/z 209.0777 and 185.0817, respectively, were assigned to the same neutral precursor $C_9H_{14}O_4$, which most likely corresponds to limonic acid.⁶¹ This is not an isolated coincidence. Table 3.1 shows elemental composition and possible structural assignments for the 5 most abundant peaks measured in each ion mode. All of these species are simultaneously detected in both modes. Furthermore, there is a good correlation between the positions and intensities of $(M + 23)$ peaks in the positive ion mode spectrum and $(M - 1)$ peaks in the negative ion mode spectrum. To emphasize this point, Figure 3.2c explicitly compares the positive ion mode spectrum adjusted for the mass of one ^{23}Na atom and the negative ion mode spectrum adjusted for deprotonation. The spectra are compared on a logarithmic intensity scale in order to amplify smaller peaks. Although many peaks appear in both modes, there are also a significant number of peaks observed in only one ion mode, which indicates that data from both ion modes are necessary to characterize aerosol composition.

The spectra shown in Figure 3.2 correspond to SOA prepared by reacting 10 ppm ozone and 10 ppm limonene for 1 h. Spectra were also obtained at different limonene:ozone ratios (10:1 and 1:10) and at variable reaction times. A surprising result was that these spectra all had a similar overall appearance. In addition, the reaction conditions were modified to include an excess amount of an OH-scavenger (500 ppm of 2-butanol). Addition of the scavenger did not appear to significantly affect the resulting mass spectrum, suggesting that secondary reactions of OH did not play a significant role in the mechanism of SOA formation. SOA samples prepared

Table 3.1: Elemental composition for the five most abundant peaks observed in the positive and negative ESI ion modes. Species observed in both ion modes are labeled with asterisks. The MS/MS fragments are listed in the order of decreasing intensities. The structures are taken from the mechanism presented in Chapter 5.

Measured m/z	Relative Abundance	Ion Composition	Non-ionized Composition	MS/MS Fragments
<i>Positive Ion Mode</i>				
209.0777	100	$[\text{NaC}_9\text{H}_{14}\text{O}_4]^+$	$\text{C}_9\text{H}_{14}\text{O}_4^*$	-H ₂ O -“C ₂ H ₄ O ₂ ” -CO ₂ -“C ₂ H ₄ O ₃ ”
				
		Limonic Acid	Keto-Limononic Acid	Keto-7OH-Limononaldehyde
207.0984	87	$[\text{NaC}_{10}\text{H}_{16}\text{O}_3]^+$	$\text{C}_{10}\text{H}_{16}\text{O}_3^{**}$	-H ₂ O -HCOOH
				
		Limonic Acid	7OH-Limononaldehyde	Endo-ozonide
223.0933	78	$[\text{NaC}_{10}\text{H}_{16}\text{O}_4]^+$	$\text{C}_{10}\text{H}_{16}\text{O}_4^{***}$	-H ₂ O -“C ₃ H ₆ O” -CO ₂ -O ₂ other peaks
				
		7OH-Limononic Acid		
193.0827	51	$[\text{NaC}_9\text{H}_{14}\text{O}_3]^+$	$\text{C}_9\text{H}_{14}\text{O}_3$	-H ₂ O
				
		Keto-Limononaldehyde	Limonic Acid	

Measured m/z	Relative Abundance	Ion Composition	Non-ionized Composition	MS/MS Fragments
191.1036	37	$[\text{NaC}_{10}\text{H}_{16}\text{O}_2]^+$	$\text{C}_{10}\text{H}_{16}\text{O}_2$	no fragmentation
				
		Limononaldehyde		
<i>Negative Ion Mode</i>				
185.0817	100	$[\text{C}_9\text{H}_{13}\text{O}_4]^-$	$\text{C}_9\text{H}_{14}\text{O}_4^*$	-“ $\text{C}_4\text{H}_6\text{O}$ ” - CO_2 - H_2O - $(\text{H}_2\text{O}+\text{CO}_2)$
		see above for possible structures (Positive ion mode, m/z 209.0777)		
199.0974	37	$[\text{C}_{10}\text{H}_{15}\text{O}_4]^-$	$\text{C}_{10}\text{H}_{16}\text{O}_4^{***}$	- H_2O - $(\text{H}_2\text{O}+\text{CO}_2)$ -“ $\text{C}_4\text{H}_6\text{O}$ ” - CO_2
		see above for possible structures (Positive ion mode, m/z 223.0933)		
171.0661	32	$[\text{C}_8\text{H}_{11}\text{O}_4]^-$	$\text{C}_8\text{H}_{12}\text{O}_4$	- CO_2 - H_2O - $(\text{H}_2\text{O}+\text{CO}_2)$ -“ $\text{C}_4\text{H}_6\text{O}$ ”
				
		Keto-limonalic Acid		
201.0766	25	$[\text{C}_9\text{H}_{13}\text{O}_5]^-$	$\text{C}_9\text{H}_{14}\text{O}_5$	- H_2O - $(\text{H}_2\text{O}+\text{CO}_2)$ - CO_2
				
183.1024	17	$[\text{C}_{10}\text{H}_{15}\text{O}_3]^-$	$\text{C}_{10}\text{H}_{16}\text{O}_3^{**}$	- CO_2 - H_2O - $(\text{H}_2\text{O}+\text{CO}_2)$
		see above for possible structures (Positive ion mode, m/z 207.0984)		

using lower concentrations or a scavenger were all extracted in methanol and compared to the methanol analog of the sample shown in Figure 3.2.

To avoid complications arising from solvent effects (see Appendix I), the analysis described below corresponds to mass spectra that used acetonitrile as the extracting solvent. Two representative mass-spectra recorded in acetonitrile were selected for a detailed analysis. In the negative ion mode, all peaks above the 0.5% intensity cutoff were assigned a unique elemental composition assuming that the majority of peaks contain only ^{12}C , ^{13}C , ^{16}O , and ^1H isotopes. We explicitly verified that all major peaks in the spectra had a neighboring peak at $m/z + 1.0034$ corresponding to incorporation of one ^{13}C atom. Furthermore, the ratio of intensities of ^{13}C - and ^{12}C -containing peaks was close to the expected $n_c \times 0.0108$, where n_c is the number of carbon atoms in the molecules. Nine such ^{13}C -containing peaks were found in the monomer region ($m/z < 300$) of the negative spectrum above the 0.5% intensity cutoff. In the positive ion spectra, the peaks were forced to contain one ^{23}Na atom in addition to ^{12}C , ^{13}C , ^{16}O , and ^1H . Seventeen ^{13}C -containing peaks in the monomer region were found to be above the 0.5% intensity threshold in the positive spectrum. Although these ^{13}C peaks do not add additional information about SOA composition, they can be used to confirm the validity of the peak assignments.

The assignments were further examined for self-consistency on a peak-by-peak basis. A few initial assignments had either unphysical elemental ratios (e.g., C:H > 1) or resulted in obvious outliers in the mass-defect plots. Such assignments were manually corrected to provide a more physical elemental composition that was within the absolute mass uncertainty ($|\text{measured} - \text{predicted}| <$

~0.001 amu). A small number of peaks, generally less than 2% relative abundance, could not be assigned to a composition within these constraints; these peaks were excluded from further analysis.

The measured m/z values were further analyzed using the Kendrick approach,¹⁰³ which introduces a new mass scale alternative to the ^{12}C -based IUPAC scale. The new mass scale can be based on any chemical moiety; CH_2 and the oxygen atom are the most commonly used bases for the Kendrick analysis of complex mass spectra.¹⁰³ We illustrate this approach using a CH_2 Kendrick diagram that eliminates any mass defect due to the $^{12}\text{CH}_2$ group as an example. The Kendrick mass (KM_{CH_2}) is calculated by re-normalizing the IUPAC scale to the CH_2 Kendrick scale that equates the exact mass of the $^{12}\text{CH}_2$ group to 14.0000 amu. The Kendrick mass defect (KMD) is calculated as the difference between the nominal value of KM (rounded up to the nearest integer) and KM.

$$\text{KM}_{\text{CH}_2} = (m/z) \times \frac{14.00000}{14.01565} \quad (3.I)$$

$$\text{KMD}_{\text{CH}_2} = \text{Nominal KM}_{\text{CH}_2} - \text{KM}_{\text{CH}_2} \quad (3.II)$$

Kendrick plots are constructed by plotting the values of KMD_{CH_2} vs. KM_{CH_2} . The advantage of this approach is that KMD_{CH_2} values are identical for families of species that differ from each other only by the number of CH_2 groups, and such series are found on horizontal lines on the plot. The peaks were also analyzed by an analogous method in which the measured m/z were normalized to a mass scale in which the m/z of the ^{16}O atom is 16.0000 amu.

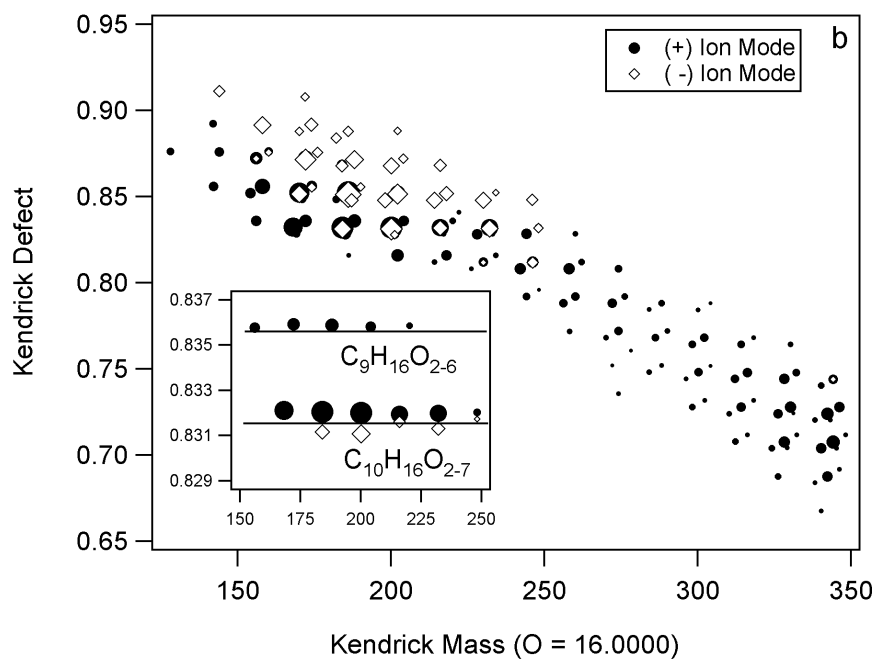
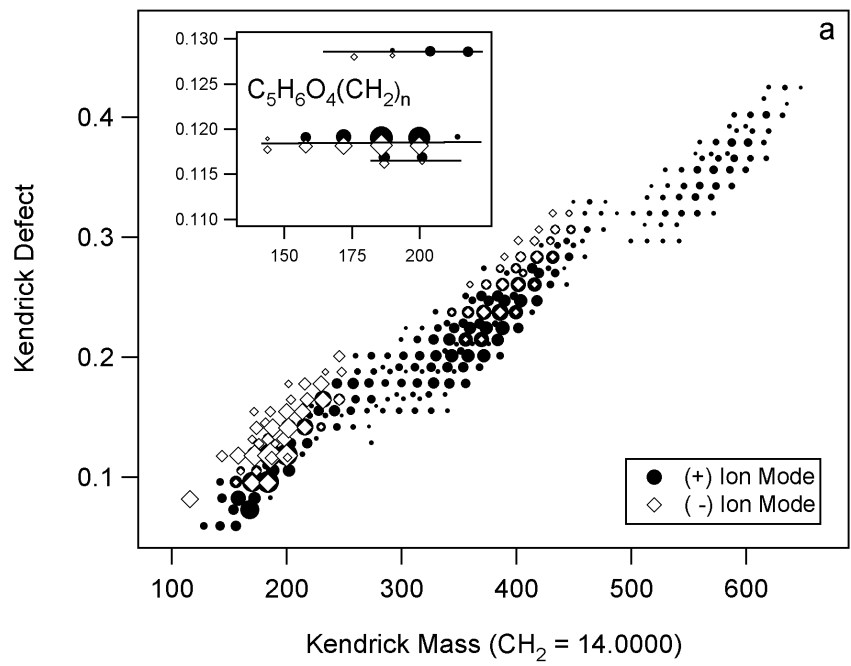
$$\text{KM}_o = (m/z) \times \frac{16.00000}{15.99492} \quad (3. \text{III})$$

$$\text{KMD}_o = \text{Nominal KM}_o - \text{KM}_o \quad (3. \text{IV})$$

This transformation enables easy identification of families of species that differ from each other only by the number of oxygen atoms. To make our KMD_{CH_2} values directly comparable with the results of Reinhardt et al.³⁶ the nominal masses were calculated by rounding KM_{CH_2} up to the nearest integer; the same procedure was used for calculating nominal KM_o values.

Figure 3.3a shows a CH_2 -Kendrick plot, constructed using the data from both the positive and negative ion mode ESI spectra discussed earlier. For clarity, only data (including ^{13}C -containing peaks) above 1% relative abundance are shown. To make a meaningful comparison between positive and negative ion mode data, the KM_{CH_2} and KMD_{CH_2} values are calculated for the neutral precursors of the ions appearing in ESI mass-spectra. Specifically, the m/z values measured in the positive ion mode ($\text{M} + \text{Na}$) have been shifted down by 22.9898 amu, and the m/z values measured in the negative ion mode ($\text{M} - \text{H}$) have been shifted up by 1.0078 amu before calculating KM_{CH_2} and KMD_{CH_2} . The size of each point is proportional to the logarithm of the peak intensity. Figure 3.3 also provides a visual representation of the degree of overlap between peaks measured in the two modes. For species observed in both negative and positive ion mode spectra, the experimental values of KMD agree within the experimental precision, $|\text{KMD}^{(-)} - \text{KMD}^{(+)}| < \sim 0.001$ amu.

Points with identical mass defects forming lines parallel to the x -axis correspond to families of species $\text{C}_x\text{H}_y\text{O}_z(\text{CH}_2)_n$ with a fixed oxygen atom content ($x, y, z = \text{fixed}; n = \text{variable}$) and different values of n . For example, one of the lines in



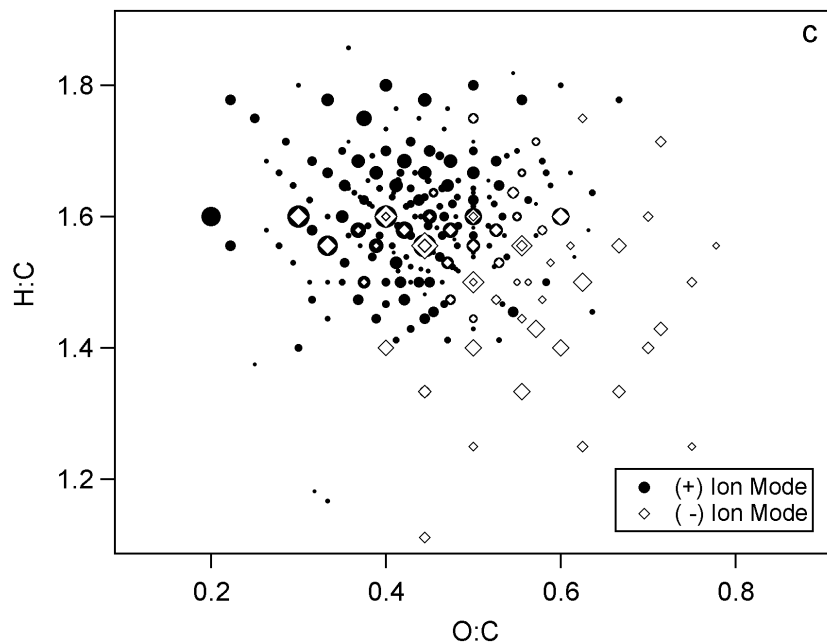


Figure 3.3: Data with $\geq 1.0\%$ relative abundance, obtained in the positive and negative ion modes: a) CH₂-Kendrick plot. Data were converted to a mass scale with CH₂ = 14.0000 amu. Species separated by CH₂ groups fall on horizontal lines. b) O-Kendrick plot. Data in the monomeric region of the spectra were converted to a mass scale with O = 16.0000 amu. Species separated by O atoms fall on horizontal lines. c) van Krevelen plot. A plot of the H:C atomic ratio versus the O:C atomic ratio provides a visual representation of the degree of oxidation of the SOA component species. The size of the data points in all plots is proportional to the logarithm of the peak intensity.

the inset to Figure 3.3a corresponds to a family C₅H₆O₄(CH₂)_n with *n* ranging from 0-4 for negative ions and from 2-6 for positive ions. Average experimental values of KMD_{CH₂} for this family are 0.1183 (negative ions) and 0.1191 (positive ions), which is equal to the predicted KMD_{CH₂} of 0.1186 within the experimental error in *m/z*. For the data sets used in this analysis, such *n*-families generally contain up to 8 and 6 members in the positive and negative ion mode spectra, respectively.

For species containing only carbon, hydrogen, and oxygen, a larger Kendrick defect generally implies a higher degree of oxidation. To illustrate this point, Table

3.2 shows expected values for the ratio of KMD_{CH_2} to KM_{CH_2} for several polymers and for CO_2 . For our SOA samples, the observed magnitude of KMD_{CH_2} increases with KM_{CH_2} with a slope of $\sim 7 \times 10^{-4}$, which is approaching a value characteristic of heavily oxidized polyethylene. There is also a slight downward shift in the slope between the monomer and dimer, and between the dimer and trimer, regions of the plot, indicating a decreasing O:C ratio with mass, which is also seen in α pinene SOA mass spectra.³⁶

Table 3.2: Kendrick data for representative oxygenated organic species. Expected slope of KMD_{CH_2} vs. KM_{CH_2} for several model polymers with a variable degree of oxidation.

Family	Description	KMD/KM
$(\text{CH}_2)_n$	Polyethylene	0
$(\text{C}_2\text{H}_4\text{O})_n$	Polyol: OH on every second C-atom	5.22×10^{-4}
$(\text{CH}_2\text{O})_n$	Polyol: OH on every C-atom	7.65×10^{-4}
$(\text{C}_3\text{H}_4\text{O})_n$	Polycarbonyl: O on every third C-atom	6.49×10^{-4}
$(\text{C}_2\text{H}_2\text{O})_n$	Polycarbonyl: O on every second C-atom	8.66×10^{-4}
$(\text{CO})_n$	Polycarbonyl: O on every C-atom	1.30×10^{-3}
CO_2	Carbon dioxide	1.35×10^{-3}

In Figure 3.3b, data have been normalized to a mass scale in which the mass of $^{16}\text{O} = 16.0000$ amu. In this plot, points with identical mass defects fall along horizontal lines, indicating families of species separated from each other only by the number of oxygen atoms: $\text{C}_x\text{H}_y\text{O}_m$ ($x, y = \text{fixed}; m = \text{variable}$). The inset in Figure 3.3b shows two such families corresponding to $\text{C}_9\text{H}_{16}\text{O}_{2-6}$ (theoretical $\text{KMD}_\text{O} = 0.8353$) and $\text{C}_{10}\text{H}_{16}\text{O}_{2-7}$ (theoretical $\text{KMD}_\text{O} = 0.8315$). The observed values of m were surprisingly high, with addition of up to 7 oxygen atoms observed in the monomeric region ($m/z < 300$; Figure 3.3b). This is consistent with a similar

observation of highly oxidized species $C_{10}H_{16}O_5$ and $C_{10}H_{16}O_6$ in a previous mass-spectrometric study of the ozone-initiated oxidation of limonene.⁹⁴

Figure 3.3c shows a van Krevelen diagram of the atomic ratio of hydrogen to carbon plotted versus the atomic ratio of oxygen to carbon.¹⁰⁴ Approximately 70% of the peaks have an O:C ratio between 0.4 and 0.6. Species with O:C ratios greater than 0.6 are generally detected in the negative mode, while species with O:C ratios smaller than 0.4 are more readily seen in the positive ion mode. The average O:C ratios calculated using peak intensities as weighting factors are 0.43 and 0.50 determined from the positive and negative ion mode spectra, respectively. This corresponds to an impressively high degree of oxidation, wherein every second carbon atom is bonded to an oxygen atom.

Most peaks have an H:C ratio smaller than 1.6, which is the H:C ratio of limonene itself. However, a number of peaks with H:C in excess of 1.6 are also observed: in the positive ion mode, 50% of peaks have an H:C ratio larger than 1.6, while in the negative ion mode, that percentage decreases to approximately 30%. The general properties of the plot agree with the recent analysis of α -pinene SOA.³⁶

Selected peaks were fragmented in the linear ion trap in an attempt to distinguish between possible isomeric structures. All major peaks in the monomeric region displayed a fairly similar fragmentation pattern with subtle differences between relative intensities of various fragmentation pathways (Table 3.1). Loss of H_2O or CO_2 was the most common fragmentation pathway for both positive and negative ions. Negative ions also lost H_2O and CO_2 simultaneously, whereas the corresponding positive ions did not. Some negative ions lost a fragment

corresponding to C_4H_6O . Losses of fragments corresponding to CH_2O_2 , $C_2H_4O_3$, and C_3H_6O were observed for some positive ions. To interpret these observations, we are currently in the process of studying fragmentation patterns for pure compounds with a similar degree of oxidation.

The mass spectra discussed above contain a surprisingly large number of peaks, well beyond the number of products described in previous studies of limonene ozonation. Even with the benefit of knowledge of elemental compositions of every peak, it is close to impossible, not to mention impractical, to assign all peaks to specific molecular structures. However, one can test whether known chemistry of the ozonation of olefins is consistent with the large number of observed products, and whether it correctly predicts the atomic ratios of the SOA constituents.

Figure 3.4 compares a) the KM_{CH_2} and KMD_{CH_2} values and b) the H:C versus O:C ratios predicted by the mechanisms outlined in Chapter 5 with those measured using high-resolution mass spectrometry in both the positive and negative ion modes. Predicted masses were generated from the masses of the first generation products, as well as the possible mass increases and decreases resulting from the subsequent reactions of first generation products. The experimental points plotted in Figure 3.4 correspond to the measured m/z values minus m/z of ^{23}Na (22.9898 amu) and plus m/z of 1H (1.0078 amu) to account for the ionization mechanisms in positive and negative ion modes, respectively.

Comparison of the predicted and measured mass defects gives credence to the qualitative validity of the proposed mechanism. In addition to the good agreement between the number of observed and predicted peaks, the magnitudes of the mass

defects are similar. The agreement between measured and predicted masses is better at higher masses than at lower masses. It is likely that the lower mass products predicted by our mechanism have a high enough vapor pressure that they exist in the gas phase rather than the aerosol phase under our experimental conditions. If this were the case, these lower masses would not have been detected, as we analyzed only those products that remained in the filtered SOA particles.

As discussed earlier, the Kendrick representation allows for the identification of homologous species separated by $-\text{CH}_2$. Figure 3.4a shows 3 horizontal lines that highlight such series, with composition $\text{C}_x\text{H}_y\text{O}_z(\text{CH}_2)_n$. As the degree of oxidation, and hence the value of z , increases, the Kendrick mass defect becomes larger, as shown by the lines in Figure 3.4a.

One would expect oxidized limonene products to have H:C ratios that are smaller than 1.6, the H:C ratio of limonene itself. We find that a large number of products have an H:C ratio in excess of 1.6 (Figures 3.3c, 3.4b). A similar observation was made in the high-resolution mass-spectrometric analysis of SOA produced by the ozonolysis of α -pinene, and attributed to unspecified secondary hydrogenation reactions.³⁶ Indeed, condensation reactions of the initial products with small molecules with $\text{H:C} > 1.6$ (e.g., formaldehyde or water) would increase the H:C ratios. However, Figure 3.4b shows that the proposed mechanism generates products with an H:C ratio > 1.6 without having to postulate hydrogenation chemistry. For example, the loss of CO_2 during decomposition of carbonyl oxides increases the H:C ratio. Additionally, formation of a stable alcohol through RO_2 self-reactions results in

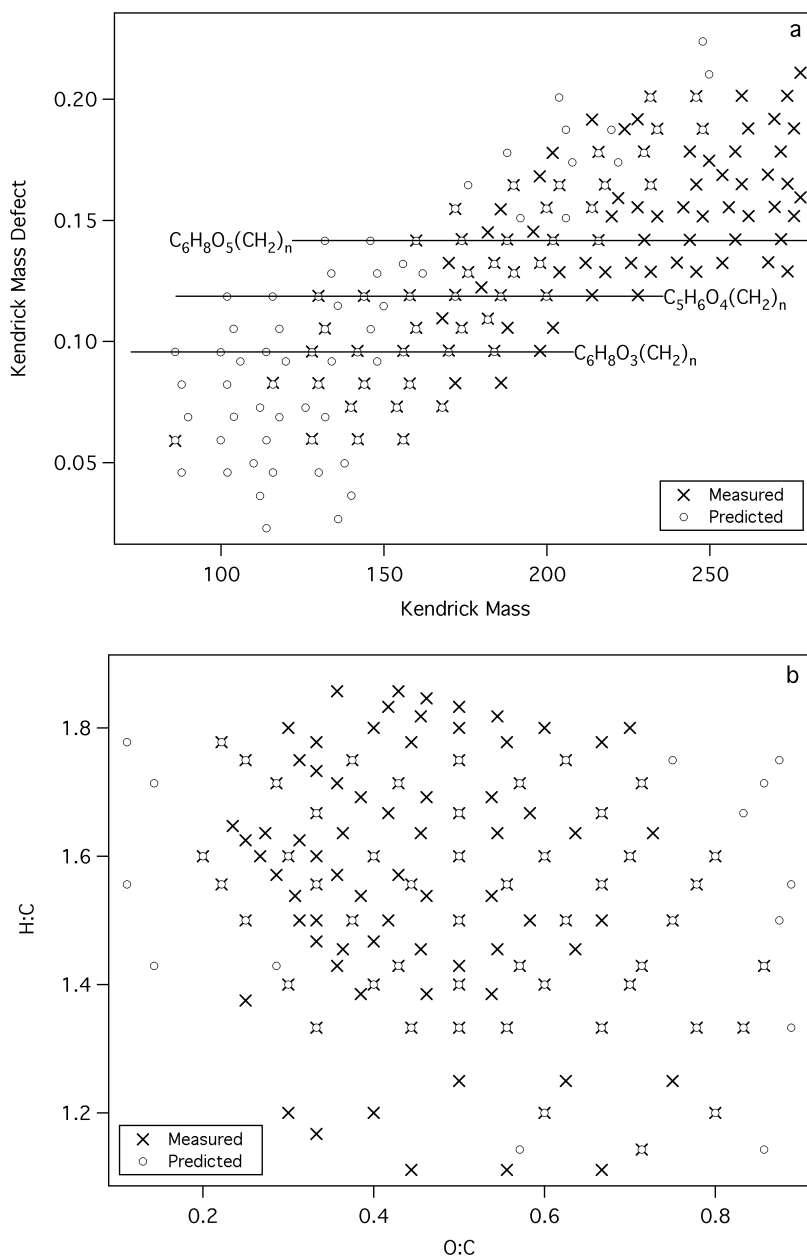


Figure 3.4: Comparison of measured and predicted SOA components. a) The CH_2 -Kendrick mass system is used to compare the masses measured in both ion modes with the masses predicted by the oxidation mechanisms outlined in Chapter 5. b) A van Krevelen diagram is used to compare the H:C and O:C ratios measured in both ion modes with the ratios predicted by our mechanism. Open circles represent peaks predicted by the empirical reaction mechanism and crosses represent peaks measured in the positive and/or negative ion modes.

addition of a hydrogen atom without addition of a carbon atom, which also increases the H:C ratio.

Conclusion

High-resolution mass spectrometric characterization of SOA particles formed from the ozone-induced oxidation of limonene demonstrated that the composition of these particles is significantly more complex than that predicted by the basic Criegee mechanism of alkene ozonolysis. To account for the very large number of polyfunctional species that exist in SOA in both monomeric and polymeric form, one has to include rich chemistry involving alkylperoxy and alkoxy radicals formed from the decomposition of carbonyl oxide intermediates. This work shows that, even with a fairly restrictive set of reaction rules, inclusion of alkylperoxy and alkoxy chemistry in limonene ozonation produces some 1100 products with 140 unique m/z values in the monomeric mass range ($m/z < 300$). The large number of isomeric products produced in the oxidation of just one terpene shows how challenging it will be to obtain detailed characterization of molecular composition of ambient SOA particles.

We take advantage of both the positive and negative ion mode mass-spectra, which allows the identification of a more complete set of SOA species. The similarities and differences between spectra obtained in the two ion modes clearly show that complementary information is obtained by using both modes. Our analysis shows that more oxidized species (e.g. carboxylic acids vs corresponding aldehydes) are more readily detected in the negative ion mode. The use of Kendrick and van Krevelen analysis, tools commonly used in mass spectrometry of complex mixtures,

allows the identification of homologous series of products with varying degrees of oxidation. Analysis of oligomeric species ($m/z > 300$) is currently underway, and this, along with a proposed mechanism for oligomer formation, will be presented in another publication.

CHAPTER 4

PHOTOCHEMISTRY

*Reproduced in part with permission from J. Phys. Chem. A, 2007, 111, 1907-1913.
Copyright © 2007 American Chemical Society*

Introduction

Atmospheric aerosol particles play an important role in controlling global climate and air quality.^{8,22,74,105-107} A large fraction of organic aerosol particles are formed as secondary organic aerosol (SOA) resulting from the condensation of partially oxidized volatile organic compounds (VOC), or as a result of VOC oxidation chemistry within cloud droplets. Because urban organic aerosol are often secondary in nature, such particles and their chemistry are of particular interest to atmospheric scientists.^{23,24,86-93}

As discussed in earlier chapters, monoterpenes are responsible for a significant fraction of biogenic VOC emissions.²⁷ Atmospheric oxidation of carbon-carbon double bonds in monoterpenes produces a variety of polyfunctional species, including alcohols, aldehydes, ketones, and carboxylic acids, which generally have lower vapor pressures than the parent terpenes, and can condense to form aerosol particles. Since Went's work in 1960³⁷ SOA yields, reaction mechanisms, and particle composition have been extensively studied for the ozonolysis of monoterpenes in smog chambers and in simulated indoor environments, as detailed in Chapter 2.

Current knowledge of terpene oxidation by O₃, OH, and NO₃ consists of gas- and condensed-phase products,^{48,56} and how various factors, such as relative

humidity, UV radiation, and NO_x concentration, affect the aerosol yield.^{26,46,75,76} Once SOA particles are formed, they undergo both physical and chemical aging processes, which may result in large effects on the physicochemical properties of the particles, including their toxicity and ability to nucleate rain droplets. Atmospheric particles are exposed to sunlight 8-14 hours a day, therefore photochemical processes are likely to be among the primary aging mechanisms. The direct effects of solar UV radiation on the composition and chemistry of monoterpene-derived SOA are currently unknown. However, recent laboratory observations of a reduction of SOA yields in the presence of UV radiation give strong evidence for the potential importance of such processes.^{46,75,109,110}

The work presented in this chapter focuses on the photochemical aging of model SOA particles resulting from the oxidation of d-limonene vapor by ozone. An experimental investigation of the absorption of radiation in the actinic region of the solar spectrum ($\lambda > 295$ nm) by SOA particles is presented. Additionally, the extent to which photochemical processes can efficiently compete with other organic aerosol aging and removal processes in the atmosphere is discussed.

Experimental

Particle generation

Model SOA particles were formed from the ozone-initiated oxidation of d-limonene vapor in an inflatable Teflon reaction chamber (Figure 4.1). A fan was used to ensure rapid mixing of ozone and limonene in the chamber. The chamber was first filled to approximately 250 L with dry purified air or, for experiments performed

at increased relative humidity (RH), with air from a Nafion humidifier. Ozone, produced by flowing oxygen (99.994% purity) through a commercial ozone generator, was added to the reaction chamber to achieve a concentration of ~ 300 ppm. Once the desired relative humidity and ozone concentration were achieved, a 50 sccm (standard cubic centimeters per minute) air flow saturated with d-limonene (97% purity, Fisher Scientific) was injected into the chamber over the course of 20 min. Saturated vapor was obtained by flowing air through a temperature-controlled bubbler containing limonene at $T = 298$ K (partial pressure of d-limonene = 260 Pa). In the absence of ozone, the final concentration of limonene in the 250 L chamber would be ~ 8 ppm, but this level was not achieved because oxidation and particle growth occurred in parallel with limonene addition. The resulting mixture was allowed to age in the dark, at room temperature (~ 298 K) and ambient pressure (~ 750 torr), for ~ 1 h before particle collection.

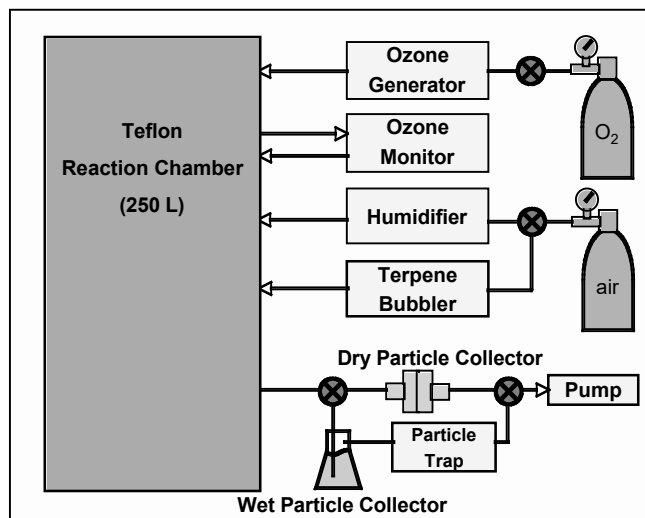


Figure 4.1: Aerosol generation setup. Limonene is allowed to react with ozone under darkness for approximately one hour before particle collection.

The particles are extracted in polar or non-polar solvents for UV/Vis analysis or collected on glass fiber filters for IR-CRDS analysis.

Particle collection

The wet particle collector (Figure 4.1) was used to capture and dissolve particles in a non-polar solvent by bubbling the aerosol/gas mixture from the reaction chamber through a flask filled with CH₂Cl₂. The particle size distribution was measured before and after the collector using a Scanning Mobility Particle Sizer (SMPS) to quantify the fraction of the collected particles. The size distribution did not change dramatically, indicating that the wet collector did not preferentially capture specific particle sizes. As a specific example, the mean particle diameter was 315 nm and the total particle number concentration was $4.1 \times 10^5 \text{ cm}^{-3}$ before the collector. After the collector, the mean diameter was 321 nm, and the total particle concentration was reduced to $3.4 \times 10^5 \text{ cm}^{-3}$ suggesting that ~17% of the particles were captured by the solvent. In the second approach (dry particle collector), the particles were first collected on a glass fiber filter over the course of ~10 min, and then ultrasonically extracted with either polar (CH₃OH) or non-polar (CH₂Cl₂) solvent. The particle filter collection efficiency was measured to be >95% for particles larger than 0.1 μm. Exposure to ambient light was minimized during the collection and extraction processes. As opposed to the wet collector, the extracts prepared this way were less likely to entrap gas-phase components of the reaction mixture.

Spectroscopic analysis

Absorption spectra of particles collected using both the wet- and dry-collection methods were recorded in standard 1 cm quartz cuvettes using a Varian Cary 50 UV/Vis spectrophotometer.

For photolysis experiments, the filters with freshly collected particles were placed in a sample holder for analysis using the infrared cavity ring-down spectroscopy (IR-CRDS) system shown in Figure 4.2. The IR-CRDS system has been described elsewhere,^{111,112} but it was modified slightly to accept filters with collected SOA as samples. Briefly, the apparatus consists of a cavity created by two highly reflective mirrors (99.98% at 3.3 μm ; suitable for detection of C-H stretching vibrations in organic molecules) spaced by approximately 60 cm. A quartz sample tube (15 mm ID) is located between the mirrors, and the cavity is pumped by an infrared optical parametric oscillator laser. The SOA particles collected on a filter are exposed to UV radiation from a Xenon lamp, passed through a 295 nm high-pass filter or, for wavelength dependent experiments, a monochromator with ~ 10 nm resolution. An optoacoustic reference spectrum of HCOOH vapor (1 torr of HCOOH in 10-100 torr N_2 buffer) is recorded in parallel with each IR-CRDS spectrum for wavelength calibration purposes.

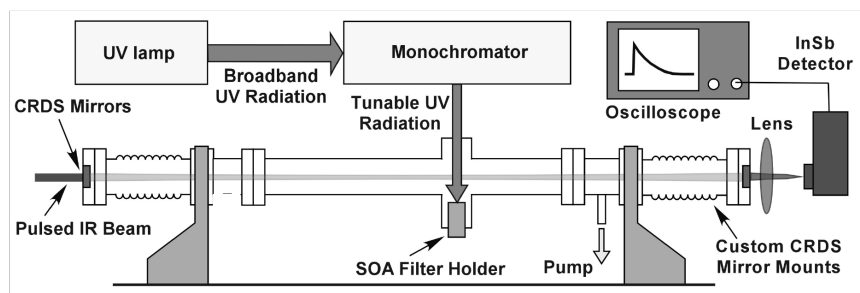


Figure 4.2: IR-CRDS setup. SOA particles collected on glass fiber filters are placed in a quartz flow tube and exposed to tunable UV radiation. Gas-phase products are detected using IR-CRDS along the flow tube axis.

The system was operated in one of two modes, depending on the goals of the experiment. In the first mode, the particles were exposed to UV light and the IR wavelength was scanned in order to identify gas-phase reaction products via their unique rovibrational transitions. Alternatively, the IR wavelength was kept constant, and the production of a specific photolysis product, formic acid in this discussion, was measured as a function of UV wavelength to obtain a photodissociation action spectrum. All photolysis experiments were carried out at room temperature (298 K) under slow flow conditions (~1-5 s cavity flushing time) using ultra-high purity N₂ as a bath gas at 7-9 torr. Before photolysis, the SOA on the filter was allowed to sit in darkness at low pressure for ~10-15 min. The background signal was very low over this time period, indicating that evaporation of particle components to the gas phase was minimal.

Results and discussion

Ultraviolet absorption spectra

Figure 4.3a compares the UV absorption spectrum obtained by wet collection of SOA particles with that of a limonene reference solution. To ensure a meaningful comparison, the limonene mass concentration (110 mg/L) in the reference solution is kept roughly equal to the mass concentration of reacted limonene in the SOA extract. The latter is estimated from the measured particle collection efficiency and from a simplifying assumption that a large mass fraction of oxidized limonene products ends

up in the SOA particles. This assumption is reasonable as ozonolysis of limonene at ppm concentrations is expected to produce SOA in fairly high mass yields.²⁵ Figure 4.3b similarly compares UV absorption spectra of limonene and of SOA particles collected on filters and ultrasonically extracted with either methanol or dichloromethane.

The absorption spectra of the SOA extracts are characterized by a smooth decrease in the absorption cross-section between 250 and 350 nm, and they are clearly different from the spectrum of the parent terpene molecule. The most obvious change is the large red-shift in the SOA spectra, which is observed for SOA extracted with both polar (CH_3OH) and non-polar (CH_2Cl_2) solvents. This red-shift significantly improves the overlap with the solar spectral radiant flux density, which is dominated by wavelengths in excess of 300 nm in the lower atmosphere.

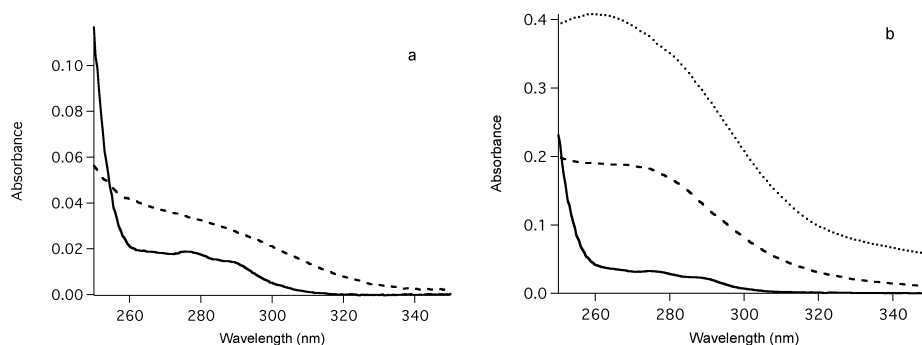


Figure 4.3: UV/Vis spectra of limonene and aerosol particles. a) Spectra of reference limonene solution (solid) and SOA generated from the ozone-initiated oxidation of limonene (dashed), collected by bubbling through CH_2Cl_2 . b) Spectra of reference limonene solution (solid) and SOA collected on glass fiber filters and ultrasonically extracted into CH_2Cl_2 (long dash) and CH_3OH (short dash). The absorbance by limonene is strongly red-shifted by oxidation.

To assess the impact of RH on the photochemical properties of SOA particles, the UV absorption spectra of SOA prepared at RH < 5% and 75% were also compared. These spectra had a similar shape to the ones shown in Figure 4.3, but the absolute absorbance of the particles prepared at elevated RH was reproducibly larger than for those prepared in dry air. This observation is consistent with the increase in the mass yield of SOA from limonene ozonolysis by a factor of 2-3 at elevated RH (85% vs. <2%)²⁶ which was confirmed by our own measurements. Indeed, the total particle number concentration prepared at elevated RH was on occasions almost an order of magnitude larger than that for dry conditions. The particle size distribution shifted slightly towards smaller particles, with a mean particle diameter of ~270 nm for 75% RH and ~320 nm for <5% RH, resulting in the RH-induced enhancement in the total particle mass by a factor of 2-6, in qualitative agreement with data from Jonsson et al.²⁶

Photodissociation action spectra

Limonene SOA collected on glass fiber filters were photolyzed with a broadband UV source ($\lambda > 295$ nm) in the IR-CRDS setup shown in Figure 4.2. The resulting IR spectra of gas-phase photolysis products (Figure 4.4) contained characteristic rovibrational lines that could be unambiguously assigned to formic acid and formaldehyde based on an explicit comparison with their reference IR spectra. We explicitly verified that formic acid and formaldehyde emissions were not caused by radiative heating of the sample. Furthermore, there were no formic acid and formaldehyde lines observed from a clean filter, from a clean filter exposed to either

ozone or UV radiation, or from unoxidized limonene adsorbed on a filter exposed to UV radiation.

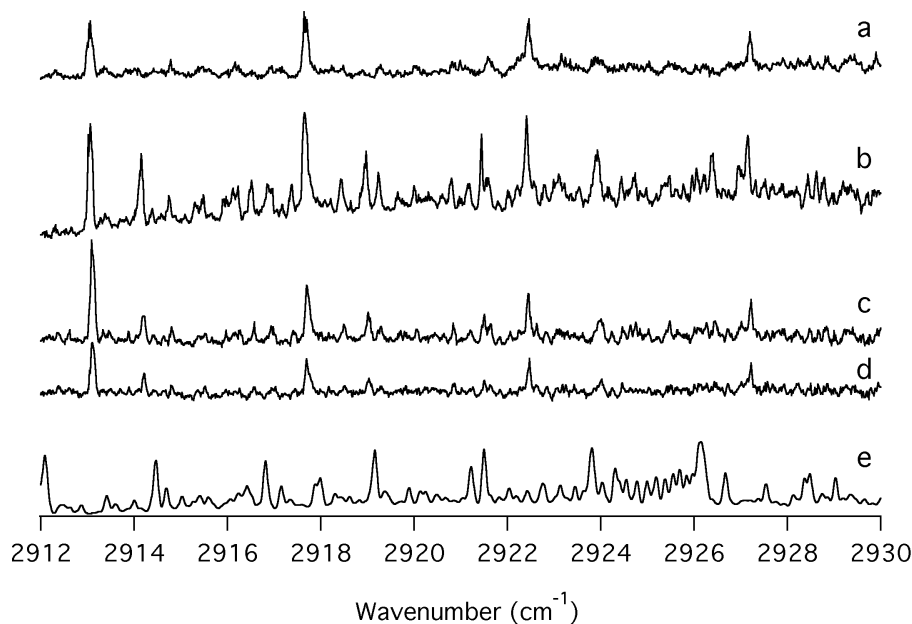


Figure 4.4: IR-CRDS spectra resulting from broad photolysis ($\lambda > 295$ nm.) (a) Formic acid reference optoacoustic spectrum. (b) Representative SOA spectra taken at $t=0$ min, (c) 10 min, and (d) 20 min after photolysis. (e) Formaldehyde reference spectrum.

It is likely that larger volatile organic molecules were also emitted by the SOA sample before and/or during photolysis. However, molecules containing more than 2-3 non-hydrogen atoms are not expected to have rotationally resolved spectra at the 0.1 cm^{-1} resolution of the IR laser used in these experiments. Such molecules contribute to the background absorbance that changes with IR wavelength slowly (typical width of a CH-stretching IR band is $20\text{-}30 \text{ cm}^{-1}$), and is hard to distinguish from instrumental drifts in the cavity ring-down time. The broad absorbance underlying resolved rotational lines in trace b of Figure 4.4 may be the result of such unresolved absorption by gas-phase products of SOA photolysis that are larger than

formaldehyde and formic acid. Figure 4.4 shows that the unresolved absorbance is not overwhelmingly large, and that it disappears from the IR spectra after 10-20 min of photolysis. Our laboratory is currently studying the nature of these unidentified photolysis products with mass-spectrometric techniques; results of this study will be reported elsewhere.¹¹³

Figure 4.4 reveals that the IR spectrum changed with photolysis time as a result of photobleaching of the SOA sample and/or secondary photochemical processes occurring on the filter. Under present experimental conditions, the formic acid signal decayed with a time constant of about 30 min. The formaldehyde signal disappeared somewhat faster, suggesting that it came from a different photochemical precursor than formic acid. Secondary photolysis of formaldehyde that was produced by photolysis, but did not immediately desorb from the filter, may also have contributed to the more rapid decay of the formaldehyde signal.

Reactions between aerosol species and the products of formaldehyde photolysis are not likely to be significant. Under our experimental conditions, the formaldehyde photolysis rate is on the order of $2 \times 10^{-4} \text{ s}^{-1}$, which corresponds to a lifetime on the order of an hour. This is relatively long-lived compared to the timescale of our experiment (10-15 min). Also, the cell operates in a continuous flow mode; as formaldehyde photolysis products enter the gas phase, they are flushed from the cell within a few seconds. As such, secondary photolysis of gas-phase products can be ruled out because of the short CRDS cell flushing time (1-5 s).

Because of photobleaching, the photodissociation action spectrum could not be obtained by simply exposing the same SOA sample to different photolysis

wavelengths, and recording the IR spectrum of the resulting gas-phase products. To circumvent this problem, SOA particles were simultaneously collected from the reaction chamber on six separate filters. Each filter was then placed in the IR-CRDS setup and exposed to a different photolysis wavelength under otherwise identical conditions. The amount of photolysis products observed at every UV wavelength was normalized to that observed at an arbitrarily selected reference wavelength of 270 nm, allowing for an easy comparison of action spectra obtained under different SOA generation conditions.

The signal measured as a function of the UV irradiation wavelength at a strong formic acid absorption line at $\sim 2816\text{ cm}^{-1}$ was used as a measure of relative SOA photolysis rates. Figure 4.5 shows this signal for different photolysis wavelengths as a function of photolysis time. The signal follows a characteristic exponential rise and decay curve. The decay time (5-10 min) can be attributed to the photobleaching of the sample, while the rise time (40-50 s) is controlled by a combination of CRDS cell purging ($\sim 2\text{ s}$) and establishment of equilibrium between gas-phase and wall-adsorbed formic acid.

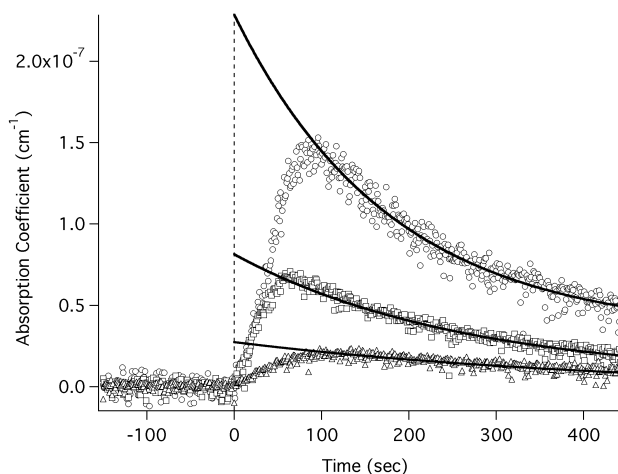


Figure 4.5: Time dependent IR-CRDS signals. IR-CRDS signals as a function of photolysis time for representative photolysis wavelengths (○ 270 nm; □ 290 nm; △ 310 nm).

The decaying portion of the traces shown in Figure 4.5 was extrapolated to zero time to obtain the wavelength-dependent relative photolysis rate before the SOA sample was significantly affected by photobleaching. Figure 4.6 shows the resulting relative yields of formic acid during photolysis of limonene SOA as a function of UV photolysis wavelength (i.e., photodissociation action spectrum). All data were normalized to the 270 nm formic acid signal as described above, and further corrected for the intensity of the photolysis light (assuming that the photolysis signal is linear in photolysis power).

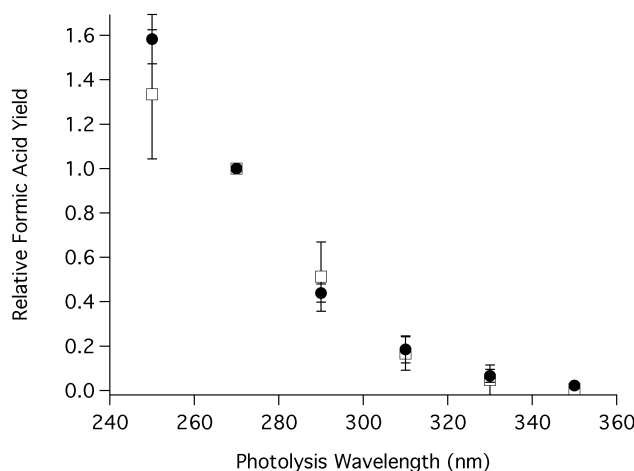


Figure 4.6: Limonene SOA formic acid action spectra. Action spectra of limonene SOA prepared at <5% RH (filled circles) and 75% RH (open squares). The data were arbitrarily normalized to the formic acid signal observed at 270 nm.

The effect of relative humidity on the photodissociation action spectrum was also investigated using limonene SOA. As shown in Figure 4.6, the shape of the action spectra for limonene-derived SOA prepared in dry air (<5% RH) and at 75%

RH are very similar, indicating that humidity has little to no effect on the wavelength dependence of the formic acid yield. The absolute photodissociation yields of formic acid at different humidities could not be straightforwardly compared. We note that UV absorption spectra for SOA prepared in dry air and at elevated relative humidity also had similar shapes but different absolute values.

Atmospheric implications

The results of this investigation indicate that solar radiation may play a significant role in the processing of SOA in the atmosphere. Indeed, the absorption spectrum of SOA generated by oxidation of limonene (Figure 4.3) shows measurable absorbance in the actinic region of the solar spectrum, i.e., at wavelengths capable of reaching the lower atmosphere ($\lambda > 295$ nm). Clearly the oxidation products that condense to form the SOA particles must contain functional groups capable of absorbing mild UV radiation – a key prerequisite for photochemistry in atmospheric aerosol particles. UV radiation has already been shown to have an effect on the yield of terpene-derived SOA,^{46,75,109,110} and this work shows that radiation continues to affect the chemical composition of SOA after particle formation.

The absorption spectrum in Figure 4.3 can be used to obtain an order of magnitude estimate of the effective absorption cross section of oxidized limonene molecules. For example, dissolved SOA particles absorb roughly as much radiation at 300 nm as an approximately equivalent amount of limonene does at 280 nm. The latter is characterized by an absorption cross section of 3.6×10^{-20} cm² molec⁻¹ ($\epsilon = 21.6$ L mol⁻¹ cm⁻¹; estimated from the reference spectrum shown in Figure 4.3).

Although this is not a large value, photochemistry in the lower atmosphere is often driven by similarly weak absorptions in the actinic region. For example, the absorption cross section of acetone at 300 nm is $2.77 \times 10^{-20} \text{ cm}^2 \text{ molec}^{-1}$, and this is sufficient to make the lifetime of acetone in the upper troposphere be controlled by photolysis, and also make acetone a significant source of HO_x.¹¹⁴

It is instructive to estimate the effective photolysis lifetime for molecules in limonene SOA particles. The photolysis rate constant, k_p , can be calculated from the wavelength dependent quantum yield, $\phi(\lambda)$, absorption cross-section, $\sigma(\lambda)$, and solar radiant flux density, $F(\lambda)$, convoluted over the relevant wavelength range.

$$k_p = \int_{\lambda} \phi(\lambda)\sigma(\lambda)F(\lambda)d\lambda \quad (4.I)$$

The photolysis lifetime is simply the inverse of the photolysis rate constant. Using the absorption cross-sections obtained by scaling the measured relative photodissociation cross-sections shown in Figure 4.6 to the estimated 300 nm value results in a photolysis lifetime of about 4.7×10^5 s, calculated for zero solar zenith angle, best-estimate surface albedo, and a photolysis quantum yield of unity.^{8,115}

Reaction with hydroxyl radical is likely to be the most important competing aging mechanism for organic species within the SOA particles. For $[\text{OH}] = 10^6 \text{ molec cm}^{-3}$, the lifetime of SOA organic species with respect to OH attack should be on the order of 10^5 s (assuming a surface reaction probability for OH of 0.1 on solid organic surfaces).¹¹⁶ However, only the molecules on the surface of the SOA particles should be susceptible to chemical aging, whereas radiation is likely to penetrate deeper and cause photochemical aging throughout the entire particle.

Therefore, the rate of photochemical aging of SOA particles in the atmosphere is likely to be comparable to, if not larger than, the rate of chemical aging due to OH attacks.

The ozonolysis of monoterpenes has been studied by many research groups and the reaction mechanism is reasonably well understood,^{26,52,56,75,100} Amongst the impressively large number of identified products of ozonolysis of monoterpenes, organic peroxides, aldehydes, and ketones are the most likely candidates for the observed weak optical absorption by SOA in the actinic region. Most of the condensable reaction products are expected to be better absorbers at $\lambda > 295$ nm than limonene itself, in agreement with our observations (Figure 4.3).

The most likely ozonolysis product that can produce formic acid upon photolysis is the secondary ozonide (1,3,4-trioxalane) formed from the ozonolysis of the exocyclic double bond. The photolysis mechanism is similar to that of the secondary ozonides of undecylenic acid¹¹¹ and other olefins,^{112,117,118} and will be discussed in greater detail in Chapter 5.

A qualitative comparison of the absorption spectrum shown in Figure 4.3 and the photodissociation action spectrum shown in Figure 4.6 provides additional insights into the reaction mechanism. If the absorption and action spectra had more similar shapes, this would indicate that production of formic acid results from the photolysis of the primary absorber within the particles. However, if a fit of the action spectrum is appropriately scaled and subtracted from the absorption spectrum, there is remaining signal in the 300 nm region. This further confirms the presence of aldehyde and ketone functionalities detected using high-resolution mass spectrometry

(Chapter 3). Both these functional groups absorb UV radiation between about 260 and 310 nm, but do not produce formic acid as a photolysis product. Work is currently underway to quantify the production of CO, a marker for carbonyl photochemistry, from limonene-derived SOA photolysis.

Conclusion

SOA particles formed from the ozone-initiated oxidation of limonene have been found to absorb radiation in the actinic region of the solar spectrum ($\lambda > 295$ nm). The ozonolysis of limonene's two double bonds produces a variety of functional groups, including carbonyls and peroxides, which are responsible for the increased absorption of UV radiation. Furthermore, the resulting SOA particles are photochemically active in that they emit small volatile molecules (e.g. formaldehyde and formic acid) upon absorption of actinic radiation. While further work is needed to completely quantify this effect, it is quite probable that such photochemical processes can efficiently compete with other organic aerosol particle aging processes in the atmosphere.

CHAPTER 5

MECHANISM

*Reproduced in part with permission from Phys Chem Chem Phys
submitted for publication.*

*Unpublished work copyright © 2007 Royal Society of Chemistry.
and J. Phys. Chem. A, 2007, 111, 1907-1913.
Copyright © 2007 American Chemical Society*

Introduction

High-resolution mass spectra of limonene-derived secondary organic aerosol (SOA) reveal a large number of both monomeric ($m/z < 300$) and oligomeric ($m/z > 300$) products of oxidation (see Chapter 3). Here, an extended reaction mechanism for the formation of the first generation of SOA molecular components is proposed. The mechanism includes known isomerization and addition reactions of the carbonyl oxide intermediates generated during the ozonolysis of limonene, and numerous isomerization pathways for alkoxy radicals resulting from the decomposition of unstable carbonyl oxides. The isomerization reactions yield numerous products with a progressively increasing number of alcohol and carbonyl groups, whereas C-C bond scission reactions in alkoxy radicals shorten the carbon chain. Together these reactions yield a large number of isomeric products with broadly distributed masses. A qualitative agreement is found between the number and degree of oxidation of the predicted and measured reaction products in the monomer range. Additionally, a mechanism that accounts for the formic acid released by photolysis, as described in Chapter 4, is presented.

Reaction mechanisms and discussion

In the following discussion, we assume that the first step in the oxidation of the limonene molecule involves an attack on its endocyclic double bond by ozone (Figure 5.1). The rate constant for the reaction of ozone with the exocyclic double bond is estimated to be an order of magnitude smaller than for the endocyclic double bond.^{61,75} Thus the exocyclic double bonds are expected to be less reactive, and they are likely to react only when most of the endo-bonds are consumed. Furthermore, a significant fraction of the exocyclic bond oxidation reactions is expected after the first-generation products condense in the aerosol phase, and not in the gas-phase.⁷⁵ Note that this assumption is not entirely accurate as products corresponding to the initial ozone attack on the exocyclic double bond in limonene have also been observed (e.g., keto-limonene).^{61,63} However, the order in which the double bonds are oxidized will not affect the overall conclusions of this analysis.

The ozone attack on the endocyclic double bond generates an unstable primary endo-ozonide (POZ) that quickly decomposes into one of two possible endo-carbonyl oxides (Criegee I & II in Figure 5.1). These carbonyl oxides possess a considerable amount of internal energy that is disposed of by isomerization, decomposition, or recombination, leading to a host of known products of the ozonolysis of limonene. Figure 5.1 shows pathways to previously identified products of the ozonolysis of limonene including limononic acid, limononaldehyde, 7-OH-limononaldehyde, and the endo-ozonide.

We believe the critical step responsible for the large number of observed oxidation products is the decomposition of the carbonyl oxide into an OH radical and

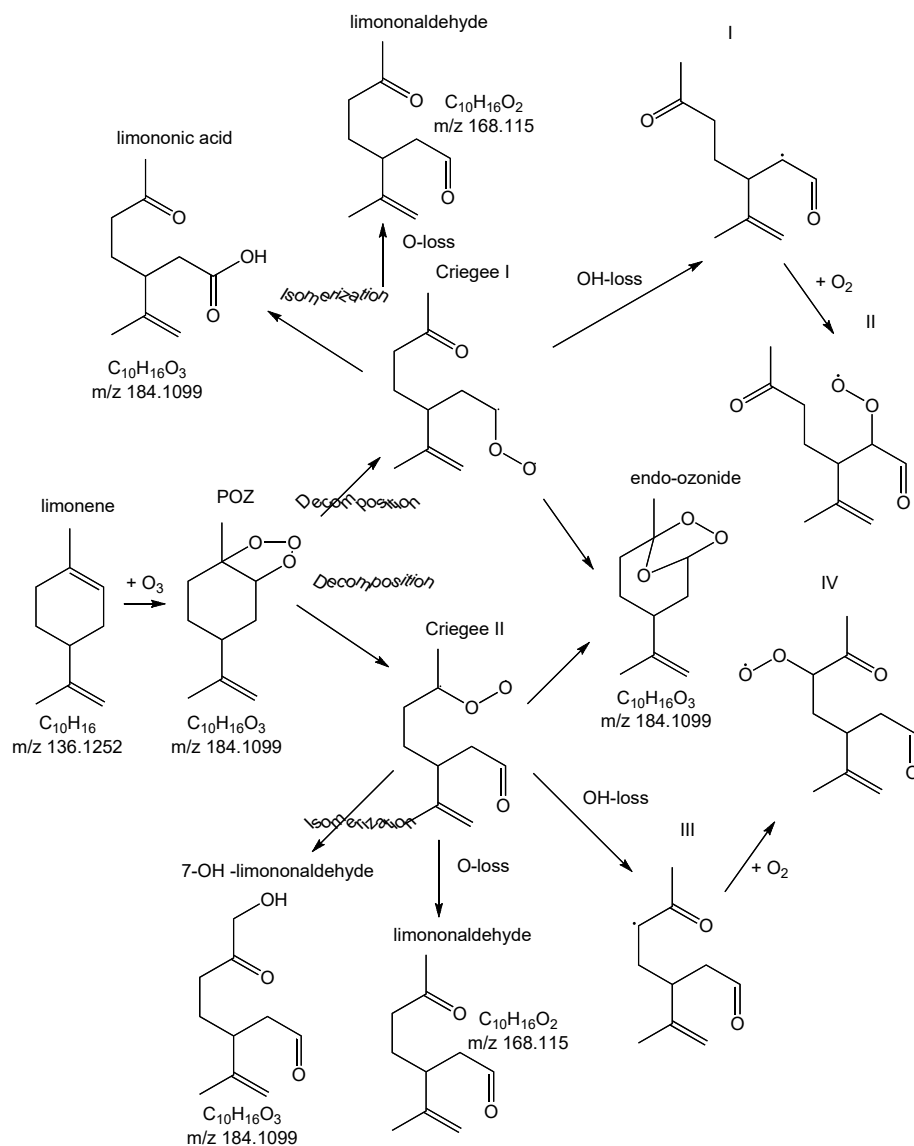


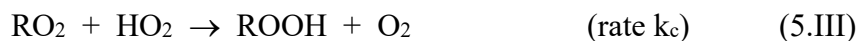
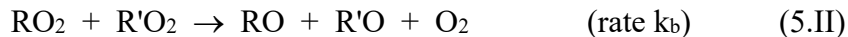
Figure 5.1: Initial products of limonene ozonolysis. The above mechanism outlines primary product formation from the oxidation of the endo-double bond. Radical species are labeled with roman numerals, and stable products have names, formulas, and m/z values next to the structures. The initial process proceeds via the Criegee mechanism, and is followed by subsequent reactions involving the highly reactive Criegee intermediate (CI).

an alkyl radical R (e.g. Criegee I decomposition into alkyl radical I in Figure 5.1).

Loss of OH from carbonyl oxides can be a very efficient process with the branching ratio for this channel approaching unity in certain cases.¹¹⁹⁻¹²¹ The alkyl radical

immediately reacts with an oxygen molecule to become an alkylperoxy radical, RO₂ (e.g., I + O₂ → II).⁸ The OH generated in this reaction goes on to add to double bonds or abstract hydrogen atoms from limonene and its numerous oxidation products, generating additional RO₂ radicals.

Under the NO_x free conditions of this experiment, the primary loss processes for RO₂ radicals are reactions with other R'O₂ radicals that proceed by several competing pathways (Figure 5.2):



The first pathway is a termination step that eliminates two free radicals and generates two stable products. The second pathway is a propagation step that converts alkylperoxy radicals into much more reactive alkoxy radicals. The relative importance of the first two pathways are comparable, with $k_b/(k_a+k_b)$ values generally falling in range of 0.4-0.7⁸ which means that highly reactive alkoxy radicals (RO; e.g. V) can be produced with substantial yields. The formation of organic peroxides only occurs in reactions of RO₂ with HO₂ (5.III); it is negligible in RO₂ self-reactions

From this point, the RO radicals have three possible fates.^{8,122} The most likely process is isomerization involving a facile intramolecular abstraction of a hydrogen atom from the γ -carbon atom (if one is available). Figure 5.2 shows that isomerization of RO radical (V) immediately followed by addition of an oxygen molecule produces another RO₂ radical (VI) that now carries an alcohol group. Repeated RO₂ self-reactions (5.1 & 5.II) followed by RO isomerizations incorporate

multiple oxygen atoms in the resulting products and may be responsible for the appearance of families of $C_xH_yO_m$ with values of m as high as 7 observed using high-resolution mass spectrometry (Chapter 3).

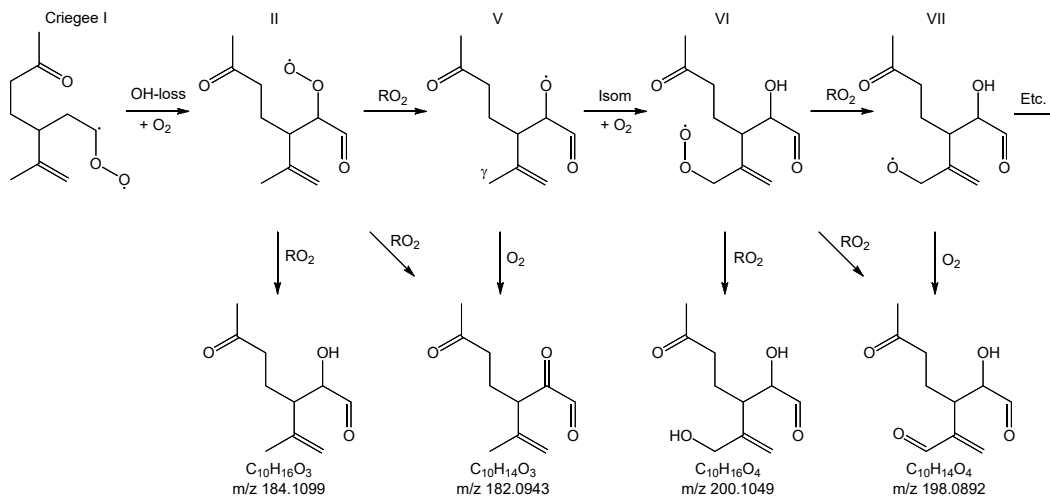


Figure 5.2: Radical isomerization mechanism. The RO isomerization pathway results in species with a progressively increasing number of alcohol and carbonyl groups in the final oxidation products. Radical species are labeled with roman numerals, and stable products have formulas and m/z values next to the structures.

Another possible fate for RO radicals is reaction with an oxygen molecule leading to formation of a stable carbonyl and HO_2 radical. Finally, the RO radical (V) can decompose (Figure 5.3) by scission of the bond between the alkoxy and α -carbon atoms, a process that generates a stable aldehyde and an alkyl radical (VIII) that has fewer carbon atoms than the RO radical from which it originated. The alkyl radical will immediately add an oxygen molecule to form another RO_2 (IX). Repeated RO_2 self-reactions and bond scissions in the resulting RO radicals will lead to progressively smaller products. A combination of all these processes can

potentially result in a very large number of final products, each containing one or more -OH, -CHO, -C(O)-, and/or -COOH functional groups.

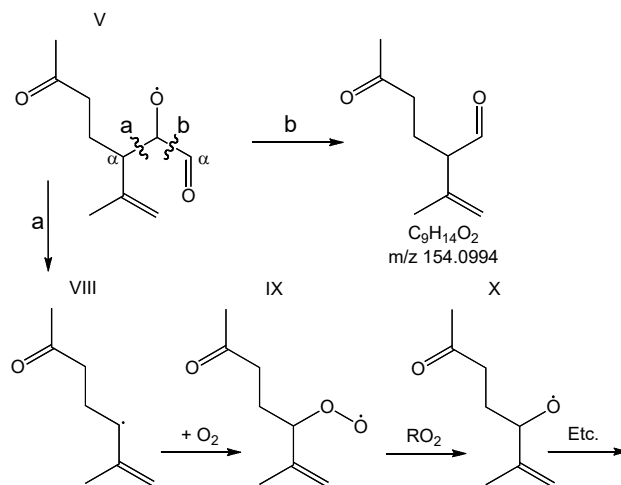


Figure 5.3: Radical decomposition mechanism. The RO radical decomposition pathway consists of bond scission between the alkoxy and α -carbons in RO radicals, resulting in new RO radicals with fewer carbon atoms than in the parent RO radical.

A reaction diagram including the reactions described above is available as supplemental information to Walser et al.⁷⁰ For simplicity, only reactions resulting from the initial decomposition of Criegee intermediates I and II (Figure 5.1) are included. Secondary reactions initiated by the OH by-product of Criegee intermediate decomposition are neglected. This is justified by the lack of difference in the mass spectra of limonene SOA generated in the presence or absence of an OH-scavenger (2-butanol; see Chapter 3). The mechanism is certainly not comprehensive, but it illustrates how the vast number of reaction products can be produced with well-known reactions of RO and RO₂ radicals. Indeed, nearly 60

stable products can be identified in the diagram. Many are structural isomers of each other, with an average of 2-3 isomers per predicted elemental composition.

Most of the stable species formed in the reactions described above still contain the intact exo-double bond. Second generation products will result from ozonolysis of these exo-double bonds. Classical Criegee oxidation of this bond produces a ketone, which replaces the terminal =CH₂ group with oxygen, thus increasing the mass of the original species by 1.9792 amu (Figure 5.4a). Reaction b) in Figure 5.4 shows the loss of CO₂ from the exo-Criegee intermediate, which is equivalent to the loss of C₂H₂ (26.0157 amu) from the original species. As discussed for the primary product, the Criegee intermediate can also decompose to form an alkyl radical (R), followed by the immediate addition of an oxygen molecule to form an alkylperoxy radical (RO₂). The net result in this case is a radical with fewer carbons than the original species, and a mass that is lower by a variable amount, which depends on the size of the fragment, R₂ (Figure 5.4c).

In addition to oxidation of the exo-double bond, aldehydes formed in the initial processes (e.g., limononaldehyde) can be partly oxidized to a carboxylic acid (Figure 5.4d). Although oxidation of aldehydes by ozone is relatively slow,¹²³ even the small amount of carboxylic acids produced will result in a sizeable signal in the mass spectra presented in Chapter 3, because of the exceptionally high ionization efficiency of carboxylic acids. This oxidation (-CHO → -COOH) increases the mass of the original aldehyde by 15.9949 amu. Finally, Figure 5.4e shows examples of various dimerization processes that can occur, resulting in the formation of exo-

ozonides that slowly decompose, or alkylperoxides, which decompose to form smaller molecules.

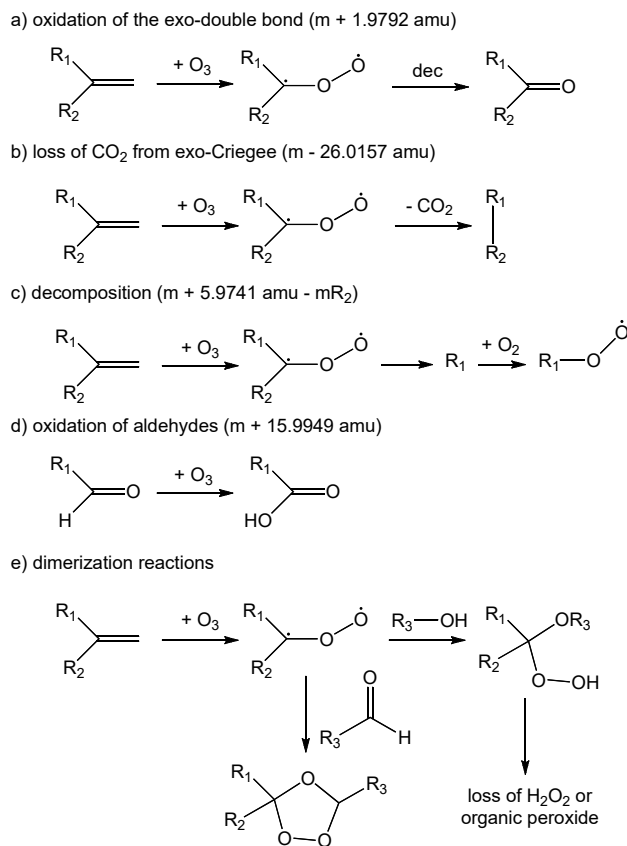


Figure 5.4: Formation of secondary products. Secondary product formation results from the oxidation of the exo-double bond (a-c) as well as oxidation of double bonds and aldehydes in primary products (d). Additionally, processes such as dimerization (e), lead to increased species complexity in the SOA.

The second-generation processes shown in Figure 5.4 greatly increase the number of additional products compared to the number of first-generation products from the oxidation of the endo-double bond. Processes a-d alone nearly quadruple the number of possible products to well over 200. Many of these products are isomers with an identical elemental composition but different structures. Accounting

for structural isomerism, we still predict some 50 plus distinct masses in the monomeric region. This prediction is qualitatively consistent with the large number of peaks observed in the mass spectra below 300 amu shown in Chapter 3.

It is likely that organic peroxides formed during oxidation of limonene are responsible for a large portion of the photochemistry of the resulting SOA particles. Figure 5.5 shows an abbreviated mechanism of the initial oxidation reaction, with emphasis placed on the formation of organic peroxides.

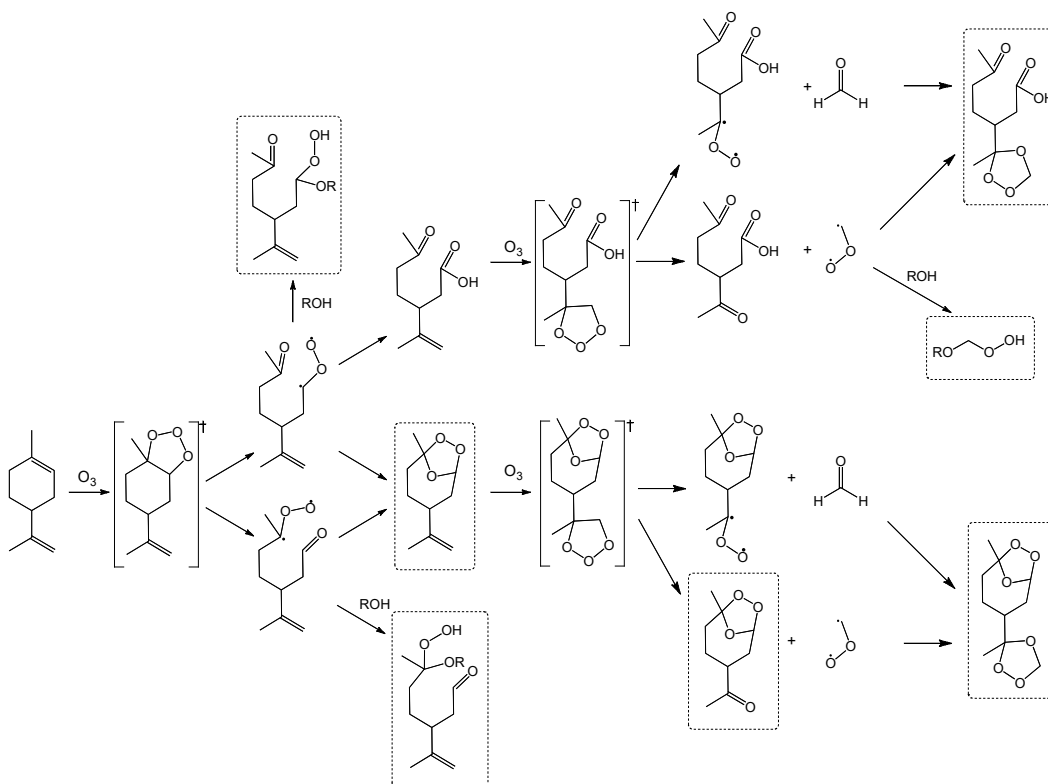


Figure 5.5: Organic peroxide formation during ozonolysis of limonene. Crosses (†) indicate short-lived primary ozonides and dashed boxes indicate comparatively stable organic peroxides that are susceptible to photolysis in the actinic region.

As discussed above, the initial cyclo-addition of ozone to the endocyclic double bond results in a highly reactive primary ozonide (POZ) that can rearrange

into a secondary ozonide (SOZ) or decompose into a molecule with carboxyl and carbonyl functionalities. These reactions go through the reactive Criegee intermediate, which can either decompose or react with carboxylic acids, alcohols, and water to form organic peroxides.

Because ozonolysis of the exocyclic double bond is more likely to occur after the first generation products condense into initial SOA,⁷⁵ the mechanism is slightly different than that for the exo-double bond. The primary difference is that POZ splitting now results in two separate molecules rather than one bifunctional molecule. The other significant difference is that thermal decomposition and isomerization of carbonyl oxides are significantly suppressed in the aerosol particle phase, whereas their reactions with the first-generation products are enhanced. Therefore, the yield of exo-cyclic SOZ and oligomeric peroxides may actually be higher than that derived from the endocyclic double bond.

The formic acid observed upon photolysis of limonene SOA (see Chapter 4) is most likely produced from the secondary ozonide (1,3,4-trioxalane) formed from the ozonolysis of the exocyclic double bond. As discussed in Chapter 4, the photolysis mechanism (Figure 5.6) is similar to that of other systems involving SOZ species.^{111,112,117,118} It involves breaking the weakest O-O bond in the ozonide, followed by an H-atom transfer and subsequent decomposition. It is not clear what functional group serves as a precursor to formaldehyde, which was also observed upon photolysis of limonene SOA. It is possible that it results from secondary reactions of OH produced by photolysis of hydroxyhydroperoxides.

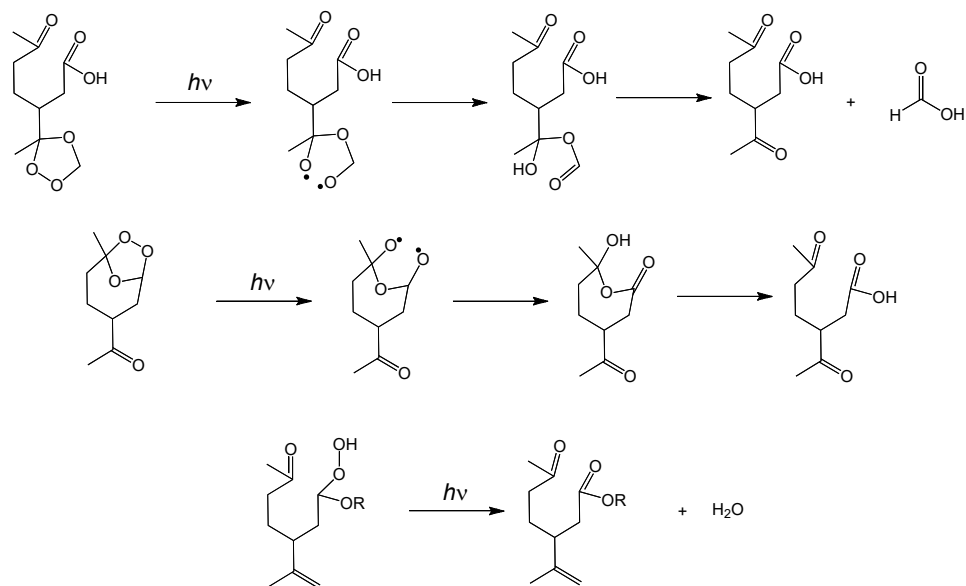


Figure 5.6: Photolysis reactions of organic peroxide species. Examples of photolysis reactions of peroxides, including the formation of formic acid observed using IR-CRDS (Chapter 4). Formation of larger organics is currently under investigation.¹¹³

Conclusion

The reaction mechanisms presented here support the results of the high-resolution mass spectrometry and IR cavity ringdown spectroscopy studies presented in Chapters 3 and 4, respectively. The large number of products observed in both the monomer and oligomer regions of the mass spectra can be explained by known ozone chemistry and subsequent isomerization, addition and decomposition reactions. As seen in Figure 3.4, there is a reasonable agreement between the masses, mass defects, and atomic ratios predicted by our mechanism, and those observed via mass spectrometry. The production of formic acid upon photolysis of limonene SOA is likely due to the presence of organic peroxides, which can also be explained by known ozone chemistry.

APPENDIX I

SOLVENT EFFECTS

The study of limonene-derived secondary organic aerosol (SOA) via high-resolution mass spectrometry revealed several solvent-dependent differences. Figure I.1 shows representative stick spectra of limonene SOA collected in the a) positive and b) negative ESI modes in four different solvents: acetonitrile, dichloromethane, methanol, and water. All data shown here are for peaks with >0.5% abundance relative to the largest peak in their respective spectra.

Mass spectra for SOA extracts in methanol looked qualitatively similar to the spectra of acetonitrile extracts, and the ion intensities were comparable in magnitude. However, the exact peak positions were not identical, with clear evidence of methylation (addition of CH₃OH) of a large fraction of SOA peaks in the methanol mass-spectra. Indeed, for 51% and 45% of peaks below 300 amu in the positive and negative ion modes, respectively, there was a coincidence between peaks in acetonitrile mass spectra and peaks in the methanol mass spectra shifted down by 32.0262 amu, the molecular weight of a methanol molecule. The methylation was observed in both positive and negative ion modes suggesting that it occurred during the SOA extraction, and not during the electrospray process. Figure I.2 shows data for the monomer region of the spectrum ($m/z < 300$ amu). By comparing peaks in this expanded region, the differences between the four solvents tested become more easily visible. Additionally, Table I.1 lists the m/z and elemental composition of the 5 most abundant peaks observed in both the positive and negative ion modes from SOA

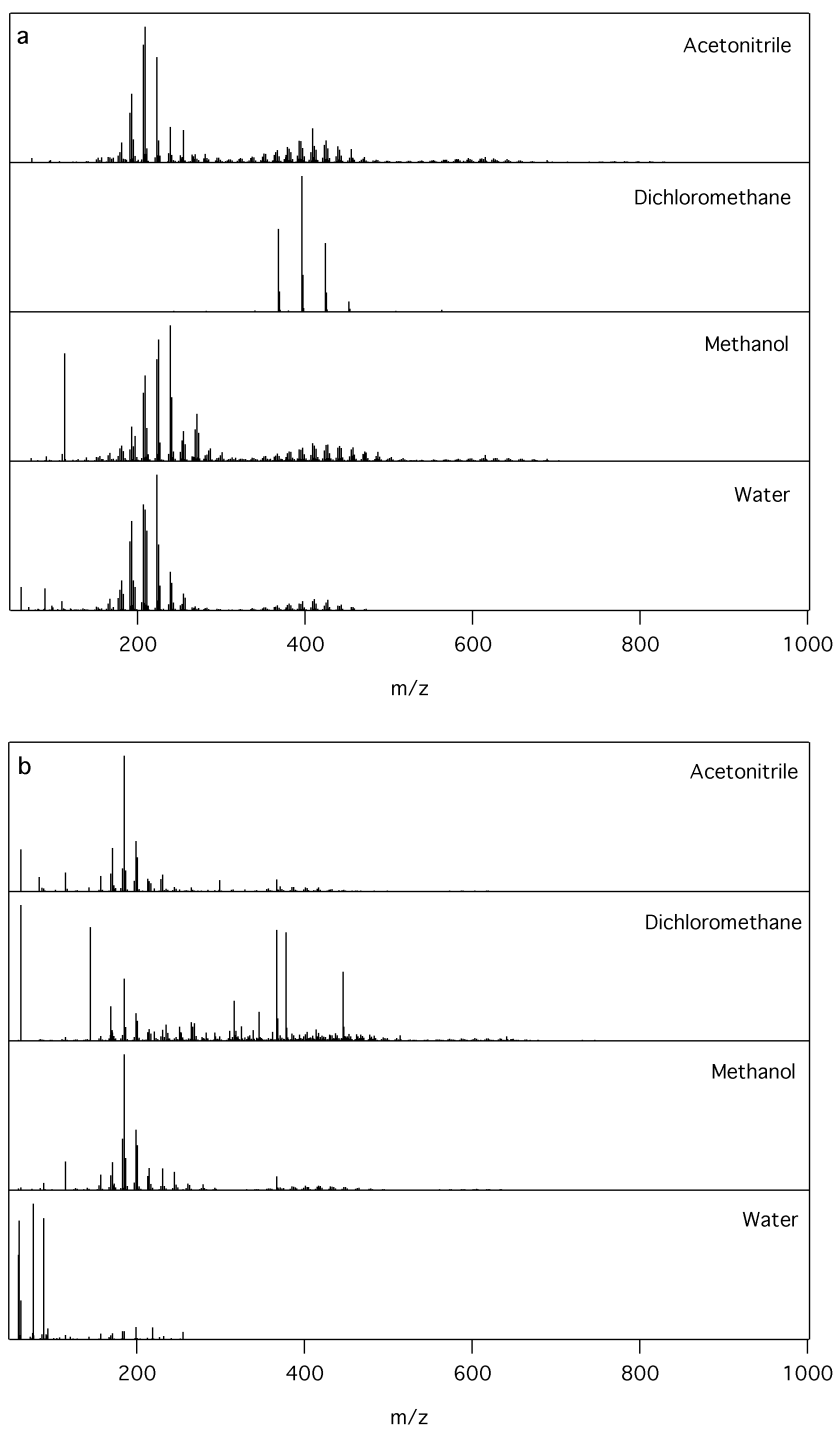


Figure I.1: Mass spectra of SOA extracted in 4 solvents. The same limonene-derived SOA sample was divided into four, roughly equal, portions and extracted in equal volumes of acetonitrile, dichloromethane, methanol or water. The resulting extracts were examined via high-resolution mass spectrometry in both the a) positive and b) negative ESI modes. This figure spans the entire m/z range for which data were collected (50-1000 amu).

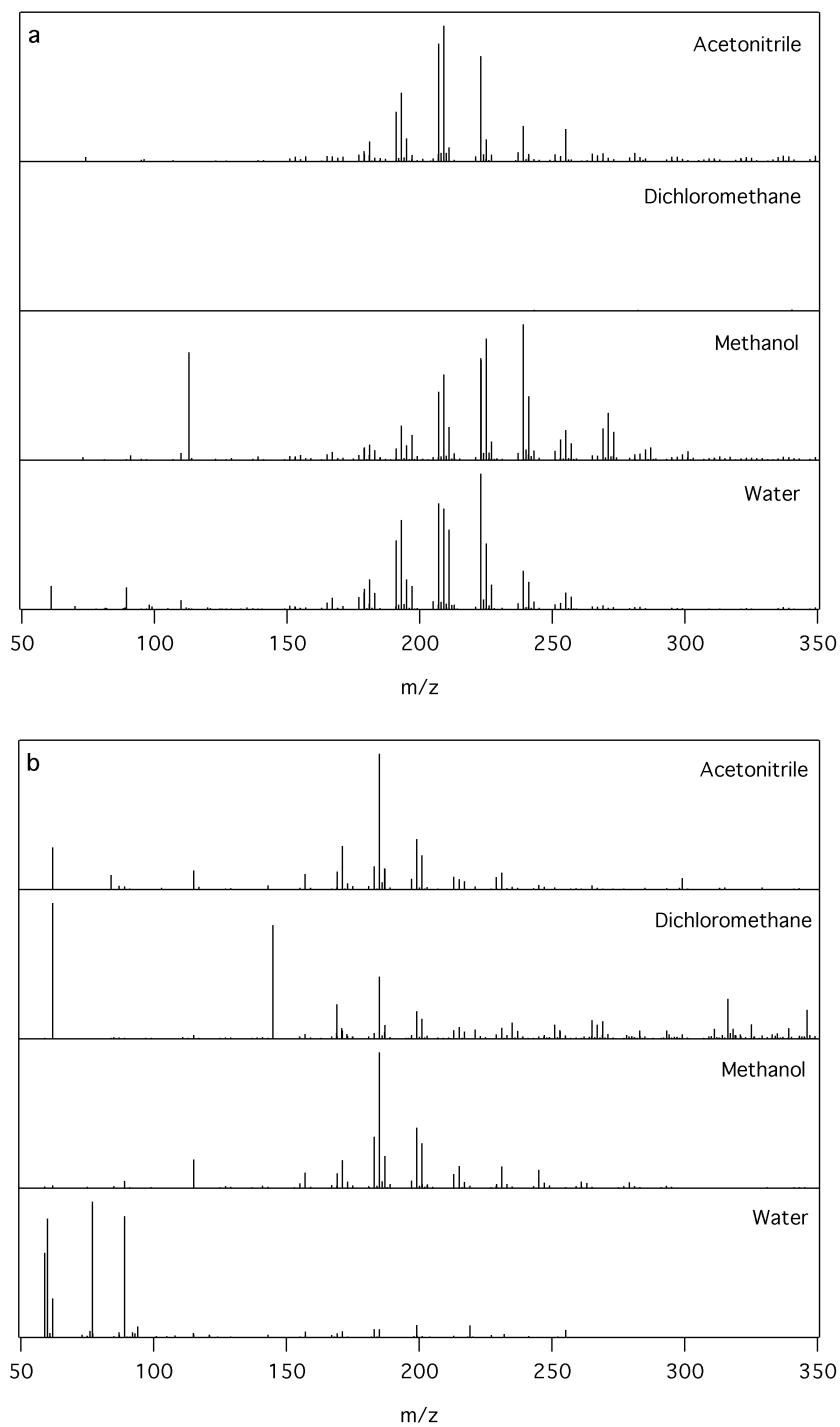


Figure I.2: Monomer region of mass spectra of SOA extracted in 4 solvents. The same limonene-derived SOA sample was divided into four, roughly equal, portions and extracted in equal volumes of acetonitrile, dichloromethane, methanol or water. The resulting extracts were examined via high-resolution mass spectrometry in both the a) positive and b) negative ESI modes. This figure highlights the monomer region ($m/z < 300$ amu) of the mass spectra.

extracted in methanol and acetonitrile. The data in this table shows that while methylation of SOA components did occur, it did not occur in every case, making data obtained in methanol even more difficult to interpret.

Table 1.1: Five most abundant peaks (m/z , relative abundance, elemental composition) observed in the positive and negative ESI modes from SOA extracted in CH_3CN and CH_3OH .^a

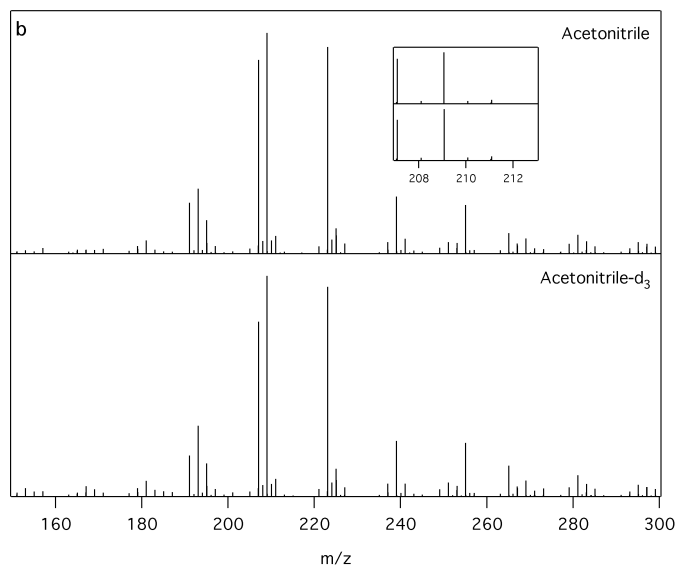
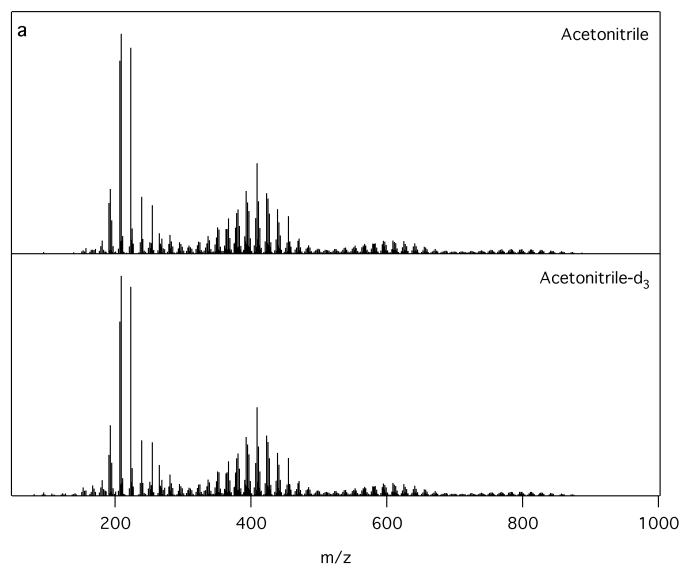
Acetonitrile					
Positive Ion Mode			Negative Ion Mode		
209.0777	100%	$[\text{NaC}_9\text{H}_{14}\text{O}_4]^+$	185.0817	100%	$[\text{C}_9\text{H}_{13}\text{O}_4]^-$
207.0984	87	$[\text{NaC}_{10}\text{H}_{16}\text{O}_3]^+$	199.0974	37	$[\text{C}_9\text{H}_{15}\text{O}_4]^-$
223.0933	78	$[\text{NaC}_{10}\text{H}_{16}\text{O}_4]^+$	171.0661	32	$[\text{C}_8\text{H}_{11}\text{O}_4]^-$
193.0827	51	$[\text{NaC}_9\text{H}_{14}\text{O}_3]^+$	201.0766	25	$[\text{C}_9\text{H}_{13}\text{O}_5]^-$
191.1035	37	$[\text{NaC}_{10}\text{H}_{16}\text{O}_2]^+$	183.1024	17	$[\text{C}_{10}\text{H}_{15}\text{O}_3]^-$
Methanol					
Positive Ion Mode			Negative Ion Mode		
239.1247	100%	<i>$[\text{NaC}_{11}\text{H}_{20}\text{O}_4]^+$</i>	185.0812	100	$[\text{C}_9\text{H}_{13}\text{O}_4]^-$
225.1091	90	<i>$[\text{NaC}_{10}\text{H}_{18}\text{O}_4]^+$</i>	199.0968	45	$[\text{C}_{10}\text{H}_{15}\text{O}_4]^-$
223.0935	75	$[\text{NaC}_{10}\text{H}_{16}\text{O}_4]^+$	183.1019	38	$[\text{C}_{10}\text{H}_{15}\text{O}_3]^-$
209.0778	63	$[\text{NaC}_9\text{H}_{14}\text{O}_4]^+$	201.0761	33	<i>$[\text{C}_9\text{H}_{13}\text{O}_5]^-$</i>
207.0985	50	$[\text{NaC}_{10}\text{H}_{16}\text{O}_3]^+$	187.0604	24	$[\text{C}_8\text{H}_{11}\text{O}_5]^-$

^adata in italics represent peaks in methanol spectra that are likely methylated SOA components (i.e. $m/z - 32.0262$ amu is observed in the corresponding acetonitrile spectrum).

Negative ion mode mass spectra obtained from dichloromethane SOA extracts were similar in the overall appearance but considerably weaker in intensity suggesting that the majority of the observed peaks correspond to moderately polar species. In the positive ion mode, there were very few peaks in the dichloromethane sample that were above 0.5% relative abundance, with virtually no peaks in the monomer region of the spectrum. In addition, there were impurity peaks in both modes resulting from reaction between dichloromethane and ion source components.

SOA samples extracted in water were comparable in both appearance and intensities to acetonitrile spectra obtained in the positive ion mode. Water extracts in the negative ion mode were considerably weaker in intensity. Because of issues with

solvent-analyte adduct formation, interaction with ion source components, and weak intensities, methanol, dichloromethane, and water, respectively, were all abandoned as extraction solvents after a few initial trials. A more complete investigation of the effects of solvent choice on SOA analysis via high-resolution mass spectrometry is currently underway, and will be presented in more detail in a future publication.



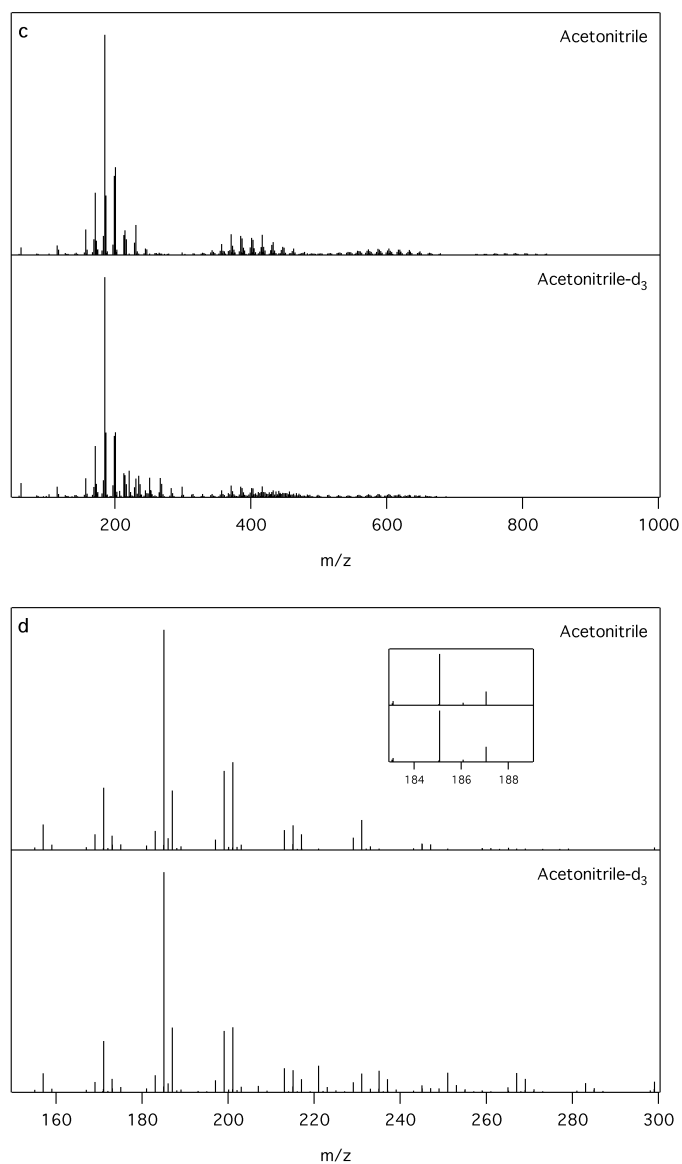
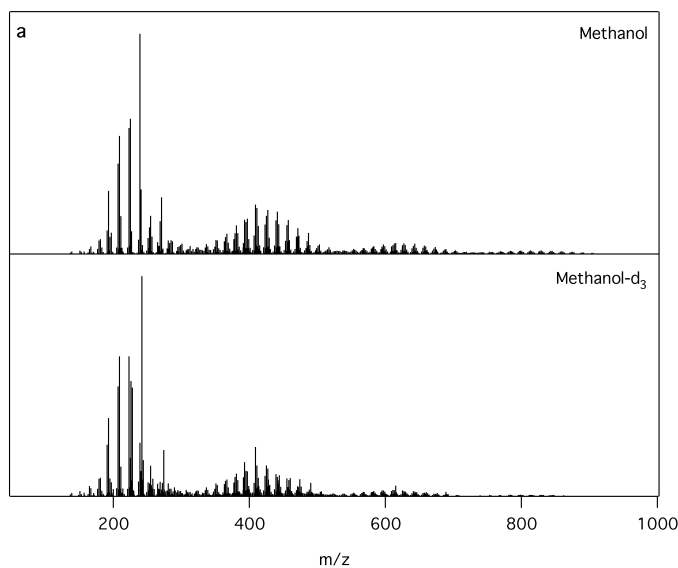


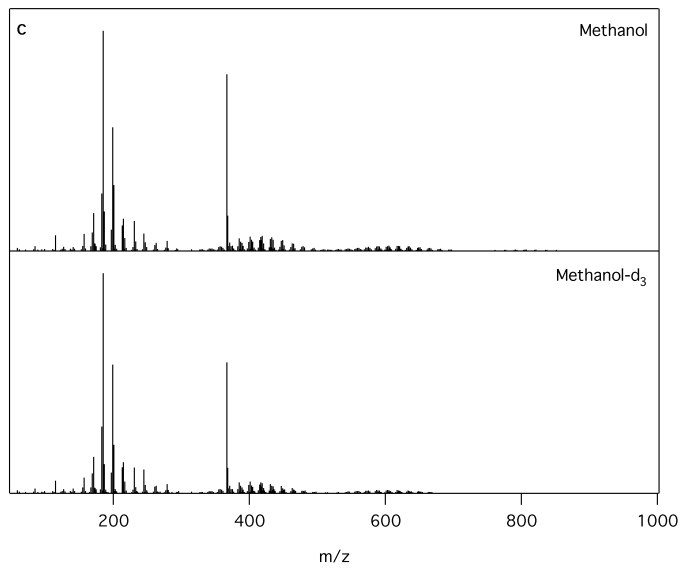
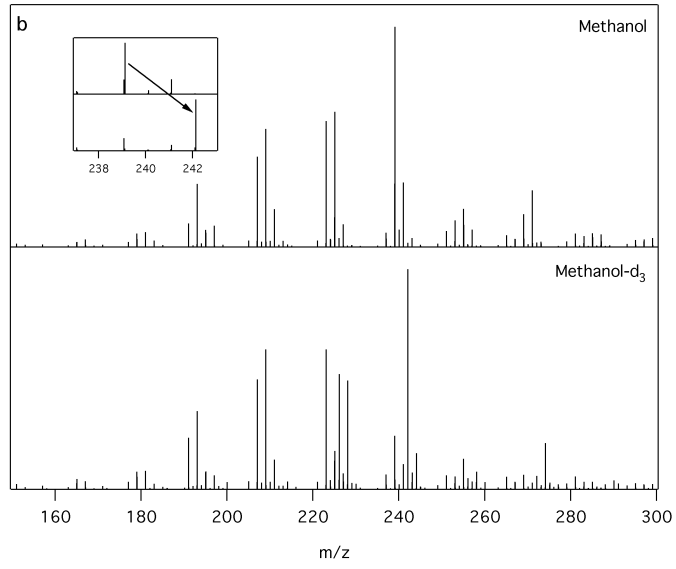
Figure I.3: Mass spectra of SOA extracted in isotopically labeled CH_3CN . The same limonene-derived SOA sample was divided into two, roughly equal, portions and extracted in equal volumes of acetonitrile (CH_3CN) or acetonitrile- d_3 (CD_3CN). The resulting extracts were examined via high-resolution mass spectrometry in both the a-b) positive and c-d) negative ESI modes. The spectra in a) and c) span the entire m/z range for which data were collected (50-1000 amu), while the spectra in b) and d) highlight the monomer region ($m/z < 300$ amu).

Additional evidence of solvent reactions was obtained using isotopically labeled solvents. There was no observable difference between positive ion mode

spectra obtained from samples extracted in acetonitrile (CH_3CN) and acetonitrile- d_3 (CD_3CN ; Figure I.3). Negative ion mode spectra had very few, likely insignificant, differences, i.e., smaller relative abundances of peaks in the oligomer region of the spectrum ($m/z > 300$ amu). Both the full spectra and the monomer region are shown in Figure I.3, which illustrates that the mass spectrum obtained in isotopically labeled acetonitrile is virtually the same as the mass spectrum obtained in acetonitrile.

SOA samples were also extracted in both methanol (CH_3OH) and methanol- d_3 (CD_3OH ; Figure I.4). A comparison of the major peaks in both the positive and negative ion modes showed a shift of 3.0188 amu, which corresponds with replacing 3 hydrogen atoms with 3 deuterium atoms. Mass spectra of SOA samples extracted in methanol- d_4 (CD_3OD ; data not shown) were also obtained. However, because of proton exchange between the methanol and acidic SOA components in addition to methylation, it was difficult to extract useful information from the data.





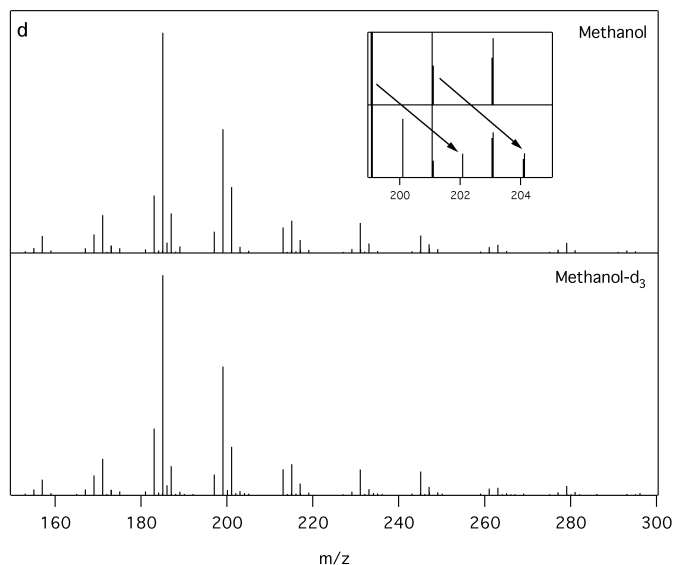


Figure I.4: Mass spectra of SOA extracted in isotopically labeled CH₃OH. The same limonene-derived SOA sample was divided into two, roughly equal, portions and extracted in equal volumes of methanol (CH₃OH) or methanol-d₃ (CD₃OH). The resulting extracts were examined via high-resolution mass spectrometry in both the a-b) positive and c-d) negative ESI modes. The spectra in a) and c) span the entire *m/z* range for which data were collected (50-1000 amu), while the spectra in b) and d) highlight the monomer region (*m/z* < 300 amu).

To check for addition of the labeled solvents to SOA components, the peaks with even *m/z* values were examined (Table I.2). For the system examined, species containing only ¹²C, ¹H, and ¹⁶O should have odd masses in their ionized form. Incorporation of ¹³C would lead to an observed *m/z* with an even value.

Table I.2: Five most abundant peaks with even *m/z* observed in the positive and negative ESI modes from SOA extracted in isotopically labeled CH₃OH.^a

Positive Ion Mode			Negative Ion Mode		
Methanol-d ₃	<i>m/z</i> - 3D	Methanol	Methanol-d ₃	<i>m/z</i> - 3D	Methanol
<i>242.1435</i>	<i>239.1247</i>	<i>239.1252</i>	186.0845	183.0657	183.0653
226.1486	223.1298	223.1302	200.1001	197.0813	197.0808
<i>228.1278</i>	<i>225.1090</i>	<i>225.1095</i>	184.1054	181.0866	181.0860
274.1331	271.1143	271.1149	204.1311	201.1123	201.1119
<i>244.1227</i>	<i>241.1039</i>	<i>241.1044</i>	202.0793	199.0605	199.0601

^adata in italics represent peaks in methanol spectra were one of the five most abundant peaks.

In addition, replacing three ^1H atoms with three ^2H atoms would increase the m/z by 3.0188 amu, yielding an even m/z . For data obtained from SOA extracted in acetonitrile- d_3 , all peaks with even values of m/z were due to incorporation of ^{13}C (peak assignments were examined for self-consistency, as discussed in Chapter 3). For methanol- d_3 spectra, there were peaks with even values of m/z that could not be explained by ^{13}C incorporation, and had a corresponding peak at $m/z - 3.0188$ amu in the analogous methanol spectrum.

APPENDIX II

TRACE GAS MEASUREMENTS

*Reproduced in part with permission from Global Biogeochem. Cycles, 2006, 20, GB3015 and Geophys. Res. Lett., 2007, 34, L01806
Copyright © 2006 and 2007 American Geophysical Union*

Methyl halides in the atmosphere

Methyl chloride (CH_3Cl), methyl bromide (CH_3Br), and methyl iodide (CH_3I) are chemically important atmospheric constituents. Accurate knowledge of CH_3Br and CH_3Cl sources is particularly needed because their relatively long residence times allow them to reach the lower stratosphere where halogen radicals produced from their photodissociation and OH attack catalytically destroy ozone. In fact, CH_3Cl and CH_3Br are responsible for ~27% of halogen-catalyzed ozone destruction.¹²⁴ Despite its short residence time, CH_3I can contribute to stratospheric ozone destruction,¹²⁵ strongly affect tropospheric chemistry, especially in the marine boundary layer, and indirectly promote marine aerosol and cloud condensation nuclei formation.¹²⁶⁻¹²⁸

Methyl halides are significant vectors of halogen transport (especially for bromine and iodine) from the terrestrial and marine environment to the atmosphere. Saiz-Lopez and Plane¹²⁹ describe the tropospheric reaction mechanisms whereby inorganic halogen species (a) destroy ozone, (b) oxidize organic compounds such as dimethyl sulfide, (c) influence the ratios of NO_2/NO and HO_2/HO , and (d) by which inorganic bromine removes elemental mercury and (e) how iodine can cause fine particle formation. Detailed reaction schemes are also presented by von Glasow et al.¹³⁰ and references therein.

The magnitude of known atmospheric methyl halide removal mechanisms is much greater than known methyl halide sources (Table II.1).^{131,132} Although the marine environment (oceanic and coastal zones) have long been recognized as important natural producers of methyl halides, terrestrial ecosystems may be equally, if not more, important sources of methyl halides, especially CH₃Cl and CH₃Br.

Table II.1: Atmospheric methyl halide budgets

	Mixing ratio (ppt) ^a	Atmospheric burden (Gg) ^a	Atmospheric lifetime ^a	Total known sources (Gg/yr)	Total known sinks (Gg/yr)
CH ₃ Cl	575 (Marine: 500-620) (Terrest: 550-1400)	5300	~1.5 years	3500-4500 ^c	4500-5500
CH ₃ Br	9 (7-20)	150	~8 months	125 ^b	100-450
CH ₃ I	2 (0.2-43)	55	~ 4 days	~250-1500 ^b	1000-2000

^aHarper and Hamilton¹²⁴

^bOrlando¹²²

^cButler¹³³

Terrestrial methyl halide sources

Methyl halides are naturally produced by photoautotrophs and certain fungi. The major mechanism of biosynthesis is enzymatic,¹³⁴ although an additional abiotic mechanism in leaf litter has been proposed.¹³⁵ The relative environmental importance of higher plant methyl halide emissions, especially from marshes,¹³⁶⁻¹³⁸ agriculture,¹³⁹ and tropical plants¹⁴⁰ has only recently been appreciated. Vegetation from temperate coastal salt marsh plants was estimated to produce 10% of the global source strength for the two gases CH₃Cl and CH₃Br.¹³⁷

In addition to coastal salt marshes, this work also attempts to quantify methyl halide emissions from greenhouse-grown mangroves. Highly productive mangrove forests, or mangals, are situated in sandy and muddy tropical and subtropical

sheltered coastal locales.¹⁴¹ Although more structurally complex, mangals are the tropical equivalent of the temperate coastal salt marsh ecosystem. Mangroves are halophytic trees and woody shrubs that are exposed directly or indirectly to seawater halides. Their global range is approximated by the 20 °C winter ocean isotherm, and as such cover approximately 60-70% of the coastline between 25 °N and 25 °S latitudes.¹⁴¹ Of the 50-75 recognized mangrove species, comprising 16-20 families, there are 4 major genera: *Rhizophora*, *Avicennia*, *Bruguiera* and *Sonneratia*.¹⁴¹⁻¹⁴³ We obtained young red (*Rhizophora mangle*) and black (*Avicennia germinans*) mangrove saplings and grew them in a greenhouse, mimicking certain features of their tropical habitats such as exposure to high temperature, seawater, and water-logged anoxic soil.

Experimental

Location, plant species, and incubation conditions

Coastal salt marsh. The location for this study was Upper Newport Bay, California, near the old salt dike (33°38.75 N, 117°52.94 W; Figure II.1). Four halophytic species *Spartina foliosa* (Cordgrass), *Salicornia virginica* (Pickleweed), *Batis maritima* (Saltwort) and *Frankenia grandifolia* (Alkali Heath) were chosen based on their known ability to produce methyl halides¹³⁷ and their dominance in southern California coastal salt marshes.

Methyl halide emissive flux was determined by enclosing a single plant species in an incubation chamber and periodically withdrawing a gas sample into a valved, pre-evacuated canister or lockable syringe. The bottom was sealed by the

surrounding mud and soil (> 0.5 cm deep). Different sized chambers were used to accommodate the different sized plants. The smallest was a 4 L modified glass beaker (14 cm ID) with sampling port, thermometer port, and an internal battery-powered fan. The sampling port contained a 20 cm stainless steel tube (1/16 in. OD; 0.1 mL dead volume) that extended into the center of the chamber. The portion extending outside the chamber had a glass sleeve with septum for withdrawing a 30-mL gas sample into a syringe.

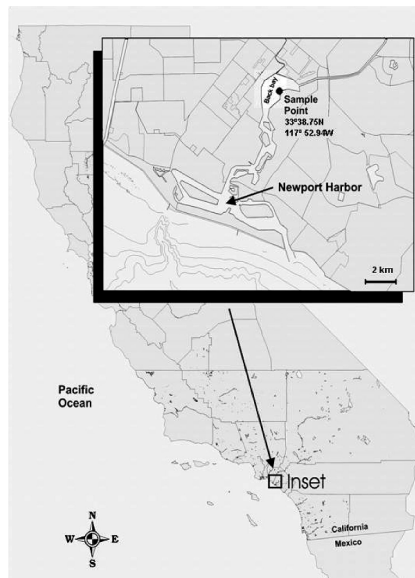


Figure II.1: Map of sampling location. The sample site was located in Newport Back Bay, California (33°38.75 N, 117°52.94 W).

Larger chambers were made of stackable sections of polycarbonate tubes (29.5 cm ID, 30 cm height) with polyethylene connectors, mounted on permanent polyvinyl chloride chamber bases (15 cm height) to yield sealed chamber volumes of 24-90 L.¹³⁹ These large chambers had a sealed lid containing two ports, one for sampling and the other for a thermometer. The sampling line was a 30 cm stainless

steel tube (1/4 in. OD; < 5 mL dead volume) that extended into the center of the chamber with a compression fitting for sampling with the attachment of a 500-mL stainless steel canister. These chambers did not inherently emit or absorb significant amounts of methyl halides.¹³⁹

Control incubations were performed similarly by positioning the same type of chamber over unvegetated areas close to, and at the same elevation as, the respective plant chamber, avoiding all aerial plant material. Areas covered with the green algae *Enteromorpha* sp., at times present on marsh mudflats, were avoided as *Spartina* control sites.

Permanent chamber bases were used for *Spartina* and *Salicornia* incubations because bimonthly removal of *Spartina foliosa* was destructive to the habitat and because the woody basal and migrating stems of *Salicornia virginica* made it difficult for the glass chamber to form a seal in the soil without damaging the plants. No biomass was harvested from within the permanent bases after incubations. Control incubations used chambers without permanent bases.

We began our study of *Spartina* by placing the chamber base over new shoots on the immediate edge of a pure stand. After 2 years, at the end of our measurements, the chamber base was well inside the *Spartina* bed, >3 m from the growing edge. Independent of the *Salicornia* incubations using the larger chambers, nine additional incubations of *Salicornia* were performed using the small glass chamber followed by tissue harvesting to determine biomass specific production rates. Small glass chambers were used for all *Batis* and *Frankenia* incubations. After the incubation

period, all aerial *Batis* and *Frankenia* biomass, including woody biomass, was harvested for fresh weight determinations.

All incubations were performed between 0930 and 1400 local time, at a period of low tide. Weather conditions and air temperatures were recorded. Incubation sampling duration and frequency ranged from 5-15 min at 1- to 5-min intervals, depending on the plant species and chamber used.

Greenhouse-grown mangroves. On 18 October 2002 ($t = 0$) 15 cm saplings of *R. mangle* (red mangrove) and *A. germinans* (black mangrove) were obtained from Mangroves Direct (Nova University) and 5 each planted in watertight bin containers (0.91 m \times 0.91 m \times 0.6 m depth) located in the UCI greenhouse. Four trees were located near each corner with the fifth in the center; all equally spaced from one another. The center plant was monitored for methyl halide emissions and growth throughout the study. The marginal plants were placed to minimize possible edge effects that may have occurred between plant roots and the bin. As all of the plants grew, the outer plants began to crowd and grow over the container sides, making their potential chambering unfeasible. Initially, growth of all plants were followed, however, as the marginal plants began to crowd the center plant, they were trimmed to allow unrestricted growth and the continued chambering of the center plant.

The bins were lined with EPDM rubber pond liner (PondGard[®]; Firestone, Akron, OH). Each bin was filled with sifted (1.3 cm screen) soil (~340 kg) from a nearby freshwater marsh, into which solid fertilizer (Scotts Turf Builder[®], Marysville, OH; equivalent to 15 g-N, 1.5 g-P, and 1.5 g-S per bin) had been thoroughly

mixed.¹⁴⁴ A hole (15 cm diameter × 30 cm deep) was dug and the bottom 2/3 of the planted tree roots were surrounded by sand and soil with the upper third surrounded by Aruba Puka Shells (Seaflo[®]; CaribSea, Miami, FL) to 3 cm above the surface. Freshwater of salinity <1‰ (0.001) covered the soil substrate for the first 60 days. The salinity was then increased by 5‰ increments with addition of seawater every month until reaching 15‰ (day 150) after which it was maintained between 10-15‰ for an additional 3 months (day 240). After this 8-month period, the salinity was maintained between 18-28‰.

Supplemental lighting (350 $\mu\text{mole quanta m}^{-2} \text{ s}^{-1}$ at the soil surface, 12L/12D) was supplied to each bin from a separate metal halide lamp (1000 W; Venture Lighting, Racine, WI). Prior to day 334, the greenhouse glass was tinted to reduce the ambient light by 50%, supplemental heating was not available except during the day from the artificial lighting (minimum winter night temperature was 14 °C reached on several days) and cooling kept the summer high temperature of air below 35 °C. After that date the tinting was removed and the greenhouse environment maintained by computer (GEM Link; QCOM, Irvine, CA) at 19-32 °C. Growth was monitored by measuring leaf surface area of the centered individual from which methyl halide emissions were also measured.

Methyl halide flux was determined between 1000 and 1400 local time by enclosing the center plant in an incubation chamber and periodically withdrawing a gas sample into a valved, pre-evacuated canister. Artificial lighting was turned off during incubations to prevent excessive chamber temperatures. The bottom was sealed by the surrounding water (1 to 2 cm deep) and mud.

Four different sized chambers were used to accommodate the growing plant: 9 L glass cylinder (14 cm ID), 40 L and 80 L polycarbonate cylinders (29.5 cm ID), and a 450 L Plexiglas[®] cube. Control incubations were performed similarly by positioning the 9 L glass cylinder or 20 L polycarbonate cylinder over the water/mud avoiding all aerial portions and visible roots of the plant. Incubation temperatures ranged from 24-37 °C. Incubation sampling frequency and duration ranged from 0-15 min at 5-min intervals, to 0-90 min at 30-min intervals, depending on the size of the chamber.

Methyl halide analysis

Analysis was performed as described by Redeker et al.¹³⁹ using gas chromatography (GC-ECD). A known amount (by pressure) of chamber air sample was pre-concentrated in a glass-bead-packed stainless steel loop at 77 K. It was then directly injected onto a 50 m 0.53 µm Poraplot-Q column (Chrompack) and detected by electron-capture (Hewlett Packard 5890 Series II). Standards in N₂ (certified 9.68 ppb CH₃Br and 479 ppb CH₃Cl; 25.4 ppb CH₃I; Scott Specialty Gases) were injected at low pressures to create linear calibration curves with a range of absolute amounts bracketing sample amounts.

Tissue halide extraction and analysis

Halide analysis was intermittently performed on tissue harvested throughout the study periods. The chambered *Batis* and *Frankenia* tissue harvested for biomass determination was so analyzed. *Spartina* and *Salicornia* tissue immediately adjacent

to the permanent chamber base was used for halide analysis. *R. mangle* and *A. germinans* tissue from corner plants was used for analysis.

Tissue samples were weighed, rinsed in deionized water to remove any external salts and dried to constant weight at 55 °C. The dried tissue was weighed, milled into a fine powder (40-mm mesh) and stored in a capped glass vial under desiccation. Solid content of tissue (% dwt) was calculated.

Halides were extracted from the milled plant tissue in the manner of Ralph & Manley¹⁴⁵ by adding the powder (0.5 g) to 50 mL of boiling, deionized water in a 150-mL flask for 10 min. Boiled tissue was then vacuum filtered and the filtrate collected and stored frozen until halide analysis. The extraction procedure was repeated 5 times on the same sample to ensure complete halide removal from the tissue. Greater than 98% Cl⁻, 97% Br⁻, and 99% I⁻ was removed from the tissue after three sequential extractions, and the three-step extraction procedure became the standard method. Values were not corrected for the 1 to 3% loss.

The halide concentration in each extract was determined using a specific ion meter/autotitrator (Thermo Orion) in conjunction with the appropriate halide electrode using Gran's known addition method.^{145,146} This method allowed for the measurement of halides near their limit of detection: 5×10^{-5} M Cl⁻; 5×10^{-6} M Br⁻; and 5×10^{-8} M I⁻ (Thermo Orion specifications) and minimized the interfering effects of other ions and compounds. Following the autotitration, the calculated initial concentration reported in mM was converted to tissue halide content as percent dry weight. The mean standard check for accuracy (with precision as % S.D.) of the analysis was 98% for Cl⁻ (5.7%), 88% for Br⁻ (11%) and 95% for I⁻ (8.0%).¹⁴⁵

Results and discussion

Coastal salt marsh

All emission rates reported are net rates (plant chamber minus control) unless otherwise indicated. The two-point averaged net emission rates normalized to the marsh area enclosed by the chamber, from sampling twice a month are shown in Figure II.2 for *S. foliosa*, *S. virginica*, *F. grandifolia*, and *B. maritima*. The average ambient monthly temperature at Newport Harbor was obtained from NCDC-NOAA (Climate-Radar Data Inventories, 2005). The insolation was taken from data from the San Joaquin Freshwater Marsh (University of California–Natural Reserve System), approximately 6 km NNE from the site along San Diego Creek. Biomass normalized net emission rates are shown for *F. grandifolia* and *B. maritima* (Figure II.3). The emission values for CH₃Br and CH₃I shown in Figures II.2 and II.3 have been scaled up by appropriate factors to allow emissions of all three methyl halides to fit on the same vertical scale. For instance, in Figure II.2a, the actual measured CH₃Br and CH₃I fluxes from *Spartina* have been multiplied by factors of 4 and 2, respectively, to give the plotted values.

Emissions correlations. We analyzed the data by determining the linear correlation coefficients between monthly emission rates and monthly mean ambient temperature, and monthly insolation. Fitting the data to several nonlinear regression models such as exponential and rectangular hyperbola, yielded poorer correlations. Only weak correlations ($r < 0.7$) were observed, except for the correlation of CH₃I emission to temperature by *Spartina* ($r = 0.83$) and *Batis* (biomass-based; $r = 0.75$).

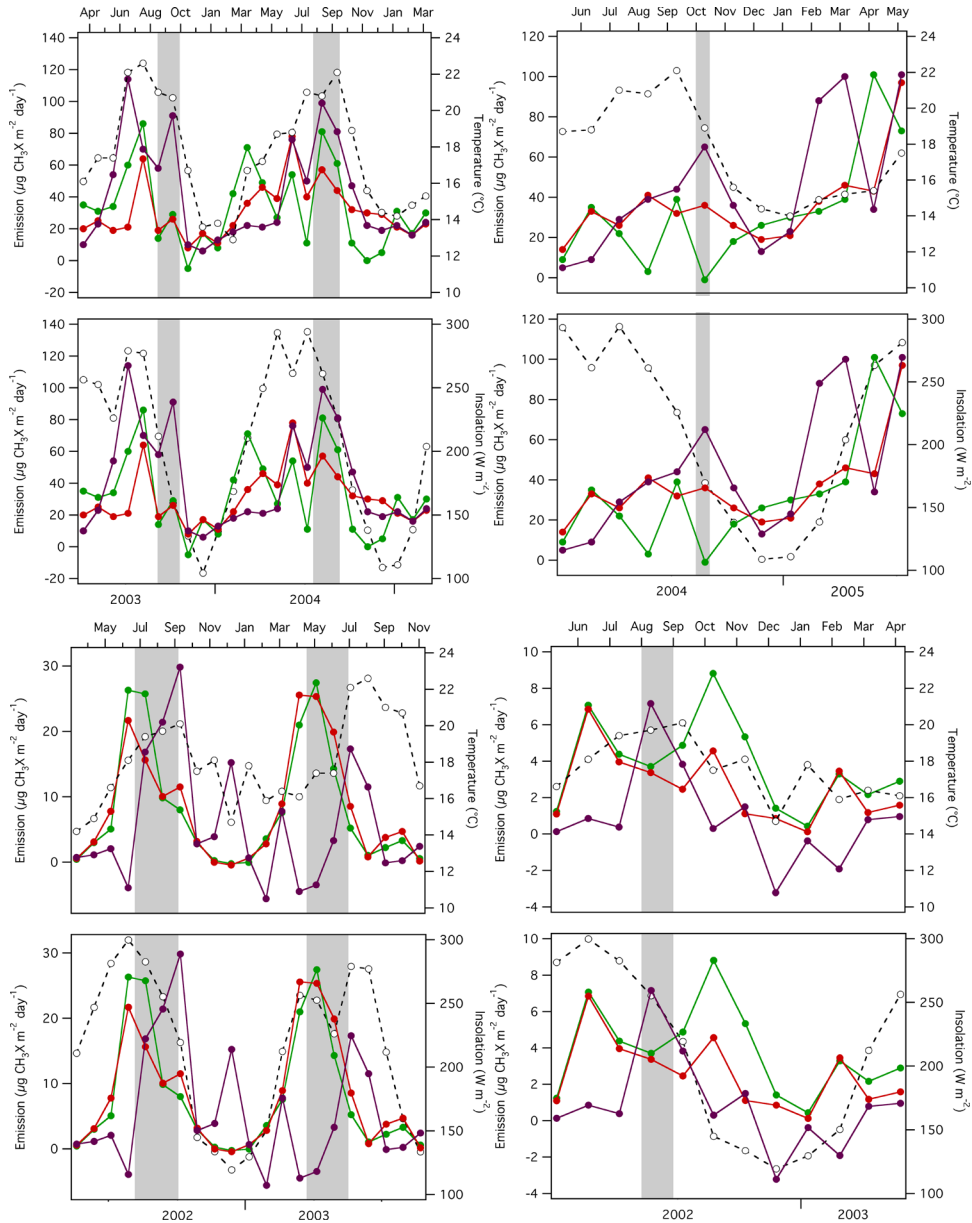


Figure II.2: Monthly mean methyl halide emissions. Methyl halide emissions ($\mu\text{g m}^{-2} \text{d}^{-1}$; CH_3Cl , green; CH_3Br , red; CH_3I , purple) from plant species with corresponding monthly mean temperature and insolation (open circles). Emissions of CH_3Cl are shown on the y axis. Actual values for CH_3Br and CH_3I emissions can be determined by dividing the graphed values by the factors indicated: a) *Spartina* (upper left), April 2003 to March 2005 ($\text{CH}_3\text{Br} \div 4$, $\text{CH}_3\text{I} \div 2$); b) *Salicornia* (upper right), May 2004 to May 2005 ($\text{CH}_3\text{Br} \div 4$, $\text{CH}_3\text{I} \div 8$); c) *Frankenia* (lower left), March 2002 to November 2003 ($\text{CH}_3\text{Br} \div 8$, $\text{CH}_3\text{I} \div 80$); d) *Batis* (lower right), May 2002 to April 2003 ($\text{CH}_3\text{Br} \div 4$, $\text{CH}_3\text{I} \div 20$). Shaded rectangles indicate flowering period.

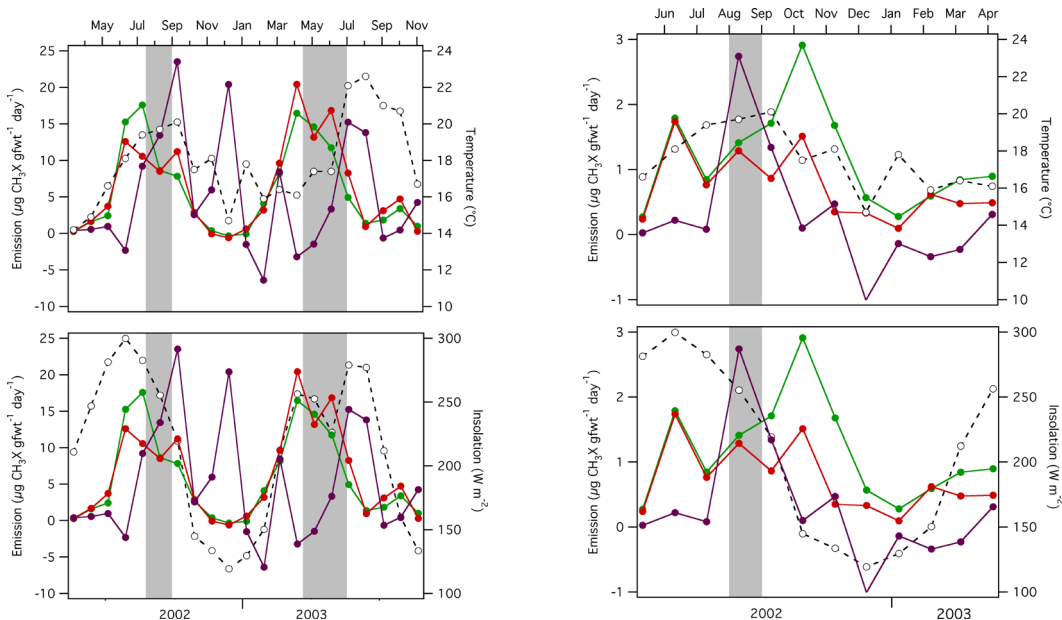


Figure II.3: Biomass specific monthly mean methyl halide emissions. Biomass (grams fresh weight) normalized methyl halide emissions ($\mu\text{g gfw}^{-1} \text{d}^{-1}$; CH_3Cl , green; CH_3Br , red; CH_3I , purple) and corresponding monthly mean temperature and insolation (open circles). Emissions of CH_3Cl are shown on the y axis. Actual values for CH_3Br and CH_3I emissions can be determined by dividing graphed values by the factors indicated: a) *Frankenia* (left), March 2002 to November 2003 ($\text{CH}_3\text{Br} \div 8$, $\text{CH}_3\text{I} \div 80$) and b) *Batis* (right), May 2002 to April 2003 ($\text{CH}_3\text{Br} \div 4$, $\text{CH}_3\text{I} \div 20$). Shaded rectangles indicate flowering period.

Mean monthly insolation was most often more highly correlated to emissions than mean monthly temperature. Mean monthly temperature changes, however, rarely exceeded $10\text{ }^\circ\text{C}$ and were usually not highly correlated with methyl halide emissions. In most instances, either temperature or insolation, for the month in which the emissions were measured, displayed the highest levels of correlation. Occasionally, it was the previous month's temperature or insolation that more closely correlated with emissions. Only at shifts of -1 month was r sometimes greater than r when no shift was applied. A shift in the emission data to one month previous insolation resulted in an increased correlation for CH_3Br produced by *Batis* and *Spartina* only ($r = 0.7$ for

both). *Salicornia* emissions were poorly correlated with monthly mean temperature and insolation ($r < 0.36$). In no instances did the same factor correlate with emissions of all three methyl halides from a given plant. Therefore, it is impossible to draw general conclusions about the effects of ambient temperature and insolation on methyl halide emissions from coastal salt marshes.

Flowering. The dramatic increase in biomass normalized CH₃Cl and CH₃Br emission by *Frankenia* was correlated with flowering (Figure II.3a). Flowering in *Batis* corresponded to a striking increase in biomass normalized CH₃I emission and a secondary spike in CH₃Br emission (Figure II.3b). Area normalized emissions of CH₃Cl and CH₃Br from the *Spartina* site correspond to this flowering pattern (Figure II.2a; 19 and 21 flowers maximum for 2003 and 2004, respectively). *Salicornia* flowering corresponded with a peak in CH₃I emissions (Figure II.2b). Although flowering does not correlate with an increase of all three methyl halides for any given plant, in general the flowering period is associated with increased emissions.

Chamber temperature and other factors. Initial chamber temperature and average chamber temperature during the incubation period were weakly or not correlated to emissions for all three methyl halides for all plants. *Spartina* CH₃Br and CH₃I emissions during non-flowering periods were poorly correlated to average chamber temperature ($r = 0.5$ and 0.3 , respectively), however, CH₃Cl emissions were weakly correlated ($n = 30$; $r = 0.70$). Methyl halide emissions by *Spartina* (located low in the marsh) and *Frankenia* (located in mid and high marsh) were not correlated

with height of last high tide, time since last high tide, or tidal strength (height of last high tide/time since last high tide; $r < 0.05$).

Soil and mud emissions. Annual emissions of CH₃Cl and CH₃Br from the soil and mud (control incubations) were smaller than their emissions from the plant by approximately an order of magnitude (Table II.2). Methyl iodide emissions from *Spartina* and *Salicornia* and their controls were similarly related. The area surrounding *Spartina* (mud) and *Salicornia* (soil/mud) produced low levels of CH₃I throughout the year with peak emissions in the late summer. The emission of CH₃I from the soil where *Batis* and *Frankenia* were located was greater than or equal to plant emissions and peaked in late summer. Net consumption of CH₃I by soil or mud rarely occurred, whereas consumption of the other two gases occurred more frequently, primarily in the winter.

Table II.2: Annual methyl halide production from coastal salt marsh plants and controls^a

Species	Spartina		Salicornia		Batis		Frankenia	
	Plant	Control	Plant	Control	Plant	Control	Plant	Control
CH ₃ Cl mg m ⁻² yr ⁻¹	12	1.6	12	1.4	1.4×10 ³	90	2.6×10 ³	130
CH ₃ Br mg m ⁻² yr ⁻¹	2.8	0.32	3.2	0.36	230	19	340	25
CH ₃ I mg m ⁻² yr ⁻¹	7.6	0.88	2.0	0.59	16	40	25	26

^aNet emission rates reported for plants (see text).

Plant emissions. Annual plant methyl halide emission rates normalized to grams fresh weight and dry weight (gfw and gdw, respectively) are shown in Table II.3 for these four species. The succulent plants (i.e., *Batis* and *Salicornia*) have very high water content compared to nonsucculent plants (*Spartina* and *Frankenia*),

therefore, a more accurate comparison of their intrinsic methyl halide emission rates is revealed when expressed per gdwt.

Table II.3: Tissue halide content and annual biomass specific methyl halide production from coastal salt marsh plants^a

	Tissue				
	<i>Spartina</i>	<i>Salicornia</i>		<i>Batis</i>	<i>Frankenia</i>
		this study	Ref. ¹⁴⁵		
Number of samples	5	4	39-216 ^b	18	30
Percent dry weight	25 (2)	14 (0.5)	13.2 (1.5)	16 (1)	37 (6)
Cl ⁻ content, %	6.7 (1.5)	20 (5)	24 (4)	21 (4)	6.3 (1.4)
Br ⁻ content, ‰	1.1 (0.3)	2.8 (0.8)	3.7 (1)	2.9 (0.7)	1.0 (0.2)
I ⁻ content, ppm	6.4 (3.2)	10 (3)	6.2 (3)	8 (3)	6.7 (3.6)
Mean annual biomass specific production					
$\mu\text{g CH}_3\text{Cl gfw}^{-1} \text{ yr}^{-1}$	18	2.2		420	1.9×10^3
$\mu\text{g CH}_3\text{Cl gdwt}^{-1} \text{ yr}^{-1}$	70 ^d	16 ^e		2.6×10^3	5.1×10^3
$\mu\text{g CH}_3\text{Br gfw}^{-1} \text{ yr}^{-1}$	4.0	0.60		67	260
$\mu\text{g CH}_3\text{Br gdwt}^{-1} \text{ yr}^{-1}$	16 ^d	4.3 ^e		420	700
$\mu\text{g CH}_3\text{I gfw}^{-1} \text{ yr}^{-1}$	11	0.38		5.5	23
$\mu\text{g CH}_3\text{I gdwt}^{-1} \text{ yr}^{-1}$	44 ^d	2.7 ^e		34	62

^aParenthesis: s.d.

^bValues: n = 39 for % dwt, 216 for Cl⁻ and Br⁻ content, and 162 for I⁻ content.¹⁴⁵

^cExcluding very high months of September and October.¹⁴⁵

^dDetermined using a yearly mean biomass density of 171 gdwt m⁻².¹⁴⁷

^eDetermined using a yearly mean biomass density of 750 gdwt m⁻².¹⁴⁸

Annual biomass normalized methyl halide emission rates for *Batis* and *Frankenia* are the mean of all direct measurements. The annual biomass-normalized methyl halide emission rates for *Salicornia* and *Spartina* were indirectly determined because the plants were not harvested. The yearly mean *Salicornia* biomass density of 750 gdwt m⁻², determined at Mugu Lagoon (Ventura County, California¹⁴⁸), and the yearly mean *Spartina* biomass density of 171 gdwt m⁻², determined from the Tijuana Estuary (San Diego County, California¹⁴⁷), were therefore used. Biomass

normalized emissions ($n = 9$) from *Salicornia* were also directly measured using the small glass chamber followed by harvesting. The rates were similar to those in Table II.3 ranging from 0.5-18 $\mu\text{g CH}_3\text{Cl gdw}^{-1} \text{ yr}^{-1}$, 0-1.3 $\mu\text{g CH}_3\text{Br gdw}^{-1} \text{ yr}^{-1}$, and 0.11-3.5 $\mu\text{g CH}_3\text{I gdw}^{-1} \text{ yr}^{-1}$, even though it was difficult to ensure a tight seal (which prompted the change to a permanent base). *Spartina* biomass normalized rates were determined 3 times (November, June and August) using biomass density determinations near the site where emission fluxes were measured. The rates were similar to those in Table II.3 ranging from 0-38 $\mu\text{g CH}_3\text{Cl gdw}^{-1} \text{ yr}^{-1}$, 1.4-12.8 $\mu\text{g CH}_3\text{Br gdw}^{-1} \text{ yr}^{-1}$, and 4-13 $\mu\text{g CH}_3\text{I gdw}^{-1} \text{ yr}^{-1}$.

Plant tissue halides. Tissue halide content for these plants is also shown in Table II.3. Although the infrequent sampling probably masked any significant seasonal changes, values are shown to confirm that halides are present in high concentrations. The succulent species *Batis* and *Salicornia* contain more halides than the nonsucculent plants.

This work extends and refines the research of Rhew et al.¹³⁷ in the estimation of methyl halide emission from coastal salt marshes. The present study differs significantly from the former in that only single plant species were chambered (no species mixtures), transparent chambers were used allowing for plant photosynthesis, and the sampling frequency was much greater and covered an entire year or more. Measuring emissions from individual species permitted direct interspecies comparisons, which, in conjunction with plant coverage data, allows for a more

accurate assessment of salt marsh methyl halide emissions. We also included production of methyl halides from barren areas in our estimations.

The use of transparent chambers ensured that the plants were photosynthetically active. If methyl halide production is coupled to C fixation, the use of transparent chambers would maintain this relationship. Methyl halides are formed enzymatically (methyl transferases) using S-adenosyl-L-methionine (SAM) as the methyl donor to methylate halides.^{134,149} Such methylations, however, are generally not directly coupled to primary metabolism (e.g., photosynthesis). The lack of coupling between methyl halide production and photosynthesis is supported by the observations that algal and rice methyl halide production is not enhanced in the light.^{144,150} Diurnal patterns in methyl halide emissions have been reported for various ecosystems including rice paddies¹⁴⁴ and salt marshes.^{137,151} However, some of these patterns may have been in response to changing ambient temperature rather than irradiance.¹⁴⁴

Higher sampling frequency and determination of emissions on the basis of chambered area and plant biomass allowed for a more accurate description of the seasonal patterns of methyl halide emissions. Emissions showed a pronounced seasonality caused not only by seasonal changes in biomass density, but also due to a physiological activation of the emission process. Such an approach identified flowering as an important event (see below).

Seasonal emission patterns. Our degree of sampling allowed for the detection of a strong seasonal signal and monthly differences. Monthly emissions of CH₃Cl

and CH₃Br from *Spartina* and *Frankenia* were more highly correlated with monthly insolation than monthly temperature because of its dramatic effect on seasonal biomass via growth. These two species show a pronounced biomass change with the seasons, with day length presumably having the greatest effect on growth.

During the winter, aboveground biomass of *Spartina* senesced and disappeared, with new shoots emerging in the spring. During the winter, green tissue of *Frankenia* also disappeared leaving only woody twigs. Whereas CH₃I emission was strongly correlated to monthly temperature for *Spartina*, that was not the case for *Frankenia*. Clearly CH₃I emissions from these two species are controlled by different physiological processes than are the emissions of the other methyl halides.

Batis showed little change in biomass with seasons, and the area-based emissions were less highly correlated with either temperature or insolation as compared to the other plants. Biomass-based CH₃I emissions by *Batis* do show a strong temperature influence suggesting greater metabolic activity in the production of this gas during the warmer months.

Salicornia is a plant with a woody base supporting succulent tissue and the ratio of woody stem to succulent tissue increases dramatically in the winter.¹⁴⁸ In the winter there was a decrease in CH₃I emissions; CH₃Br emissions showed a slight decline, and CH₃Cl emissions were relatively unchanged. There was much more biomass and succulent tissue present in the spring of 2005 than in the spring and summer of 2004 which corresponded to overall greater methyl halide emissions in the spring of 2005. Although there were poor correlations between methyl halide emissions from *Salicornia* and monthly temperature, CH₃Cl and CH₃Br emissions did

correlate slightly with insolation showing succulent tissue dependency. A stronger correlation may have been masked by the large increase in emissions and biomass that occurred in 2005 after heavy summer rains.

We could not correlate emissions with tidal or rainfall patterns on a daily, weekly or monthly scale. Presumably tides and rainfall did not influence emissions directly, apart from their effect on overall plant health and growth. In most cases, mean chamber incubation temperatures were weakly correlated to daily emissions, even when those emissions were separated into flowering and non-flowering categories. Positive correlations between emissions (e.g., CH₃Cl emissions from *Spartina*, non-flowering) and temperature may have been due to the effect of temperature on diffusion and the rate of enzyme-catalyzed methyl halide synthesis. Negative correlation between emissions (e.g., CH₃I emissions by *Spartina* during 2003 flowering and CH₃Br emissions by flowering *Salicornia*) and temperature may have been a result of inhibition of methyl halide biosynthesis at high temperatures. The highest chamber temperatures were not generally associated with average monthly temperatures (e.g., chamber temperature for *Spartina* of 34.6 °C occurred 12/03) and thus did not amplify the seasonal signal. The negative correlations between temperatures and emissions during the flowering period may have resulted in an underestimation of emission peaks associated with flowering. The use of temperature-controlled chambers would have been beneficial.

Intrinsic plant variation in methyl halide emissions. Calculating the yearly biomass specific methyl halide emission rates, especially those based on dry weights,

(Table II.3) demonstrates an inherent difference in emissions amongst species. *Frankenia* and *Batis* biomass specific emission rates for CH₃Cl and CH₃Br were at least an order of magnitude greater than the rates for the other two species. The biomass specific emission rates for CH₃I by *Frankenia* were also greater than the rates from *Spartina* and *Salicornia*, but the CH₃I emissions from *Batis* exceeded only those of *Salicornia*.

The values were empirically determined for *Batis* and *Frankenia* and were calculated based on seasonal determinations of biomass for *Salicornia* and *Spartina* from other studies. The biomass of above ground tissue of *Salicornia* in a southern California salt marsh reaches a maximum in the summer (~1000 gdwt m⁻², 20–40% succulent tissue) compared to the winter (~500 gdwt m⁻², 3% succulent tissue), with slightly more succulent tissue peaking in June and woody tissue peaking in August.¹⁴⁸ Biomass normalized emissions calculated for *Salicornia* (Table II.3) were very similar to those few direct measurements. The mean biomass density from these limited determinations was 649 gdwt m⁻², which is similar to the yearly mean of 750 gdwt m⁻²,¹⁴⁸ validating our approach.

Spartina aerial biomass (using height and numbers of stems as a proxy) in a southern California salt marsh peaks in July and again in September when fruiting, and is at a minimum throughout the winter.^{147,152} The limited measurements of *Spartina* biomass densities (570 gdwt m⁻²) was 3 times the yearly mean determined from the work of Zedler and Nordby¹⁴⁷ but well within reported growing season maximums of 211-898 gdwt m⁻².^{147,152} The mean annual biomass density calculated for *Batis* and *Frankenia* were 520 and 470 gdwt m⁻², respectively.

Normalizing emissions to the amount of chambered aerial tissue biomass revealed seasonal emissions inherent to each plant species independent of biomass density (Figure II.3). This increase in methyl halide emission demonstrates physiological control of the process. Such control could involve the increase in the synthesis of the methyl transferase(s) involved in methyl halide production and/or increased activity of the enzyme.

The seasonal emission peak of certain methyl halides corresponded with flowering in *Batis* (CH₃I in August) and *Frankenia* (CH₃Cl and CH₃Br in late spring/early summer). The CH₃I emission peak for *Spartina* in August 2004 and for *Salicornia* in October 2004 also corresponded with flowering, but because data are not normalized to biomass but to chambered area, the peaks may be influenced by biomass increases. Clearly flowering is related to the production of certain methyl halides, depending on the plant species. Flowering in rice corresponded to a large increase in CH₃Br emissions and a minor peak in CH₃I emissions.¹³⁹

Plants contain many different types of SAM-utilizing methyl transferases defined by the different organic substrates that they methylate.¹⁴⁹ A variety of purified methyl transferases (caffeic acid OMT, caffeoyl-CoA OMT, flavanol OMT, salicylic acid carboxyl MT) have been shown to catalyze the methylation of bromide in the presence of SAM.¹⁴⁹ The latter enzyme had the highest specific activity in producing CH₃Br. Salicylic acid carboxyl MT isolated from petals of the plant *Clarkia breweri* functions to create the volatile compounds associated with this flower to attract insects.¹⁵³ Such a methyl transferase may be present during flowering of these salt marsh species and secondarily methylate the respective

halides. Although *Spartina* is a wind pollinator and may not produce volatile insect attractants, increased CH₃I emissions were correlated with flowering for both years studied.

Intrinsic differences in methyl halide production by plants are also revealed by examination of the molar ratios of emissions (Table II.4). Each plant has its own distinct ratio pattern. However, *Spartina* and *Salicornia* have similar CH₃Cl:CH₃Br ratios, as do *Frankenia* and *Batis*. The latter two species also share similar CH₃Cl:CH₃I and CH₃Br:CH₃I ratios, reflecting similar emission fluxes for all compounds.

Table II.4: Linear correlation coefficients (*r*) and molar ratios for monthly methyl halide production from coastal salt marsh plants and controls

Species	CH ₃ Cl versus CH ₃ Br		CH ₃ Cl versus CH ₃ I		CH ₃ Br versus CH ₃ I	
	<i>r</i>	ratio	<i>r</i>	ratio	<i>r</i>	ratio
<i>Spartina</i>	0.84	8.3	0.53	4.6	0.67	0.55
Control	0.87	9.7	0.81	5.2	0.88	0.53
<i>Salicornia</i>	0.54	7.4	0.25	17	0.73	1.8
Control	0.50	7.8	0.22	6.9	0.59	0.90
<i>Batis</i>	0.78	12	0.25	252	0.21	21
Control	0.14	9.1	0.92	6.3	-0.06	0.71
<i>Frankenia</i>	0.98	15	-0.10	299	-0.17	21
Control	0.62	9.9	-0.21	14	-0.07	1.4

The linear correlation between CH₃Cl and CH₃Br monthly emissions was moderate to high (*r* > 0.7) for all plant species except *Salicornia*, suggesting synchronized production (Table II.4). *Frankenia* showed the highest correlation between CH₃Cl and CH₃Br (*r* = 0.98) because the emissions of these gases were enhanced during flowering, whereas with the other species only CH₃I emissions were primarily enhanced during flowering. The correlation between CH₃Cl and CH₃Br for a Tasmanian coastal wetland site (Cape Grim, 40 °S, 145 °E) dominated by the

succulent halophyte *Pachycornia arbuscula* (basionym *Salicornia arbuscula*) was also high ($r = 0.86^{138}$), however, we found the correlation based on our integrated mean with related species *S. virginica* low ($r = 0.35$).

Intrinsic plant variation in tissue halide content. Except for the species *Salicornia*,¹⁴⁵ this is the first time all three halides have been measured in these halophytes (Table II.3). *Batis* and *Salicornia* contain more halides than *Frankenia* or *Spartina*, because of their strategy to survive in saline soils by maintaining a large amount of tissue water (succulence) with which to sequester salts in cell vacuoles.¹⁵⁴ It is anticipated that other halophytes would also be prolific methyl halide producers because of their high tissue halide levels.

The frequency of analysis for tissue halides may have missed any significant seasonal differences in tissue halide content for the various halophytes. *Salicornia* chloride and bromide levels were slightly lower in the late winter of 2003 as compared to summer of 2002, presumably as a response to increased succulence.¹⁴⁵ This conceivably could affect CH₃Cl and CH₃Br emissions. However, in the winter, much of the green tissue of *Salicornia* disappeared, leaving mostly woody stems above ground, and the decline is most likely a response to overall lack of metabolic activity. In marked contrast, during the flowering period of September and October of 2002, iodide tissue levels increased by several orders of magnitude.¹⁴⁵ The peak emission of CH₃I also corresponded with flowering during a different year (Figure II.2b). This excess iodide, possibly in concert with flower methyl transferase activity, may be responsible for the October peak in CH₃I production in this species. The peak

in CH₃I in March of 2005 corresponded with the development of new green succulent tissue associated with renewed growth.

The mean molar ratio of CH₃Cl:CH₃Br:CH₃I produced by the plants was 144:11:1, which was smaller than for tissue halides, 5.4×10^4 :420:1, and seawater, 5.4×10^6 : 8.2×10^3 :1. There is selective uptake of halides with I⁻ > Br⁻ > Cl⁻, and there is selective methylation following the same trend. Methyl transferase isolated from *Batis* shows a higher affinity with I⁻ > Br⁻ > Cl⁻.¹³⁴ Our molar ratio of CH₃Cl:CH₃Br plant emissions was 12 ± 3 (sd), which was comparable to 17 ± 14 , as reported by Rhew et al.¹³⁷ for all plants.

Methyl halide emission from mud and soil. The soil/mud mixed control for *Salicornia* was most similar in methyl halide flux to the estuarine mud control for *Spartina*, except the *Spartina* control showed greater CH₃I production. The *Batis* and *Frankenia* soil controls were also most similar in emissions, suggesting similar production mechanisms. Emissions of CH₃Cl and CH₃Br from mudflats and mid marsh soil were smaller than from plants. A weak seasonal signal for CH₃Cl emissions was detectable only for mid-marsh soil and for CH₃Br emissions from mud. The uptake of CH₃Cl and CH₃Br was more pronounced in the mid marsh soil occurring primarily, but not exclusively, in the winter. Rarely were these gases taken up by mud. Microbial production in mud throughout the year may have accounted for the very low level emission of these gases. Their emission from mid-marsh soil during the summer may have also been microbially produced, with production ceasing in the winter. Emissions from mud in a tidal channel with the green seaweed

Enteromorpha present¹³⁷ were approximately 2.6 times greater than our average emissions of CH₃Cl and CH₃Br from mud. Green seaweeds are known producers of methyl halides.^{155,156}

Benthic diatoms are a common component of estuarine mud¹⁵⁷ and micro algae, including diatoms, are known to produce CH₃I.¹⁵⁸⁻¹⁶⁰ Methyl iodide is the major alkyl iodide found in estuarine sediments, with a concentration range of 1-3.5 pg gdw⁻¹ sediment.¹⁶¹ It may also be formed abiotically during oxidation of organic matter in sediment.¹⁶²

Highly significant CH₃I emissions also occurred from barren soil. The magnitude of emission (g yr⁻¹) was 5.6 times that of the estuarine mud. We attribute this large CH₃I emission to plant roots and associated microbes presumably present under the barren surface. Controls for *Batis* and *Frankenia* were routinely close to the standing plants and the CH₃I emission rates from these soils were surprisingly similar (Table II.2). Root mycorrhizal fungi, known producers of CH₃I¹⁶³ may have also contributed to this large CH₃I emission.

Greenhouse-grown mangroves

After an apparent lag phase of growth of 170 days for both species, a steady and apparently healthy growth increase of 10% and 7.8% per week ensued for *A. germinans* and *R. mangle*, respectively. These growth rates are similar to those derived from the data of Smith and Snedaker¹⁶⁴ for mean leaf index of *R. mangle* seedlings grown in outdoor containers: mean growth between days 99 and 144 ranged from 1 to 6% per week.

Throughout the study all the plants appeared healthy and showed no evidence of chlorosis or disease. *A. germinans* and *R. mangle* developed their characteristic root types: pneumatophores (breathing roots) and stilt roots (support roots), respectively. The rate of leaf area increase declined slightly for both plant species between the last two dates of measurements (beginning at $t = 355$ days for both species and ending at $t = 473$ days for *A. germinans* and $t = 510$ days for *R. mangle*) due to leaf senescence. New leaves, however, were continually being produced during this period.

Effects on emissions. Chamber temperature during the incubation of the mangroves had no measurable effect on methyl halide emissions. All the methyl halide emission measurements were weakly linearly correlated with incubation temperature for either *A. germinans* (r^2 from -0.10 to +0.17) or *R. mangle* (r^2 from -0.02 to +0.14).

For the last two 90 min incubations of *A. germinans*, when leaf area was above 3,000 cm² (growth period 3), photosynthesis may have become CO₂ limited based on the known photosynthetic rate of 9.7 μmole CO₂ m⁻² leaf area s⁻¹ measured in the tropical midday sun (integrated photon flux density = 2100 μmole m⁻² s⁻¹).¹⁶⁵ Our daytime greenhouse incubations, however, were performed at a photon flux density of 300 – 350 μmole m⁻² s⁻¹ at the canopy top (daylight only; lighting turned off). We calculated that 40% of the entrained CO₂ would have been consumed. Examination of the methyl halide emission kinetics over these long time intervals yielded linear correlations of $r^2 > 0.9$. Carbon dioxide limitation did not appear to

have affected methyl halide emissions. During the incubation periods, stomatal pores probably were not closed, because the plants were never subjected to water stress, and remained open to facilitate CO₂ uptake and methyl halide efflux. Methyl halide emissions from rice were similar during light and dark periods.¹⁴⁴

Mean methyl halide emissions for each growth period are shown in Table II.5. Period 1 is when seawater was initially added incrementally to 15‰. The salinity was maintained between 10 and 15‰ during Period 2. Salinity was increased to 18‰ at the start of Period 3 and maintained between 18 and 28‰ throughout the remainder of the study.

Table II.5: Methyl halide emission from greenhouse-grown mangroves

Growth period	Days after planting	Salinity (‰)	Mean methyl halide emissions per leaf area ^a (ng cm ⁻² d ⁻¹)					
			CH ₃ Cl		CH ₃ Br		CH ₃ I	
			A ^b	R ^c	A	R	A	R
1	60-150	increased 1 to 15	-6.2 (10)	11 (10)	-0.02 (0.10)	0.24 (0.40)	12 ^d (4.2)	2.3 (2.0)
2	150-240	maintained 10-15	6.0 (6.0)	2.5 (0.5)	1.0 (1.1)	0.21 (0.26)	0.94 (1.6)	-0.03 (0.18)
3	> 240	maintained 18-28	4.5 (4.0)	1.6 (1.1)	0.56 (0.40)	0.09 (0.13)	1.4 (0.7)	0.58 (0.24)
Mean, all periods			1.5	5.3	0.52	0.18	4.8	1.0

^aParenthesis: s.d.; n = 4 except for growth period 3 for *R. Mangle* where n = 3.

^b*A. germinans*.

^c*R. mangle*.

^dSignificantly different from other growth periods (p ≤ 0.05).

Species comparison. The mean emission rates for a given methyl halide and mangrove during each growth period were not statistically different from each other (p < 0.05) except for the emission of CH₃I during the first growth period by *A. germinans*. The production of CH₃Cl by *A. germinans* was lower during growth

period 1 as compared to the other growth periods at $p = 0.11$. Because of high variability, there was no significant difference between the two mangroves ($p \leq 0.05$) in the mean emission of a given methyl halide over the entire study. *A. germinans* tended to emit more CH_3I than *R. mangle* ($p = 0.13$). *R. mangle* tended to emit more CH_3Cl but with much less certainty ($p = 0.28$) because of its extremely high emission during growth period 1 compared with net uptake for *A. germinans*.

During growth period 1 for *A. germinans*, net uptake of CH_3Cl occurred during 3 of the 4 measurements and net uptake of CH_3Br occurred for half the measurements. Relatively high net emissions of CH_3I were measured during this period. Net uptake of methyl halides by chambered plants was inferred because no concentration changes were detected, while net emissions occurred from the soil control. Seawater additions began during this period and presumably a transition in the soil microbial community was taking place.

Also occurring during this period was increased root development with pneumatophores becoming evident from *A. germinans*. Undoubtedly the biological (microbial and faunal) and chemical composition of container soil was very different from that in a mangrove forest. Any processes occurring therein, affecting soil methyl halide emissions or uptake, are probably not representative of the natural condition. The dominant emission of CH_3Cl and CH_3Br from the chambered soil may have been a result of a changing microbial community and/or production from roots, although no visible pneumatophores were enclosed. Clearly CH_3I was being emitted from the aerial part of the plant.

Except for the first day of measurement for *R. mangle*, there were net plant

emissions for all three gases during growth period 1, with CH₃Cl dominant. Methyl halide emission was highest during this period and tended to decline with growth. During growth period 1, stilt roots emerged from the main trunk of *R. mangle*. Control emissions were less from *R. mangle* controls than from *A. germinans* controls during growth period 1, perhaps because of less root development. Control emissions from both bins were more similar during the other two growth periods.

Leaf area analysis. Direct comparisons of methyl halide emissions between these mangroves and other plants cannot be made because plant biomass was not measured and consequently emissions are not normalized to biomass. Estimates of emissions per land area can be made, however, using the above determinations of methyl halide emissions and estimates of leaf area index (LAI; single sided leaf area/ground area) for each species. This is a more accurate method of estimation rather than using the surface area because our plant density was not similar to natural mangrove stands. LAI estimated from our data (not shown) increased over time reaching a maximum during growth period 3: 1.9 for *R. mangle* and 2.6 for *A. germinans*, which is low compared to field values, as would be expected from juvenile trees. LAI determinations for *R. apiculata* have been reported (mean \pm SD) as 5.1 ± 0.11 ranging from 2.2 to 7.4,¹⁶⁶ 4.4 ± 0.26 for an *R. mangle* dominated stand,¹⁶⁷ and 5.7 ± 1.8 for an *R. mangle* basin type stand.¹⁶⁸ Although no LAI values for *Avicennia* could be found, a mixed mangrove stand of *R. mangle*, *Lagunacularia racemosa*, and *A. germinans* growing with *Concarpus erectus* (tropical buttonwood) had an LAI range of 0.8 to 7.0, with a mean of 4.0.¹⁶⁹

Methyl halide emissions normalized to land area were calculated using emission rates for these two species from growth period 3 and the mean emission rate for the entire study. An LAI of 5 was used, which approximates the average values determined from field studies. Growth period 3 was the longest period of the study and the most stable environmentally, with the maximum salinity maintained and temperature being controlled by computer for most of this period. During growth period 3 there was only a single instance of measured net uptake of a methyl halide: CH₃Br uptake by *R. mangle*. Emissions for this period may be a more accurate representation of what occurs naturally. The mean methyl halide emission by the two mangroves during period 3 were close to being significantly different for CH₃Cl and CH₃Br ($p = 0.10$), and for CH₃I ($p = 0.06$). The mean emissions for a given methyl halide by the two mangroves over the entire study were not significantly different.

Comparison to coastal salt marshes. Using rates from growth period 3, calculated CH₃Cl emissions per land area (mg m⁻² d⁻¹; LAI = 5) from these two mangrove species were within the range reported for coastal salt marsh plants. Mangrove emissions of CH₃Cl may contribute to the strong CH₃Cl emissions associated with tropical coastlines.¹⁴⁰ Methyl bromide emissions tended to be similar to the lower emitting salt marsh plants (*Spartina* and *Salicornia*), while CH₃I emissions were similar to the high emitting salt marsh plants (*Batis* and *Frankenia*). Methyl iodide emissions by mangroves during growth period 3 are not as high as that from rice, which uses CH₃I as a means to rid itself of tissue iodide.¹⁴⁴ Rice values, however, are based on a single growing season of approximately 110 days.

Plant tissue halides. Analysis of leaf tissue halide content collected over growth period 3 (n = 3) yielded the results shown in Table II.6. Comparing our values of tissue halide content in *R. mangle* to those measured by Market and Jayasekera,¹⁷⁰ only our chloride content is comparable. This could be due to a difference in plant maturity, as our analysis of a tissue sample from a mature tree yielded results within the range for Market and Jayasekera for all three halides. The chloride and bromide values were significantly different between the two greenhouse-grown species at $p < 0.1$. The iodide values were not significantly different ($p = 0.35$). Although the leaf halide concentrations are greater in *R. mangle* during growth period 3, methyl halide emissions are greater in *A. germinans* during this period. These species have different strategies to tolerate and grow in high salinity conditions. *Avicennia* rids itself of excess salt by actively excreting it through its leaves, while *Rhizophora* selectively excludes ions by ultrafiltration and stores excess ions in cell vacuoles.¹⁴³ The cell vacuoles of *Rhizophora* may sequester halides from methyl transferases, the enzyme responsible for methyl halide biosynthesis in plant tissue.¹⁷¹

Table II.6: Tissue halide content of greenhouse-grown mangroves

	Tissue			
	<i>A. germinans</i>	<i>R. mangle</i>		
		this study	mature tree ^a	ref. ¹⁷⁰
Cl ⁻ content, %	4.9	9.0	5.0	1 – 10
Br ⁻ content, ‰	1.1	2.0	0.8	0.1 – 1.0
I ⁻ content, ppm	6.3	13	1.6	< 6.0

^aMature *R. Mangle* tree obtained from a natural population near Ft. Pierce, Florida.

Global extrapolation. An estimate of global mangrove methyl halide production can be made using the above determinations of methyl halide emissions, an LAI of 5 and an estimate of global mangrove surface coverage ($2 \times 10^5 \text{ km}^2$).¹⁷² The combined mean methyl halide emissions for both mangroves during period 3 (Table II.5) were used to calculate global mangrove emissions: 11 Gg $\text{CH}_3\text{Cl y}^{-1}$, 1.2 $\text{CH}_3\text{Br Gg y}^{-1}$ and 3.7 $\text{CH}_3\text{I Gg y}^{-1}$. Using the combined mean methyl halide emissions for both mangroves over the entire study period to calculate global mangrove emissions yielded 12, 1.3 and 11 Gg y^{-1} for CH_3Cl , CH_3Br and CH_3I , respectively. Using the CH_3Cl global sink strength of 4005 Gg y^{-1} reported by Montzka et al.,¹³² our preliminary analysis shows mangroves producing 0.3%. Using global sink strengths¹³¹ of 205 Gg $\text{CH}_3\text{Br y}^{-1}$ and 258 Gg $\text{CH}_3\text{I y}^{-1}$ indicate that mangroves contribute approximately 0.6% to global CH_3Br production and no more than 4% to global CH_3I production. From these preliminary determinations, only CH_3I emissions emerge as globally significant.

Conclusion

Methyl halide emissions from coastal salt marshes. The results of this study demonstrate that the plants inhabiting the salt marsh community have dramatically different intrinsic abilities to produce methyl halides (Table II.3). Also, a plant species that covers a relatively small area (e.g., *Batis*, *Frankenia*) can make a significant contribution to the total methyl halide emitted from the marsh. Conversely, a plant species that covers a large area, such as *Spartina*, can be an

overall minor contributor of methyl halides. The accuracy of the estimated methyl halide emissions can be dramatically improved by increasing the number of species being measured. Our estimation of methyl halide emissions from coastal salt marshes could still be low because we did not measure eight species present in UNB, including *Scirpus californicus* (Bulrush) with 14% cover in the UNB upper marsh and *Tiglochin maritime* (Sea lavender) with 11% cover in UNB middle marsh.

We did not account for possible diurnal patterns in methyl halide emission from plants. It is unclear if any or all halophytes exhibit this response, and if so, the amplitude of the response wave. *Batis* and *Salicornia* have shown increased CH₃Cl and CH₃Br emission with a peak corresponding with maximum daylight.^{137,151} The magnitude of the response varied depending on the methyl halide emitted and the plant species examined. It is possible, however, that these diurnal emissions changes were artifacts due to changes in plant metabolism. The chambers used by Rhew et al.^{137,151} blocked the plants from sunlight during the incubation period of 15 to 40 min. During that period the plant would undergo a dramatic metabolic shift, from photosynthesis to respiration as indicated by an increase in chamber CO₂. The effect of these metabolic changes on methyl transferase activity is unknown. Ambient air temperature also increased and may have had a direct effect on respiration and methyl halide production. Similar incubations in transparent chambers with regulated temperature would confirm the existence of a diurnal response.

Methyl halide emissions from tropical mangrove forests. This work also represents the first measurements of methyl halide emissions in mangroves.

Although caution must be taken applying emissions derived from a single individual grown in a greenhouse to natural populations, methyl halide emissions from greenhouse-grown rice are very similar to those measured in the field.^{139,144} This work utilized the same bins and greenhouse used for the rice experiments. The two species chosen were from 2 dominant mangrove genera, however, juvenile trees may have inherently different emission rates (per unit biomass or leaf area) than mature trees. We also did not take into account possible emissions from roots and stems, or the possibility of enhanced emissions during flowering as seen in the coastal salt marsh measurements. Clearly a more accurate determination must be conducted on natural populations. Tidal fluxes, rainfall, biogeochemical processes, and community interactions would all affect the growth and physiology of the plant species and microbial populations present. As demonstrated for coastal salt marsh plants, accurate determinations of methyl halide production from ecosystems must involve measurements of a majority of the species present, as well as the amount of unvegetated area present. Also, plant species present in low numbers can be significant producers of certain methyl halides in the ecosystem.

REFERENCES

- (1) Intergovernmental Panel on Climate Change (IPCC), *Climate Change 2001: Synthesis Report, Summary for Policymakers*, 2001.
- (2) Intergovernmental Panel on Climate Change (IPCC), *Climate Change 2007: Contribution of Working Group I, The Physical Science Basis, Summary for Policymakers*, 2007.
- (3) Geron, C. et al., A review and synthesis of monoterpene speciation from forests in the United States, *Atmos Environ*, **2000**, *34*, 1761-1781.
- (4) Christensen, C. S. et al., Determination of the terpene flux from orange species and Norway spruce by relaxed eddy accumulation, *Atmos Environ*, **2000**, *34*, 3057-3067.
- (5) Pio, C. A. and A. A. Valente, Atmospheric fluxes and concentrations of monoterpenes in resin-tapped pine forests, *Atmos Environ*, **1998**, *32*, 683-691.
- (6) Rapparini, F. et al., Seasonal variation of monoterpene emissions from *Malus domestica* and *Prunus avium*, *Phytochemistry*, **2001**, *57*, 681-687.
- (7) Seinfeld, J. H. and S. N. Pandis, *Atmospheric chemistry and physics: From air pollution to climate change*; John Wiley & Sons, Inc.: New York, 1998.
- (8) Finlayson-Pitts, B. J. and J. N. Pitts, *Chemistry of the upper and lower atmosphere: Theory, experiments, and applications*; Academic Press: San Diego, 2000.
- (9) Zellner, R., *Global aspects of atmospheric chemistry*; Steinkopf: Darmstadt, 1999.
- (10) Jacob, D. J., *Introduction to atmospheric chemistry*; Princeton University Press: Princeton, 1999.
- (11) Brasseur, G. P. et al., *Atmospheric chemistry and global change*; Oxford University Press: New York, 1999.
- (12) Penner, J. E. et al., In *Climate Change 2001: The Scientific Basis. Contribution of Working Group I*; Houghton, J. T. et al., Eds.; Cambridge University Press: New York, 2001.
- (13) Weichenthal, S. et al., Indoor ultrafine particles and childhood asthma: Exploring a potential public health concern, *Indoor Air*, **2007**, *17*, 81-91.
- (14) Morgenstern, V. et al., Respiratory health and individual estimated exposure to traffic-related air pollutants in a cohort of young children, *Occup Environ Med*, **2007**, *64*, 8-16.
- (15) Lanki, T. et al., Associations of traffic related air pollutants with hospitalisation for first acute myocardial infarction: The HEAPSS study, *Occup Environ Med*, **2006**, *63*, 844-851.
- (16) Miller, K. A. et al., Long-term exposure to air pollution and incidence of cardiovascular events in women, *N Engl J Med*, **2007**, *356*, 447-458.
- (17) Zanobetti, A. and J. Schwartz, Particulate air pollution, progression, and survival after myocardial infarction, *Environ Health Perspect*, **2007**, *115*, 769-775.

- (18) Wellenius, G. A. et al., Air pollution and hospital admissions for ischemic and hemorrhagic stroke among Medicare beneficiaries, *Stroke*, **2005**, *36*, 2549-2553.
- (19) Kettunen, J. et al., Associations of fine and ultrafine particulate air pollution with stroke mortality in an area of low air pollution levels, *Stroke*, **2007**, *38*, 918-922.
- (20) Maynard, D. et al., Mortality risk associated with short-term exposure to traffic particles and sulfates, *Environ Health Perspect*, **2007**, *115*, 751-755.
- (21) Ostro, B. et al., The effects of components of fine particulate air pollution on mortality in California: Results from CALFINE, *Environ Health Perspect*, **2007**, *115*, 13-19.
- (22) Dockery, D. W. et al., An association between air pollution and mortality in six U.S. cities, *N Engl J Med*, **1993**, *329*, 1753-1759.
- (23) Jacobson, M. C. et al., Organic atmospheric aerosols: Review and state of the science, *Rev Geophys*, **2000**, *38*, 267-294.
- (24) Lim, H. J. and B. J. Turpin, Origins of primary and secondary organic aerosol in Atlanta: Results of time-resolved measurements during the Atlanta Supersite experiment, *Environ Sci Technol*, **2002**, *36*, 4489-4496.
- (25) Hoffmann, T. et al., Formation of organic aerosols from the oxidation of biogenic hydrocarbons, *J Atmos Chem*, **1997**, *26*, 189-222.
- (26) Jonsson, A. M. et al., Impact of humidity on the ozone initiated oxidation of limonene, Δ^3 -carene, and α -pinene, *Environ Sci Technol*, **2006**, *40*, 188-194.
- (27) Guenther, A. et al., A global-model of natural volatile organic-compound emissions, *J Geophys Res*, **1995**, *100*, 8873-8892.
- (28) Davis, K. J. et al., Biogenic nonmethane hydrocarbon emissions estimated from tethered balloon observations, *J Geophys Res*, **1994**, *99*, 25587-25598.
- (29) Janson, R., Monoterpene concentrations in and above a forest of Scots pine, *J Atmos Chem*, **1992**, *14*, 385-394.
- (30) Hayward, S. et al., Monoterpene emissions from soil in a Sitka spruce forest, *Atmos Environ*, **2001**, *35*, 4081-4087.
- (31) Warneke, C. et al., Comparison of daytime and nighttime oxidation of biogenic and anthropogenic VOCs along the New England coast in summer during New England Air Quality Study 2002, *J Geophys Res*, **2004**, *109*, D10309.
- (32) Khamaganov, V. G. and R. A. Hites, Rate constants for the gas-phase reactions of ozone with isoprene, α - and β -pinene, and limonene as a function of temperature, *J Phys Chem A*, **2001**, *105*, 815-822.
- (33) Destailats, H. et al., Indoor secondary pollutants from household product emissions in the presence of ozone: A bench-scale chamber study, *Environ Sci Technol*, **2006**, *40*, 4421-4428.
- (34) Rohr, A. C. et al., Generation and quantification of ultrafine particles through terpene/ozone reaction in a chamber setting, *Aerosol Sci Technol*, **2003**, *37*, 65-78.
- (35) Weschler, C. J. and H. C. Shields, Indoor ozone/terpene reactions as a source of indoor particles, *Atmos Environ*, **1999**, *33*, 2301-2312.

- (36) Reinhardt, A. et al., Ultrahigh mass resolution and accurate mass measurements as a tool to characterize oligomers in secondary organic aerosols, *Anal Chem*, **2007**, *79*, 4074-4082.
- (37) Went, F. W., Blue hazes in the atmosphere, *Nature*, **1960**, *187*, 641-643.
- (38) Novakov, R. and J. E. Penner, Large contribution of organic aerosols to cloud-condensation nuclei concentrations, *Nature*, **1993**, *365*, 823-826.
- (39) Robinson, A. L. et al., Rethinking organic aerosols: Semivolatile emissions and photochemical aging, *Science*, **2007**, *315*, 1259-1262.
- (40) Fehsenfeld, F. C. et al., Emissions of volatile organic compounds from vegetation and the implications for atmospheric chemistry, *Global Biogeochem Cycles*, **1992**, *6*, 389-420.
- (41) Goldstein, A. H. and I. E. Galbally, Known and unexplored organic constituents in the Earth's atmosphere, *Environ Sci Technol*, **2007**, *41*, 1515-1521.
- (42) Lamb, B. et al., A national inventory of biogenic hydrocarbon emissions, *Atmos Environ*, **1987**, *21*, 1695-1705.
- (43) Kavouras, I. G. et al., Formation of atmospheric particles from organic acids produced by forests, *Nature*, **1998**, *395*, 683-686.
- (44) Yu, J. et al., Gas-phase ozone oxidation of monoterpenes: Gaseous and particulate products, *J Atmos Chem*, **1999**, *34*, 207-258.
- (45) Claeys, M. et al., Hydroxydicarboxylic acids: Markers for secondary organic aerosol from the photooxidation of α -pinene, *Environ Sci Technol*, **2007**, *41*, 1628-1634.
- (46) Presto, A. A. et al., Secondary organic aerosol production from terpene ozonolysis. 1. Effect of UV radiation, *Environ Sci Technol*, **2005**, *39*, 7036-7045.
- (47) Gao, S. et al., Low-molecular-weight and oligomeric components in secondary organic aerosol from the ozonolysis of cycloalkenes and α -pinene, *J Phys Chem A*, **2004**, *108*, 10147-10164.
- (48) Dalton, C. N., et al., Continuous real-time analysis of products from the reaction of some monoterpenes with ozone using atmospheric sampling glow discharge ionization coupled to a quadrupole ion mass spectrometer, *Anal Chem*, **2005**, *77*, 3156-3163.
- (49) Jang, M. et al., Heterogeneous atmospheric aerosol production by acid-catalyzed particle-phase reactions, *Science*, **2002**, *298*, 814-817.
- (50) Griffin, R. J. et al., Organic aerosol formation from the oxidation of biogenic precursors, *J Geophys Res*, **1999**, *104*, 3555-3567.
- (51) Criegee, R., Mechanism of ozonolysis, *Angew Chem*, **1975**, *87*, 765-771.
- (52) Griesbaum, K. et al., Ozonides of mono-, bi- and tricyclic terpenes, *Tetrahedron*, **1996**, *52*, 14813-14826.
- (53) Griesbaum, K. et al., Isolation of ozonides from gas-phase ozonolyses of terpenes, *Environ Sci Technol*, **1998**, *32*, 647-649.
- (54) Nørgaard, A. W. et al., Secondary limonene endo-ozonide: A major product from gas-phase ozonolysis of *R*-(+)-limonene at ambient temperature, *Atmos Environ*, **2006**, *40*, 3460-3466.

- (55) Cai, X. and R. J. Griffin, Secondary aerosol formation from the oxidation of biogenic hydrocarbons by chlorine atoms, *J Geophys Res*, **2006**, *111*, D14206.
- (56) Grosjean, D. et al., Atmospheric oxidation of biogenic hydrocarbons: Reaction of ozone with α -pinene, d-limonene and *trans*-caryophyllene, *Environ Sci Technol*, **1993**, *27*, 2754-2758.
- (57) Grosjean, D. et al., Atmospheric oxidation of selected terpenes and related carbonyls: Gas-phase carbonyl products, *Environ Sci Technol*, **1992**, *26*, 1526-1533.
- (58) Librando, V. and G. Tringali, Atmospheric fate of OH initiated oxidation of terpenes: Reaction mechanism of α -pinene degradation and secondary organic aerosol formation, *J Environ Manage*, **2005**, *75*, 275-282.
- (59) Yokouchi, Y. and Y. Ambe, Aerosols formed from the chemical reaction of monoterpenes and ozone, *Atmos Environ*, **1985**, *19*, 1271-1276.
- (60) Kamens, R. M. et al., Aerosol formation from the reaction of α -pinene and ozone using a gas-phase kinetics-aerosol partitioning model, *Environ Sci Technol*, **1999**, *33*, 1430-1438.
- (61) Leungsakul, S. et al., Kinetic mechanism for predicting secondary organic aerosol formation from the reaction of d-limonene with ozone, *Environ Sci Technol*, **2005**, *39*, 9583-9594.
- (62) Jaoui, M. et al., Analysis of secondary organic aerosol compounds from the photooxidation of d-limonene in the presence of NO_x and their detection in ambient PM_{2.5}, *Environ Sci Technol*, **2006**, *40*, 3819-3828.
- (63) Donahue, N. M. et al., Secondary organic aerosol from limonene ketone: Insights into terpene ozonolysis via synthesis of key intermediates, *Phys Chem Chem Phys*, **2007**, *9*, 2991-2998.
- (64) Hakola, H. et al., Product formation from the gas-phase reactions of OH radicals and O₃ with a series of monoterpenes, *J Atmos Chem*, **1994**, *18*, 75-102.
- (65) Spittler, M. et al., Reactions of NO₃ radicals with limonene and α -pinene: Product and SOA formation, *Atmos Environ*, **2006**, *40*, S116-S127.
- (66) Tolocka, M. P. et al., Chemistry of particle inception and growth during α -pinene ozonolysis, *Environ Sci Technol*, **2006**, *40*, 1843-1848.
- (67) Docherty, K. S. et al., Contributions of organic peroxides to secondary aerosol formed from reactions of monoterpenes with O₃, *Environ Sci Technol*, **2005**, *39*, 4049-4059.
- (68) Tolocka, M. P. et al., Formation of oligomers in secondary organic aerosol, *Environ Sci Technol*, **2004**, *38*, 1428-1434.
- (69) Baltensperger, U. et al., Secondary organic aerosols from anthropogenic and biogenic precursors, *Faraday Discuss*, **2005**, *130*, 265-278.
- (70) Walser, M. L. et al., High-resolution mass spectrometric analysis of secondary organic aerosol produced by ozonation of limonene, *submitted to Phys Chem Chem Phys*, **2007**.
- (71) Czoschke, N. M. et al., Effect of acidic seed on biogenic secondary organic aerosol growth, *Atmos Environ*, **2003**, *37*, 4287-4299.

- (72) Kleindienst, T. E. et al., Secondary organic carbon and aerosol yields from the irradiations of isoprene and α -pinene in the presence of NO_x and SO₂, *Environ Sci Technol*, **2006**, *40*, 3807-3812.
- (73) Fick, J. et al., A study of the gas-phase ozonolysis of terpenes: The impact of radicals formed during the reaction, *Atmos Environ*, **2002**, *36*, 3299-3308.
- (74) Kanakidou, M. et al., Organic aerosol and global climate modelling: A review, *Atmos Chem Phys*, **2005**, *5*, 1053-1123.
- (75) Zhang, J. et al., Secondary organic aerosol formation from limonene ozonolysis: Homogeneous and heterogeneous influences as a function of NO_x, *J Phys Chem A*, **2006**, *110*, 11053-11063.
- (76) Presto, A. A. et al., Secondary organic aerosol production from terpene ozonolysis. 2. Effect of NO_x concentration, *Environ Sci Technol*, **2005**, *39*, 7046-7054.
- (77) Pandis, S. N. et al., Aerosol formation in the photooxidation of isoprene and α -pinene, *Atmos Environ*, **1991**, *25A*, 997-1008.
- (78) Presto, A. A. and N. M. Donahue, Investigation of α -pinene + ozone secondary organic aerosol formation at low total aerosol mass, *Environ Sci Technol*, **2006**, *40*, 3536-3543.
- (79) Leungsakul, S. et al., A kinetic mechanism for predicting secondary aerosol formation from the reactions of d-limonene in the presence of oxides of nitrogen and natural sunlight, *Atmos Environ*, **2005**, *39*, 7063-7082.
- (80) Sax, M. et al., Time resolved infrared spectroscopic analysis of aerosol formed by photo-oxidation of 1,3,5-trimethylbenzene and α -pinene, *Aerosol Sci Technol*, **2005**, *39*, 822-830.
- (81) Robinson, A. L. et al., Photochemical oxidation and changes in molecular composition of organic aerosol in the regional context, *J Geophys Res*, **2006**, *111*, D03302.
- (82) Ellison, G. B. et al., Atmospheric processing of organic aerosols, *J Geophys Res*, **1999**, *104*, 11633-11641.
- (83) Gaffney, J. S. et al., Natural radionuclides in fine aerosols in the Pittsburgh area, *Atmos Environ*, **2004**, *38*, 3191-3200.
- (84) Rudich, Y., Laboratory perspectives on the chemical transformations of organic matter in atmospheric particles, *Chem Rev*, **2003**, *103*, 5097-5124.
- (85) Morris, J. W. et al., Kinetics of submicron oleic acid aerosols with ozone: A novel aerosol mass spectrometric technique, *Geophys Res Lett*, **2002**, *29*, 1357-1360.
- (86) Alves, C. et al., Mass balance of organic carbon fractions in atmospheric aerosols, *J Geophys Res*, **2002**, *107*, 8345-8353.
- (87) Duce, R. A. et al., Organic material in the global troposphere, *Reviews of Geophysics and Space Physics*, **1983**, *21*, 921-952.
- (88) Hildemann, L. M. et al., Chemical composition of emissions from urban sources of fine organic aerosol, *Environ Sci Technol*, **1991**, *25*, 744-759.
- (89) Liu, D.-Y. et al., Aerosol time-of-flight mass spectrometry during the Atlanta Supersite experiment: 1. Measurements, *J Geophys Res*, **2003**, *108*, D78246.

- (90) Middlebrook, A. M. et al., Observations of organic material in individual marine particles at Cape Grim during the First Aerosol Characterization Experiment (ACE 1), *J Geophys Res*, **1998**, *103*, 16475-16483.
- (91) Mochida, M. et al., Fatty acids in the marine atmosphere: Factors governing their concentrations and evaluation of organic films on sea-salt particles, *J Geophys Res*, **2002**, *107*, D174325.
- (92) Murphy, D. M. et al., In situ measurements of organics, meteoritic material, mercury, and other elements in aerosols at 5 to 19 kilometers, *Science*, **1998**, *282*, 1664-1669.
- (93) Raes, F. et al., The Second Aerosol Characterization Experiment (ACE-2): General overview and main results, *Tellus, Series B: Chemical and Physical Meteorology*, **2000**, *52B*, 111-125.
- (94) Warscheid, B. and T. Hoffmann, Structural elucidation of monoterpene oxidation products by ion trap fragmentation using on-line atmospheric pressure chemical ionisation mass spectrometry in the negative ion mode, *Rapid Commun Mass Spectrom*, **2001**, *15*, 2259-2272.
- (95) Warscheid, B. and T. Hoffmann, Direct analysis of highly oxidised organic aerosol constituents by on-line ion trap mass spectrometry in the negative-ion mode, *Rapid Commun Mass Spectrom*, **2002**, *16*, 496-504.
- (96) Kalberer, M. et al., Identification of polymers as major components of atmospheric organic aerosols, *Science*, **2004**, *303*, 1659-1662.
- (97) Feltham, E. J. et al., Reactions of alkenes with ozone in the gas phase: A matrix-isolation study of secondary ozonides and carbonyl-containing reaction products, *Spectrochim Acta A*, **2000**, *56A*, 2605-2616.
- (98) Bonn, B. and G. K. Moortgat, New particle formation during α - and β -pinene oxidation by O₃, OH and NO₃, and the influence of water vapor: Particle size distribution studies, *Atmos Chem Phys*, **2002**, *2*, 183-196.
- (99) van Reken, T. M. et al., Cloud condensation nucleus activation properties of biogenic secondary organic aerosol, *J Geophys Res*, **2005**, *110*, D07206.
- (100) Iinuma, Y. et al., Aerosol-chamber study of the α -pinene/O₃ reaction: Influence of particle acidity on aerosol yields and products, *Atmos Environ*, **2004**, *38*, 761-773.
- (101) Gao, S. et al., Particle phase acidity and oligomer formation in secondary organic aerosol, *Environ Sci Technol*, **2004**, *38*, 6582-6589.
- (102) Britigan, N. et al., Quantification of ozone levels in indoor environments generated by ionic and ozonolysis air purifiers, *J Air & Waste Manage Assoc*, **2005**, *56*, 601-610.
- (103) Kendrick, E., A mass scale based on CH₂ = 14.0000 for high resolution mass spectrometry of organic compounds, *Anal Chem*, **1963**, *35*, 2146-2154.
- (104) van Krevelen, D. W., Graphical statistical method for investigation of the structure of coal, *Fuel*, **1950**, *29*, 269-284.
- (105) Pope, C. A., III et al., Lung cancer, cardiopulmonary mortality, and long-term exposure to fine particulate air pollution, *J Amer Med Assoc*, **2002**, *287*, 1132-1141.

- (106) Gauderman, W. J. et al., Association between air pollution and lung function growth in Southern California children: Results from a second cohort, *Am J Respir Crit Care Med*, **2000**, *166*, 76-84.
- (107) Seinfeld, J. H., Clouds, contrails and climate, *Nature*, **1998**, *391*, 837-838.
- (108) Sarwar, G. et al., Indoor fine particles: The role of terpene emissions from consumer products, *J Air & Waste Manage Assoc*, **2004**, *54*, 367-377.
- (109) Kroll, J. H. et al., Secondary organic aerosol formation from isoprene photooxidation, *Environ Sci Technol*, **2006**, *40*, 1869-1877.
- (110) Ng, N. L. et al., Contribution of first- versus second-generation products to secondary organic aerosols formed in the oxidation of biogenic hydrocarbons, *Environ Sci Technol*, **2006**, *40*, 2283-2297.
- (111) Gomez, A. L. et al., UV photodissociation spectroscopy of oxidized undecylenic acid films, *J Phys Chem A*, **2006**, *110*, 3584-3592.
- (112) Park, J., A.L. Gomez, M.L. Walser, A. Lin, and S.A. Nizkorodov, Ozonolysis and photolysis of alkene-terminated self-assembled monolayers on quartz nanoparticles: Implications for photochemical aging of organic aerosol particles, *Phys Chem Chem Phys*, **2006**, *8*, 2506-2512.
- (113) Pan, X. et al., Photochemistry of limonene derived secondary organic aerosol analyzed via chemical ionization mass spectrometry, *in preparation*, **2007**.
- (114) Wennberg, P. O. et al., Twilight observations suggest unknown sources of HO_x, *Geophys Res Lett*, **1999**, *26*, 1373-1376.
- (115) Sander, S. P. et al. *Chemical kinetics and photochemical data for use in stratospheric modeling: Evaluation number 14*; JPL Publication 02-25 ed.; Jet Propulsion Laboratory: Pasadena, 2003.
- (116) Bertram, A. K. et al., The reaction probability of OH on organic surfaces of tropospheric interest, *J Phys Chem A*, **2001**, *105*, 9415-9421.
- (117) Hawkins, M. et al., Matrix infrared spectra and photolysis and pyrolysis of isotopic secondary ozonides of ethylene, *J of Phys Chem*, **1982**, *86*, 3154-3166.
- (118) Andrews, L. and C. K. Kohlmeier, Infrared spectra and photochemistry of the primary and secondary ozonides of propene, trans-2-butene, and methylpropene in solid argon, *J of Phys Chem*, **1982**, *86*, 4548-4557.
- (119) Rickard, A. R. et al., OH yields in the gas-phase reactions of ozone with alkenes, *J Phys Chem A*, **1999**, *103*, 7656-7664.
- (120) Paulson, S. E. et al., OH radical formation from gas-phase reaction of ozone with terminal alkenes and the relationship between structure and mechanism, *J Phys Chem A*, **1999**, *103*, 8125-8138.
- (121) Paulson, S. E. et al., Measurement of OH radical formation from the reaction of ozone with several biogenic alkenes, *J Geophys Res*, **1998**, *103*, 25533-25539.
- (122) Orlando, J. J., In *The handbook of environmental chemistry* 2003; Vol. 3, Part R, pp. 253-299.
- (123) Atkinson, R. and W. P. L. Carter, Kinetics and mechanisms of the gas-phase reactions of ozone with organic compounds under atmospheric conditions, *Chem Rev*, **1984**, *84*, 437-470.

- (124) Harper, D. B. and J. T. Hamilton In *The handbook of environmental chemistry* 2003; Vol. 3, Part P, pp. 17.
- (125) Solomon, S. et al., On the role of iodine in ozone depletion, *J Geophys Res*, **1994**, *99*, 20491-20499.
- (126) Davis, D. et al., Potential impact of iodine on tropospheric levels of ozone and other critical oxidants, *J Geophys Res*, **1996**, *101*, 2135-2147.
- (127) Carpenter, L. J. et al., Short-lived alkyl iodides and bromides at Mace Head, Ireland: Links to biogenic sources and halogen oxide production, *J Geophys Res*, **1999**, *104*, 1679-1689.
- (128) O'Dowd, C. D. et al., Marine aerosol formation from biogenic iodine emissions, *Nature*, **2002**, *417*, 632-636.
- (129) Saiz-Lopez, A. and J. M. C. Plane, Recent applications of differential optical absorption spectroscopy: Halogen chemistry in the lower troposphere, *J Phys IV*, **2004**, *121*, 223-238.
- (130) von Glasow, R. et al., Impact of reactive bromine chemistry in the troposphere, *Atmos Chem Phys*, **2004**, *4*, 2481-2497.
- (131) Cox, M. L. et al., Identification of regional sources of methyl halides from AGAGE observations at Cape Grim, Tasmania, *J Atmos Chem*, **2005**, *50*, 59-77.
- (132) Montzka, S. A., et al., Controlled substances and other source gases, In *Scientific assessment of ozone depletion:2002*, chap. 1, World Meteorol. Org., 2003.
- (133) Butler, J. H., Atmospheric chemistry: Better budgets for methyl halides?, *Nature*, **2000**, *403*, 260-261.
- (134) Wuosmaa, A. M. and L. P. Hager, Methyl chloride transferase: A carbocation route for biosynthesis of halometabolites, *Science*, **1990**, *249*, 160-162.
- (135) Hamilton, J. T. et al., Chloride methylation by plant pectin: An efficient environmentally significant process, *Science*, **2003**, *301*, 206-209.
- (136) Varner, R. K. et al., Wetlands: A potentially significant source of atmospheric methyl bromide and methyl chloride, *Geophys Res Lett*, **1999**, *26*, 2433-2436.
- (137) Rhew, R. C. et al., Natural methyl bromide and methyl iodide emissions from coastal salt marshes, *Nature*, **2000**, *403*, 292-295.
- (138) Cox, M. L. et al., Terrestrial sources and sinks of halomethanes near Cape Grim, Tasmania, *Atmos Environ*, **2004**, *38*, 3839-3852.
- (139) Redeker, K. R. et al., Emissions of methyl halides and methane from rice paddies, *Science*, **2000**, *290*, 966-969.
- (140) Yokouchi, Y. et al., Strong emissions of methyl chloride from tropical plants, *Nature*, **2002**, *416*, 163-165.
- (141) Hogarth, P. J., *The biology of mangroves*; Oxford Univ. Press: New York, 1999.
- (142) Ellison, A. M. and E. J. Farnsworth, In *Marine community ecology*; Bertness, M. D. et al., Eds.; Sinauer: Sunderland, Mass, 2001.
- (143) Kathiresan, K. and B. L. Bingham, In *Advances in marine biology*; Southward, A. J. et al., Eds.; Elsevier: New York, 2001.
- (144) Redeker, K. R. and R. J. Cicerone, Environmental controls over methyl halide emissions from rice paddies, *Global Biogeochem Cycles*, **2004**, *18*, GB1027.

- (145) Ralph, Y. J. and S. L. Manley, Spatial and temporal variation in tissue halide levels of *Salicornia virginica*, *Wetlands*, **2006**, *26*, 97-106.
- (146) Gran, G., Determination of the equivalence point in potentiometric titrations: Part II, *Analyst*, **1952**, *77*, 661-673.
- (147) Zedler, J. B. and C. S. Nordby, The ecology of Tijuana Estuary, California: An estuarine profile, U.S. Fish and Wildlife Serv., 1986.
- (148) Boyer, K. E. et al., *Salicornia virginica* in a southern California salt marsh: Seasonal patterns and a nutrient-enrichment experiment, *Wetlands*, **2001**, *21*, 315-326.
- (149) Manley, S. L., Phytogenesis of halomethanes: A product of selection or a metabolic accident?, *Biogeochemistry*, **2002**, *60*, 163-180.
- (150) Manley, S. L. and M. N. Dastoor, Methyl halide (CH₃X) production from the giant kelp, *Macrocystis*, and estimates of global CH₃X production by kelp, *Limnol Oceanogr*, **1987**, *32*, 709-715.
- (151) Rhew, R. C. et al., Environmental and biological controls on methyl halide emissions from southern California coastal salt marshes, *Biogeochemistry*, **2002**, *60*, 141-161.
- (152) Covin, J. D. and J. B. Zedler, Nitrogen effects on *Spartina foliosa* and *Salicornia virginica* in the salt marsh at Tijuana Estuary, California, *Wetlands*, **1988**, *8*, 51-65.
- (153) Ross, J. R. et al., S-adenosyl-L-methionine:Salicylic acid carboxyl methyltransferase, an enzyme involved in floral scent production and plant defense, represents a new class of plant methyltransferases, *Arch Biochem*, **1999**, *367*, 9-16.
- (154) Jennings, D. H., Halophytes, succulence and sodium in plants: A unified theory, *New Phytol*, **1968**, *67*, 899-911.
- (155) Manley, S. L. et al., Laboratory production of bromoform, methylene bromide, and methyl iodide by macroalgae and distribution in nearshore southern California waters, *Limnol Oceanogr*, **1992**, *37*, 1652-1659.
- (156) Nightingale, P. D. et al., Production of chloroform and other low molecular weight halocarbons by some species of macroalgae, *Limnol Oceanogr*, **1995**, *40*, 680-689.
- (157) Admiraal, W., In *Progress in phycological research*; Round, F. E., Chapman, D. J., Eds.; Biopress: Bristol, U.K., 1984.
- (158) Tait, V. K. and R. M. Moore, Methyl chloride production in phytoplankton cultures, *Limnol Oceanogr*, **1995**, *40*, 189-195.
- (159) Scarratt, M. G. and R. M. Moore, Production of methyl chloride and methyl bromide in laboratory cultures of marine phytoplankton, *Mar Chem*, **1996**, *54*, 263-272.
- (160) Manley, S. L. and J. L. de la Cuesta, Methyl iodide production from marine phytoplankton cultures, *Limnol Oceanogr*, **1997**, *42*, 142-147.
- (161) Tessier, E. et al., Formation and volatilization of alkyl-iodides and -selenides in macrotidal estuaries, *Biogeochemistry*, **2002**, *59*, 183-206.
- (162) Keppler, F. et al., Halocarbons produced by natural oxidation processes during degradation of organic matter, *Nature*, **2000**, *403*, 298-301.

- (163) Redeker, K. R. et al., Ectomycorrhizal fungi: A new source of atmospheric methyl halides?, *Global Chang Biol*, **2004**, *10*, 1009-1016.
- (164) Smith, S. M. and S. C. Snedaker, Salinity responses in two populations of viviparous *Rhizophora mangle* l. Seedlings, *Biotropica*, **1995**, *27*, 435-440.
- (165) Sobrado, M. A., Relations of water transport to leaf gas exchange properties in three mangrove species, *Trees*, **2000**, *14*, 258-262.
- (166) Clough, B. F. et al., Estimating leaf area index and photosynthetic production in canopies of the mangrove *Rhizophora apiculata*, *Atmos Environ*, **1997**, *38*, 3839-3852.
- (167) Sherman, R. E. et al., Spatial patterns of biomass and aboveground net primary productivity in a mangrove ecosystem in the Dominican Republic, *Ecosystems*, **2003**, *6*, 384-398.
- (168) Araújo, R. J. et al., LAI and leaf size differences in two red mangrove forest types in south Florida, *Bull Mar Sci*, **1997**, *60*, 643-647.
- (169) Green, E. P. et al., Estimating leaf area index of mangroves from satellite data, *Aquat Bot*, **1997**, *58*, 11-19.
- (170) Market, B. and R. Jayasekera, Elemental composition of different plant species, *J Plant Nutr*, **1987**, *10*, 783-794.
- (171) Rhew, R. C. et al., Genetic control of methyl halide production in *Arabidopsis*, *Curr Biol*, **2003**, *13*, 1809-1813.
- (172) Duarte, C. M. et al., Major role of marine vegetation on the oceanic carbon cycle, *Biogeoscience*, **2005**, *2*, 659-679.